Variations de charge d'antennes radio-fréquence pour la mesure de signaux physiologiques en imagerie cardiaque par résonance magnétique

Guido Peter Kudielka

Thèse
présentée pour l'obtention du titre de
Docteur en Sciences de l'Université de Lorraine
École Doctorale IAEM – Mention Automatique
par **Guido Peter Kudielka**

Coil load changes for physiological motion acquisition in cardiac magnetic resonance imaging

(Soutenance le 31 mai 2016)

Rapporteurs :	
M. Axel Haase	Professeur, Technische Universität, Munich
M. Ewald Moser	Professeur, Medizinische Universität, Vienne
Examinateurs :	
M. Jacques Felblinger	Professeur, Université de Lorraine, Nancy (Directeur de thése)
M. Pierre-André Vuissoz	Ingénieur de recherche, Université de Lorraine, Nancy (Co-directeur de thése)
M. Jean-Marie Escanyé	Maître de conference, Université de Lorraine, Nancy
M. Timo Schirmer	Manager du laboratoire, GE Global Research, Munich

Laboratoire d'Imagerie Adaptative Diagnostique et Interventionnelle – INSERM U947
CHRU de Nancy Brabois – 4e étage - Tour Drouet
Rue du Morvan – 54511 Vandoeuvre-lès-Nancy – FRANCE

Guido Peter Kudielka: Coil load changes for physiological motion acquisition in cardiac magnetic resonance imaging , *Variations de charge d'antennes radio-fréquence pour la mesure de signaux physiologiques en imagerie cardiaque par résonance magnétique*

Manuscript submitted on April, 6th 2016.

Final Version as of August 6, 2016 (classicthesis version 1.0).

For Dipl.-Ing.(FH) Hans-Ernst Nauck and Dr. med. Karl-Erhard Kudielka
... the early supporters

Acknowledgements

This research work was conducted in a unique collaboration between GE Global Research Europe (GRC) in Munich and the Laboratoire d'Imagerie Adaptive Diagnostique et Interventionelle (IADI) in Nancy. Hence I want express my sincere gratitude to Dr. Timo Schirmer and Prof. Jacques Felblinger who made this collaboration project possible. I also want to thank Dr. Kathleen Amm, Dr. Carlos Härtel and Dr. Anja Brau for their management support. My special gratitude goes to Prof. Axel Haase, Prof. Ewald Moser and Dr. Jean-Marie Escanye for volunteering as jury members and their constructive feedback on this thesis.

As this extra-occupational thesis at two locations involved many people, I want to thank all my colleagues at GRC, GE Healthcare and IADI for their support in this work. Especially I want to acknowledge

- Dr. Pierre-André Vuissoz for sharing his endless knowledge, always lending an ear to all my questions and supporting the experiments in Nancy.
- Dr. Anne Menini for her immens support - from the first "Bienvenue á IADI", the discussions on motion correction and data analysis up to the assistance in SAEC experiments in Munich.
- Dr. Freddy Odille for his support in GRICS reconstructions and experiments in Nancy.
- Dr. Alexia Missoffe and Julie Kabil for sharing their knowledge and performing the electromagnetic simulations for this research work.
- Dr. Christophe Meyer, Dr. Z'hor Ramdane-Cherif and Dr. Adnane Benhadid for all information about the SAEC system and the support for the Munich SAEC version.
- Piero Ghedin, Dr. Martin Janich, Dr. André Fischer and Dr. Ana-Bea Solana Sanchez for sharing their expertise in cardiac MR imaging.
- Dr. Sarra Aissani and Dr. Titus Lanz (Rapid Biomedical, Rimpar) for fruitful discussions on RF design.
- Dr. Christopher Hardy and Dr. Damien Mandry for helpful information on arterial pulse wave analysis.
- Dr. Gabriela Hossu, Dr. Pauline Ferry and Céline Fournier for all organisational support in Nancy.
- Joe Piel, Dr. Eric Fiveland, Reiner Metz and Susanne Günther for helping out at MR system related questions and product coil delivery.

Finally I want to thank my wife Nina for her abundance of patience and back up throughout the years and for always motivating me to drive this work to the end.

Résumé

L'Imagerie par Résonance Magnétique (IRM) est une technique d'imagerie non-invasive et non-ionisante permettant de générer des images tomographiques et des représentations tridimensionnelles des organes et des flux tels que les flux sanguins. Son principal inconvénient réside dans la longue durée d'acquisition nécessaire à la reconstruction d'une image. Ceci se traduit par une forte sensibilité aux mouvements des patients. Dans certains cas, la dégradation des images est telle que l'utilisation diagnostique est impossible. En imagerie cardiaque et thoracique, les mouvements cardiaques et respiratoires sont enregistrés avec des capteurs tels que les capteurs ECG et les ceintures respiratoires pour synchroniser les acquisitions et pour pratiquer des corrections rétrospectives des images. Le positionnement de ces capteurs augmente le temps de préparation des patients. Il présuppose également leur tolérance par les patients placés dans un espace restreint et déjà très contraints par l'antenne readio-fréquence nécessaire á l'imagerie. Enfin, ces capteurs peuvent diminuer la qualité du signal et donc celle des images. Dans ces travaux, l'antenne radio-fréquence déjà présente pour la réalisation de l'exam d'imagerie a été elle-même étudiée en tant que capteur de mouvements. Les variations des propriétés électromagnétiques des tissus dues aux mouvements se répercutent de manière directe sur l'impédance de l'antenne. Selon la position de l'antenne, les variations d'impédance induites par les mouvements cardiaques et respiratoires peuvent être enregistrées et utilisées dans des méthodes de correction de mouvements rétrospectives. Dans ce but, le système d'acquisition "Signal And Event Controller (SAEC)" développé au sein du laboratoire IADI a été amélioré en collaboration avec le laboratoire DIBT de GE Global Research. Les variations d'impédance induites par les mouvements ont été étudiées dans des dispositif utilisant soit des antennes readio-fréquence volumique ou des antennes radio-fréquence surfacique sur des objets-test animés et sur des sujets sains. Les mouvements respiratoires, cardiaques et les flux sanguins ont été enregistrés avec cette méthode. Puis, les résultats expérimentaux ont été comparés à des simulations électromagnétiques et aux données de la littérature. Enfin, l'enregistrement continu des mouvements a été réalisé lors d'acquisitions IRM cardiaques chez des sujets sains. Une correction de mouvements rétrospective avec l'algorithme GRICS a été appliquée à ces données démontrant la faisabilité de l'utilisation des antennes d'imagerie comme capteurs de mouvements.

Mots clés

Imagerie par Résonance Magnétique, antenne Radio-Fréquence (RF), mesures d'impédance, enregistrement de mouvements, imagerie cardiaque

Abstract

Magnetic resonance imaging (MRI) is a non-invasive and non-ionizing imaging technology that generates tomographic cross-sections or three-dimensional views of organs and blood flow. One major drawback is its long image acquisition time and, therefore, high sensitivity to patient motion. This leads to degradation in the image quality up to a level where clinical reporting is impossible. Especially in cardiac and thoracic imaging, respiratory motion and heart movement need to be registered using sensors like electrocardiogram or respiratory belts, in order to trigger the image acquisition or perform retrospective corrections. The placement of the sensors extends the patient preparation time, is critical for signal quality and, hence, image quality, and expects patients to tolerate additional sensors besides the imaging coil and space restrictions. In this work, the imaging coil itself was investigated for sensor-less motion registration. Motion-related variations of the electromagnetic properties of tissue have a direct effect on the coil impedance. Depending on the position of the coil, various cardiovascular and respiration-induced impedance changes can be recorded and used for retrospective motion-correction methods. For this purpose, the multi-source acquisition system "Signal And Event Controller (SAEC)," developed at Imagerie Adaptive Diagnostique et Interventionelle (IADI), was further enhanced in collaboration with the Diagnostics, Imaging and Biomedical Technologies Laboratory (DIBT) laboratory of GE Global Research. The impedance changes of volume coils and local loop coils were investigated using moving phantoms on healthy volunteers. Lung motion, myocardial-related motion, and vascular blood flow were registered with this method. The experimental findings were compared to electromagnetic simulations and the data gathered by state-of-the-art sensors. Finally, continuous motion registration during cardiac MRI image acquisition and retrospective motion correction with the GRICS algorithm was executed on healthy volunteers to show the feasibility of imaging coils as reliable motion sensors.

Keywords

Magnetic Resonance Imaging, RF coil, impedance measurement, motion registration, Cardiac imaging

Contents

Acknowledgements v

Résumé vii

Abstract ix

Contents xi

List of Tables xiv

List of figures xiv

Acronyms xviii

INTRODUCTION xxiii

I FUNDAMENTALS AND METHODS 3

1 MAGNETIC RESONANCE IMAGING (MRI) AND THE PROBLEM OF MOTION 5
1.1 The Nuclear Magnetic Resonance signal - from nuclear spin to image 5
1.1.1 The magnetic moment of spins . . . 5
1.1.2 Excitation and Relaxation of nuclear spins . . . 7
1.1.3 Spatial encoding and signal detection . . . 9
1.2 MRI system hardware . . . 12
1.3 Motion in MRI . . . 15
1.3.1 Image artifacts caused by motion . . . 15
1.3.2 Physiological motion in Cardiac MRI . . . 17
1.4 Motion artifact reduction and correction . . . 22
1.4.1 Motion prevention . . . 22
1.4.2 Motion insensitive imaging sequences . . . 22
1.4.3 Motion correction . . . 24
1.4.4 Motion detection techniques . . . 25
1.4.5 Motion handling in CMR . . . 28
1.5 Summary . . . 31

2 INTRODUCTION TO RADIO FREQUENCY TECHNOLOGY IN MRI 35
2.1 RF coil design for MRI . . . 35
2.1.1 The RLC circuit . . . 36
2.1.2 Tuning and Matching . . . 37
2.1.3 Coil Sensitivity, Q-value and losses . . . 38
2.1.4 Coil types for MRI . . . 41
2.2 RF measurement techniques . . . 45
2.2.1 Scatter parameters for characterization of RF circuits . . . 45

2.2.2 Impedance determination by power measurement 47
2.3 Electromagnetic properties of biological tissue 48
2.4 Electromagnetic simulation for MRI systems 50
2.5 Summary 52

3 EQUIPMENT AND METHODS TO MEASURE COIL IMPEDANCE CHANGES 53
3.1 The work environment at IADI and GE Global Research 53
3.1.1 Clinical instrumentation at IADI 54
3.1.2 RF and MRI labs at GE Global Research 54
3.1.3 Signal Acquisition and Event Controller (SAEC) 56
3.2 Measurement systems for coil load change acquisition 59
3.2.1 Reflective power measurement on MRI RF amplifier 59
3.2.2 Flexible power reflection measurement system for MRI coils . 60
3.2.3 Coil load measurements during imaging 61
3.3 LabView applications for coil load changes 64
3.3.1 The Producer-Consumer-Architecture 64
3.3.2 Transfer of power meter measurements to SAEC 66
3.3.3 Continuous S-parameter recording with a VNA 67
3.4 Post-processing methods 68
3.4.1 Signal processing with MATLAB 68
3.4.2 Image processing and quality metric 68
3.5 Coil design for load change experiments 70
3.6 Summary 70

II THE EFFECT OF COIL LOAD CHANGES CAUSED BY MOTION 73

4 NUMERICAL ANALYSIS OF COIL LOAD CHANGES 75
4.1 EM simulation design on coil load variations 75
4.2 Simulated and measured Q-values on a homogeneous load 76
4.3 Results of human body model simulations and invivo measurements 77
4.4 Discussion 79

5 MOTION INDUCED LOAD CHANGES OF VOLUME COILS 81
5.1 Reflected power of excitation pulses for respiration measurement . . 81
5.1.1 Investigation of respiration influence on RF excitation power 82
5.1.2 Application of reflected power information for motion correction 84
5.2 Birdcage coil modes for motion detection 86
5.2.1 Investigation of birdcage coil modes for motion detection . . . 86
5.2.2 Motion registration during MRI imaging 88
5.3 Discussion 91

6 MEASUREMENT OF LOAD CHANGES ON LOCAL COILS 93
6.1 Load changes of surface coils at several body positions 93
6.1.1 Respiratory motion detection 95
6.1.2 Arterial pulse flow detection 95
6.1.3 Heart motion representation 98

6.2 Local acquisition of load changes as a motion indicator during Cine imaging . . . 101
6.2.1 Clinical volunteer setup and data analysis methods . . . 101
6.2.2 Retrospective respiratory motion correction . . . 102
6.2.3 Coil load data compared to left ventricular volume variations 106
6.3 Simultaneous load change acquisition of a multi-channel coil . . . 109
6.3.1 S-parameter setup on 4-channel cardiac coil . . . 109
6.3.2 4-port S-parameters of a volunteer measurement . . . 110
6.4 Discussion . . . 114

III DISCUSSION AND OUTLOOK 115

DISCUSSION – ADVANTAGES AND LIMITATIONS 117

OUTLOOK 120

PUBLICATIONS 121

BIBLIOGRAPHY 123

List of Tables

Table 1	Volume parameters of atria and ventricles	21
Table 2	Summary of advantages and limitations of various motion detection methods	33
Table 3	Frequency behavior of resistor-, inductance-, and capacitor impedance	36
Table 4	Permittivity and conductivity values for heart and lung tissue	49
Table 5	Technical specifications of GE HDxt and MR750w MRI systems	55
Table 6	RF lab equipment used for experiments in this thesis	55
Table 7	Sampling frequencies of the SAEC system	57
Table 8	Capacitor values and Q-ratios for single loop coils	70
Table 9	Simulated and measured coil parameters	76
Table 10	Simulated and measured coil parameters on breathing	77
Table 11	Noise level comparison between normal conditions, with power on mode frequency (f = 64 MHz) and with BHP-100+ high pass filter (passband 90-2000MHz)	88
Table 12	Pulse wave velocities calculated from coil power reflections on six volunteers	97
Table 13	Heart motion analysis on six volunteers	100
Table 14	Mean image entropy over all cardiac cycles in five volunteers	102

List of Figures

Figure 1.1	Illustration of the magnetization vector $\vec{M}_0$ in a magnetic field	7
Figure 1.2	T1- and T2-relaxation for grey matter and Muscle tissue at 3T	9
Figure 1.3	Schematic of a MRI pulse sequence with k-space sampling	11
Figure 1.4	Schematic of a MRI system	12
Figure 1.5	Example of superconducting magnet and open magnet	13
Figure 1.6	Example of blurring in a short-axis heart image	16
Figure 1.7	Belt signal of two different breathing pattern	18
Figure 1.8	Anatomy of the human heart and ECG	19
Figure 1.9	Wiggers Diagram of cardiophysiologic pressure and flow	20
Figure 1.10	Arterial pressure in different arteries	21
Figure 1.11	Schematic of prospective and retrospective motion correction	24
Figure 1.12	Triggering and gating in cardiac imaging	29
Figure 1.13	Segmented Cine images and resultant ventricle volume course	29
Figure 1.14	Effect of magnetohydrodynamic effect on ECG	30
Figure 2.1	Frequency dependent impedance and schematic of coil circuit	37
Figure 2.2	Equivalent circuit for sample losses	40

Figure 2.3 Clinical birdcage coil and ladder network 42
Figure 2.4 Harmonic frequencies of 3T birdcage body coil 43
Figure 2.5 Clinical surface coils 43
Figure 2.6 S-parameters of one-, two- and four-port systems 45
Figure 2.7 Magnitude of S11 coefficient of a coil 46
Figure 2.8 Schematic of a directional coupler 47
Figure 2.9 Frequency dependent permittivity and conductivity of tissue 48
Figure 2.10 Virtual population provided by IT'IS foundation 51
Figure 3.1 Schematic of the new SAEC system 56
Figure 3.2 Mobile SAEC at GRC Munich 58
Figure 3.3 Schematic of motion acquisition by reflected power measurement 60
Figure 3.4 Schematic of switch setup for motion acquisition on birdcage coil modes 61
Figure 3.5 Schematic of motion acquisition setup with VNA 62
Figure 3.6 GUI of a LabView application 65
Figure 3.7 Schematic of LabView data acquistion application 65
Figure 3.8 R-peak detection and superposition of cardiac data 69
Figure 3.9 Photo and schematic of single loop coil for motion capture . 71
Figure 4.1 Coil position on human body model 76
Figure 4.2 Simulated coil impedance at deflated and inflated lung . . . 78
Figure 5.1 Excitation pulse of a gradient echo pulse sequence 82
Figure 5.2 Transmitted and reflected power of RF amplifier 83
Figure 5.3 Graphical comparison of reflected power of excitation pulse with respiratory belt 83
Figure 5.4 Reflected power level change on arm motion 84
Figure 5.5 Correlation of reflected power and pneumatic belt during free-breathing imaging 85
Figure 5.6 Comparison of uncorrected and GRICS corrected free-breathing exam 85
Figure 5.7 Power variations on birdcage coil modes caused by a moving phantom 87
Figure 5.8 Correlation of power variation on modes with pneumatic belt 87
Figure 5.9 Gradient echo sequence timing with switch activation 89
Figure 5.10 FFT of power signal on mode frequency 90
Figure 6.1 Positions of loop coil for physiologic data acquistion 94
Figure 6.2 Q-ratios for respiratory filtered signal on six volunteers at different positions 95
Figure 6.3 Signal of coil load changes on the wrist 96
Figure 6.4 Time points and distances for PWV calculations 97
Figure 6.5 Bandpass-filtered signal on position 1 in comparison with ECG and PPG 98
Figure 6.6 Comparison of experimental results with simulated cardio-physiologic data 99
Figure 6.7 1RR section with simulated left ventricular volume 100
Figure 6.8 Setup of clinical loop coil measurement on volunteer 101

Figure 6.9 Correlation between the coil S11 data and belt data 103
Figure 6.10 Comparison of raw S11-data, the chest belt and the abdominal belt on volunteer 3 with an atypical breathing pattern . 104
Figure 6.11 Short axis DICOM images of uncorrected and GRICS corrected (with belt and coil data) image data 104
Figure 6.12 Image entropy over 31 cardiac phases of volunteer 5 105
Figure 6.13 Superimposed ECG and S11-data in four volunteers 106
Figure 6.14 Mean of superimposed ECG and S11-data in comparison with segmented left ventricular volume 107
Figure 6.15 Bland-Altman plot of R-R durations measured from ECG data and S11-data 108
Figure 6.16 1.5T four channel cardiac coil 109
Figure 6.17 Schematic of the coil element positions on the volunteer . . 110
Figure 6.18 Respiratory portion of reflection coefficients of 4-ch coil during free-breathing 112
Figure 6.19 Respiratory portion of transmission coefficients of 4-ch coil during free-breathing 112
Figure 6.20 Cardiophysiologic signal of reflection coefficients of 4-ch coil during free-breathing 113

Figure 6.21 Cardiophysiologic signal of transmission coefficients of 4-ch coil during free-breathing 113

References for illustrations of other publications or internet:

Fig. 1.8a See page for author [GFDL (http://www.gnu.org/copyleft/fdl.html) or CC-BY-SA-3.0 (http://creativecommons.org/licenses/by-sa/3.0/)], via Wikimedia Commons

Fig. 1.8b By Agateller (Anthony Atkielski) (en:Image:SinusRhythmLabels.png) [Public domain], via Wikimedia Commons

Fig. 1.9 By Daniel Chang, MD revised original work of DestinyQx; Redrawn as SVG by xavax (Wikimedia Commons, File:Wiggers Diagram.png) [CC BY-SA 2.5 (http://creativecommons.org/licenses/by-sa/2.5)], via Wikimedia Commons

Fig. 1.14 Scientific Figure on ResearchGate. Available from: https://www.researchgate.net/figure/258766045$_$fig5

[accessed Feb 6, 2016]

Fig. 2.8 By Spinningspark at Wikipedia (File:Short_line_directional_coupler_equivalent_circuit.svg) [CC BY-SA 3.0 (http://creativecommons.org/licenses/by-sa/3.0)], via Wikimedia Commons

Fig. 2.9 The variations of the complex permittivity of the biological tissues... - Scientific Figure on ResearchGate. Available from: https://www.researchgate.net/figure/236941002_fig5_The-variations-of-the-complex-permittivity-of-the-biological-tissues-with-frequency

[accessed Feb 17, 2016]

Fig. 6.17 https://d1tb9j1fbhww3m.cloudfront.net/uploads/media/file/12982/sde018.jpg

[accessed, Feb 16, 2016]

Notations and abbreviations

Acronyms [1]

ACQ *acquisition window*

ADC analog-to-digital converter

AoF aortic flow

a.u. arbitrary units

bpm beats per minute

CHRU Centre Hospitalier Régional Universitaire

CIC-IT Centre d'Investigation Clinique pour l'Innovation Technologique

CMR, cMRI *cardiac magnetic resonance imaging*

CW continuous wave

DAC digital-to-analog converter

DC direct current

DIBT Diagnostic, Imaging and Biomedical Technologies Laboratory

ECG electrocardiogram

ED End-diastole

EDV End-diastolic volume of the heart ventricle

EM electromagnetic

emf electromagnetic force

ES end-systole

ESV end-systolic volume of the heart ventricle

ETL *Echo Train Length*

FID free induction decay

FIFO first in, first out

FFT fast Fourier transform

fMRI *functional magnetic resonance imaging (of the brain)*

FOV *Field of View*

FGRE *Fast GRadient Echo*

FSE *Fast Spin Echo*

GRICS Generalized Reconstruction by Inversion of a Coupled System

GRC GE Global Research Center

GRD *gradient signal*

GUI graphical user interface

HR heart rate

IADI Laboratoire d'Imagerie Adaptative, Diagnostic et Interventionnelle

INSERM Institut national de la santé et de la rechercge médicale

LV left ventricle of the heart

LVV left ventricular volume of the heart

1. *Acronyms specific to magnetic resonance imaging written in italic*

LAV	left artial volume of the heart
mmHg	millimeter of mercury (manometric pressure unit)
MRI	*magnetic resonance imaging*
MHD	magneto-hydrodynamic
NI	National Instruments Corporation
NMR	*nuclear magnetic resonance*
PAF	pulmonary artery flow
PACS	picture archiving and communication system
PPG	pulseplethysmograph
PSF	point spread function
PTT	pulse transit time
PUC	pick up coil
PWV	pulse wave velocity
RF	radio frequency
ROI	*region of interest*
RS-232	serial communication standard
RV	right ventricle of the heart
TE	*echo time*
TR	*repetition time*
TTL	transistor-transistor logic
SAEC	Signal and Event Controller
SAR	Specific Absorption Rate
SNR	*signal to noise ratio*
SV	stroke volume of the heart ventricle
UWB	ultra wideband radar
VNA	vector network analyzer

Notations

α	flip angle
$\vec{B_0}$	main magnetic field
$\vec{B_1}$	magnetic field of RF wave
C_M	matching capacitor
C_S	stray capacitance
C_T	tuning capacitor
$\Delta\omega$	full width half maximum bandwidth
$\Delta\upsilon$	acquisition bandwidth
ϵ', ϵ_r	relative permittivity
ϵ_0	permittivity of free space
E_m	Zeeman energy
f_0	resonance frequency
f_m	harmonic mode frequency of birdcage coil
γ	gyromagnetic ratio
Γ	reflection factor
$\vec{G}, G_x, G_y, G_z$	magnetic field gradients
G_F	frequency encoding gradient
G_P	phase encoding gradient
G_S	slice selection gradient
h	Planck's constant
$\hbar$	reduced Planck constant
I	angular momentum, spin
I_R	frequency dependentcurrent of resonant circuit
κ	coupling factor of directional couplers
k_B	Boltzmann constant
K	inductive coupling factor
L_m	inductance of magnetic field coupling
$\vec{M}$	macroscopic magnetization of protons
$\vec{M_z}$	longitudinal magnetization vector
$\vec{M_{xy}}$	transverse magnetization vector
m	magnetic quantum number
μ	magnetic moment
μ_0	Permeability in free space
$N\uparrow, N\downarrow$	number of parallel and antiparallel oriented spins
N_x, N_y	k-space matrix size
ω	circular frequency
ω_0	resonant circular frequency, Larmor frequency
ϕ_m	magnetic flux
P_{FWD}	(coupled) transmitted power
P_{REF}	(coupled) reflected power
Q	quality factor of RF component or circuit
Q_u	Q-value of unloaded RF circuit
Q_l	Q-value of loaded RF circuit
ρ	spin density
$\vec{R}$	spatial relaxation rates
$\vec{r}$	reciprocal space vector

R_C	resistive losses, coil resistance
R_D, R_e	dielectric losses
R_M, R_m	inductive losses
S	NMR signal amplitude
S_{ab}	scatter parameter between port a and b
σ	conductivity
θ	rotation angle of an object
T_1	longitudinal or spin-lattice relaxation
T_2	transverse or spin-spin relaxation
t_d	dwell time
T_d	delay time
T_p	motion acquisition duration
t_{ph}	phase encoding duration
U_S	induced voltage of NMR signal
U_N	voltage of noise
U_R	frequency dependent voltage of resonant circuit
X_C	reactance of capacitance
X_L	reactance of inductance
Z_C	impedance of capacitance
Z_L	impedance of inductance
Z_0	system impedance
Z_{CM}	impedance of matching capacitor
Z_e	impedance of dielectric losses
Z_m	impedance of inductive losses
Z_R	impedance of resonant circuit
Z_S	sample impedance

Introduction

Medical imaging is an important component in the increasing field of clinical diagnostics. In 2010, five billion imaging investigations were performed [1], whereby two-thirds were executed with ionizing radiation techniques, like X-ray, computer tomography (CT), positron emission tomography (PET) and single-photon emission computed tomography (SPECT). With the increasing trend on detecting illnesses in an early stage, continuous screening and regular control of therapy effects, non-ionizing imaging methods become more important. Since its beginnings in the 1970s, magnetic resonance imaging (MRI) developed to a powerful and flexible imaging modality without the compromise of exposing the patient to ionizing radiation. Its field of application reaches from cancer diagnosis in oncology, anatomy and pathology of organs or joints in gastrointestinal, musculoskeletal or neuro-imaging up to imaging hemodynamic responses in the brain (functional MRI) or metabolic development in cells (multi-nuclear imaging). Due to its good image contrast on soft tissue and liquid, cardiac magnetic resonance imaging (CMR, cMRI) has become an established imaging technique for diagnosing cardiovascular diseases. CMR provides information about the structure of the cardiovascular system, the function of the heart, perfusion of the myocard or blood flow in the heart and the vessels with high resolution and flexible imaging plane orientation.

The image acquisition process in MRI is based on the excitation of hydrogen nuclei and the signal detection during the relaxation process. This process requires a certain temporal period to generate an image and assumes a spatially static object during that time. Hence motion is a major problem in MRI, resulting in image distortions - so called "artifacts" - up to a level where clinical diagnostic is impossible. Patient motion is reported to be the main cause for repeated examinations in clinical practice [2], resulting in institutional cost increases of approximately US$115,000 per MRI scanner per year [3]. With further development of MRI, aiming higher image resolution, the sensitivity against motion increases accordingly. Today various approaches exist to solve the problem of motion, which can be classified into methods which "freeze" the actual motion state (fast imaging techniques), methods which prevent motion (demobilization) and methods which correct for the image distortions (motion correction techniques). As no gold standard solution exists, the application of these methods depends on the imaging region, patient compliance and type of imaging.

In CMR the physiological activity of the heart and the breathing motion has to be addressed in the image acquisition. This requires an additional effort in patient preparation and experienced personnel. In order to synchronize the image acquisition with the heart beat, electrocardiogram (ECG) signal is acquired simultaneously. Breathing motion is either minimized by breath-hold commands or by respiratory gating. The respiratory motion information is typically recorded from a pneumatic belt placed on the patient's chest. The positioning of these sensors is critical for

signal reliability and requires additional patient preparation time. Furthermore patient compliance is necessary throughout the 30 to 45 minute cardiac examination. However the claustrophobic situation inside the MRI tunnel could lead to anxiety especially in very young or old patients or in patients with acute cardiologic diseases. By placing additional sensors (ECG, pneumatic belt), the imaging coil and ear protection, the patient discomfort is further increased, resulting in additional motion or inability for breath-hold.

In this thesis the utilization of the imaging coil as a reliable, sensor-less physiologic motion sensor for CMR is investigated. This could reduce the preparation time and patient discomfort and could deliver additional information besides the ECG and respiratory motion. By measuring the impedance of the coil, information about the sample in close proximity to the coil can be acquired. Continuous impedance variations due to respiratory motion were reported in 1986 [4]. This thesis further investigates this effect for simultaneous respiratory and cardiophysiologic motion recording as a motion source for retrospective motion correction. In-vivo studies on the birdcage body coil and on surface coils were performed. For the latter also electromagnetic simulation were conducted and compared with the measured values. The measured impedance variation of the coil was analyzed with regards to state-of-the-art sensors, volumetric measurements from MRI images and physiologic simulation results. Finally also a multi-channel motion acquisition on a phased-array coil was performed, to analyze the loading change effect on four channels concurrently. It can be shown that sensor-less and contact-less motion acquisition with the imaging coil is a promising motion recording technique for CMR imaging.

This thesis was realized in a collaboration of the Laboratoire d'Imagerie Adaptative, Diagnostic et Interventionnelle (IADI) in Nancy, France and GE Global Research Europe (GRC) in Munich, Germany. In this collaboration, a data acquisition system ("SAEC") originally designed at IADI, was further developed and was deployed at GRC.

Outlook of this thesis

Part One gives the reader some supporting background. **Chapter 1** describes the fundamental physics of MRI and highlights the problem of motion and current solutions. MRI imaging of the heart with respect to the motion problem is explained in more detail. **Chapter 2** is dedicated to radio frequency (RF) technology in MRI. Several coils and their design are covered as well as information about electromagnetic simulations, RF measurement techniques and the behavior of biological tissue on electromagnetic waves. Since this thesis was realized in a collaboration of the IADI laboratory in Nancy, France and GE Global Research Europe in Munich, Germany both working environments and their specialties are addressed in **Chapter 3**. Furthermore the methodical background on hard- and software for the experiments is also described.

The research experiments and results are explained in Part Two. **Chapter 4** describes the comparison between numerical electromagnetic simulation and lab bench experiments of a single loop coil on the human chest. The load change effect on MRI coils was investigated in-vivo on volume and surface coils in several experiments. The investigation of birdcage coil impedance on motion induced load changes

and its utilization for motion correction can be found in **Chapter 5**. These results were presented in two poster presentation at the Motion Correction Workshop of the International Society of Magnetic Resonance in Medicine (ISMRM) 2014 in Tromsø, Norway [Kudielka et al., 2014a, Kudielka et al., 2014b]. One measurement technique which is described in this chapter, was also applied for patent and published in 2016 [Kudielka et al., 2016a]. The analysis of birdcage coils is followed by the study of single loop coils in **Chapter 6**, in which various regions on the body were investigated for cardiovascular motion components influencing the coils' impedance. Also data of a multi-channel approach for motion acquisition with a phase-array coil is shown. Two volunteers studies are described in this chapter, whereas the results of one study were presented in an oral presentation at the 23rd Annual Meeting of the ISMRM in Toronto, Ontario, Canada in 2015 [Kudielka et al., 2015]. Findings of the second study were submitted as a full paper to the journal "IEEE Transactions in Biomedical Engineering" (IEEE TBME) in May 2016 [Kudielka et al., 2016b].

Part Three discusses the results of this work, shows the advantages and limitations of the investigated motion detection method and provides an outlook for product implementation and clinical usage in the future. As this thesis was conducted during the employment as Research Scientist at GE Global Research, contribution to projects partly beyond the scope of this thesis was made, such as material science [Kudielka et al., 2015a], optical motion detection [Kudielka et al., 2015b] and cardiac imaging [Bustin et al., 2016].

Part I

Fundamentals and Methods

1 Magnetic resonance imaging (MRI) and the problem of motion

The principles of nuclear magnetic resonance were detected by Purcell [5] and Bloch [6] in 1946. This discovery allowed the spectroscopic investigation of material and is used in chemistry even today. Lauterbur [7] and Mansfield [8] developed spatial encoding on the nuclear magnetic resonance (NMR) signal and founded NMR imaging or magnetic resonance imaging (MRI). For the first time, a method was provided that could generate tomographic images of the human body without the use of ionizing radiation. This had a significant impact on medical diagnosis, and Lauterbur and Mansfield were awarded the Nobel Prize in Physiology or Medicine in 2003.

In this chapter, a short theoretical background of NMR and the spatial encoding to an MRI image are given (Section 1.1). The hardware of MRI systems is explained in Section 1.2. Furthermore, the influence of motion on the MRI signal is addressed in Section 1.3. Strategies to avoid or correct for motion-distorted images are introduced, with a focus on various motion-tracking techniques (Section 1.4.4). In addition, the anatomy and physiology of breathing organs, the heart, and the blood circulation, as well as their influence on MRI imaging are explained in Section 1.3.2, and specific solutions for motion correction in cardiac magnetic resonance imaging (CMR) are addressed (Section 1.4.5).

It must be mentioned that the nomenclature for the parameter $\vec{B}$ has been simplified in the MRI-community and is physically incorrect. The term "magnetic field" has become a commonly accepted description of $\vec{B}$, though it describes rather the "magnetic flux density" with the unit of $[\vec{B}] = \mathrm{Vs/m^2} = \mathrm{T}$. This work follows the nomenclature by the MR community with $\vec{B}_0$ as the external or main magnetic field and $\vec{B}_1$ as the excitation field.

1.1 The Nuclear Magnetic Resonance signal - from nuclear spin to image

1.1.1 The magnetic moment of spins

The NMR phenomenon is based on physical principle that atomic nuclei with an angular momentum or spin $\mathbf{I}$ show an magnetic moment $\boldsymbol{\mu}$

$$\boldsymbol{\mu} = \gamma\hbar\mathbf{I} \tag{1.1}$$

with $\hbar$=h/2π, h as Planck's constant and the gyromagnetic ratio γ, which is characteristic to every nucleus. Since the human body consists of 60% water [9], the ^{1}H

nucleus is the most relevant for MRI imaging. For the ^{1}H nucleus, the gyromagnetic ratio is defined as $\gamma(^1\mathrm{H}) = 42.58$ MHz T^{-1}. On applying an external magnetic field B_0, the proton aligns in 2I+1 possible orientations to this magnetic field. This alignment is defined by magnetic quantum number m, which is m=$\pm\frac{1}{2}$ for the ^{1}H nucleus. The energy of each individual orientation in a magnetic field is defined by the Zeeman effect as

$$E_m = -\gamma\hbar m B_0 \tag{1.2}$$

and with the magnetic quantum number for hydrogen, a energy difference between the two possible orientations can be calculated as

$$\Delta E = \left(\frac{1}{2} - \left(-\frac{1}{2}\right)\right)\hbar\omega_0 = \hbar\omega_0 \tag{1.3}$$

where ω_0 is the Larmor frequency

$$\omega_0 = \gamma B_0. \tag{1.4}$$

The ratio of the population to the different energy levels is described by the Boltzmann distribution

$$\frac{N_\uparrow}{N_\downarrow} = \exp\left(\frac{\Delta E}{k_B T}\right) \tag{1.5}$$

where $N_\uparrow$ and $N_\downarrow$ are the number of spins oriented parallel and anti-parallel to the magnetic field, k_B is the Boltzmann constant and T the temperature. Since the energy difference ΔE is small compared to the thermal energy k_BT, only a small excess of spins in the parallel orientation can be detected. The spin excess SE depends on the main magnetic field B_0 and prescribed as

$$SE \simeq N\frac{\hbar\omega_0}{2k_B T}. \tag{1.6}$$

For a temperature T=310 K (T = 36.85 °C) and a magnetic field of B_0=3 T the spin excess is 9.87 ppm of the total number of spins N in the volume. This fraction of protons contributes to the net magnetization and therefore to the NMR signal.

The typical main magnetic field strength in MRI reaches from 0.2T to 7T and higher in NMR. For comparison, the magnetic field strength of the earth is at 40-70μT. In practise, the macroscopic magnetization $\vec{M}_0$ is measured in NMR, which reflects the sum of magnetic moments in a sample and, hence, the parallel spin excess.

$$\vec{M}_0 = \sum_i^N \mu_i \approx \frac{N\gamma^2\hbar^2 B_0}{4k_B T} \tag{1.7}$$

The magnetization vector is not totally aligned to the the main magnetic field, but precesses around its axis. The potential energy level of the magnetization $\vec{M}_0$ in a magnetic field is then given by

$$E = -\vec{M}_0\vec{B}_0 = -|\vec{M}||\vec{B}_0|\cos\alpha \tag{1.8}$$

and depends on the angle α between the magnetization and the magnetic field (Fig 1.1). The transverse component $\vec{M}_{xy}$ of $\vec{M}_0$ with

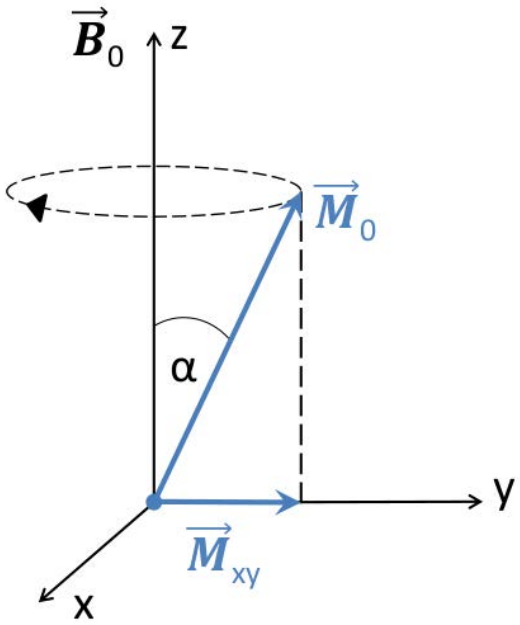

Figure 1.1 – Illustration of the magnetization vector $\vec{M}_0$ in a magnetic field $\vec{B}_0$ along z-axis and $\vec{M}_{xy}$ its transverse component related to angle α

$$\vec{M}_{xy} = \vec{M}_0 \sin\alpha \tag{1.9}$$

generates a temporal varying magnetic field as it precesses in the transverse plane (Fig 1.1). According to Faraday's law of electromagnetic induction, a voltage U is induced in a coil by a temporal varying magnetic flux ϕ_m

$$U(t) = -\frac{\mathrm{d}\phi_m}{\mathrm{d}t} \tag{1.10}$$

The magnetic flux of the transverse magnetization M_{xy}, therefore, generates a oscillating voltage in imaging coils oriented perpendicular to the main magnetic field B_0. This voltage holds the image signal and decays exponentially - the so called free induction decay (FID)- during the relaxation process, as explained in the next section.

1.1.2 Excitation and Relaxation of nuclear spins

Excitation

In the equilibrium state the induced voltage in Eq. 1.10 is very small because $\left|\vec{M}_0\right| \gg \left|\vec{M}_{xy}\right|$ and $\alpha \to 0$. In order to detect a reasonable signal, $\vec{M}_0$ needs to be tipped towards the x-y plane, which is achieved by a rotating magnetic field B_1 perpendicular to the main magnetic field B_0. This excitation field is generated by an radio frequency (RF) pulse in resonance with the Larmor frequency ω_0 and results in a flip angle

$$\alpha = \int_0^\tau \gamma \left|\vec{B}_1(t)\right| dt \tag{1.11}$$

with τ being the pulse duration of the applied RF excitation pulse. A complete rotation of $\vec{M}_0$ into the transverse plane is achieved by an $\pi/2$ pulse or flip angle $\alpha = 90°$. Similarly a π-pulse or an 180° flip angle rotates the magnetization in the negative z-plane. In MRI pulse sequences, typically, flip angles of $\alpha = [1°, 90°]$ are used. In the spin echo pulse sequence an $\alpha = 180°$ flip angle is applied for spin rephasing.

Relaxation

During RF energy supply, the magnetization vector changes its alignment with respect to the main magnetic field. By switching the RF pulse off, the spins begin to emit the absorbed energy and the magnetization reverts to the thermal equilibrium state. This time-dependent evolution of the macroscopic magnetization $\vec{M}$ is called relaxation and has been described first by Bloch as

$$\frac{\partial \vec{M}}{\partial t} = \gamma \vec{M}(t) \times \vec{B}(t) - \vec{R}[\vec{M}(t) - \vec{M}_0], \tag{1.12}$$

where $\vec{R}$ denotes as the relaxation matrix.

$$\vec{R} = \begin{bmatrix} 1/T_2 & 0 & 0 \\ 0 & 1/T_2 & 0 \\ 0 & 0 & 1/T_1 \end{bmatrix}, \tag{1.13}$$

The components of $\vec{R}$ are called relaxation rates. T_1-relaxation is the energy loss of spins to the surrounding environment or lattice, also called spin-lattice relaxation. It describes the relaxation of the longitudinal component $\vec{M}_z$ of the magnetization $\vec{M}$ to the magnetization at thermal equilibrium M_0 by

$$M_z(t) = M_0 * \left(1 - e^{-\frac{t}{T_1}}\right) \tag{1.14}$$

T_2-relaxation describes the loss of phase coherence of the spins in the xy-plane, caused by interactions between spins. Therefore T_2-relaxation is also called spin-spin relaxation. These losses effect the transverse magnetization M_{xy} by

$$M_{xy}(t) = M_0 * e^{-\frac{t}{T_2}} \tag{1.15}$$

T_1 and T_2 relaxation times refer to about 63% and 37% of the magnetization decay respectively. They are unique for every tissue type and depend on the main magnetic field B_0. Fig. 1.2 visualizes the difference between the relaxation times of grey matter and muscle tissue at 3T.

Imperfections in the B_0 homogeneity, susceptibility changes on tissue borders or external effects on the magnetic field (e.g. implants) cause destructive interference between the various magnetization vectors, resulting in a faster T_2 decay. All these effects are summed up in a T'_2 time and the resultant faster total decay $T_2{}^*$ can be calculated from

$$T_2^* = \left(\frac{1}{T_2} + \frac{1}{T_2'}\right)^{-1} \tag{1.16}$$

However T'_2 effects on static objects are constant over time and allow a reversal by rephasing methods like spin echo. Depending on the echo time TE on when the signal

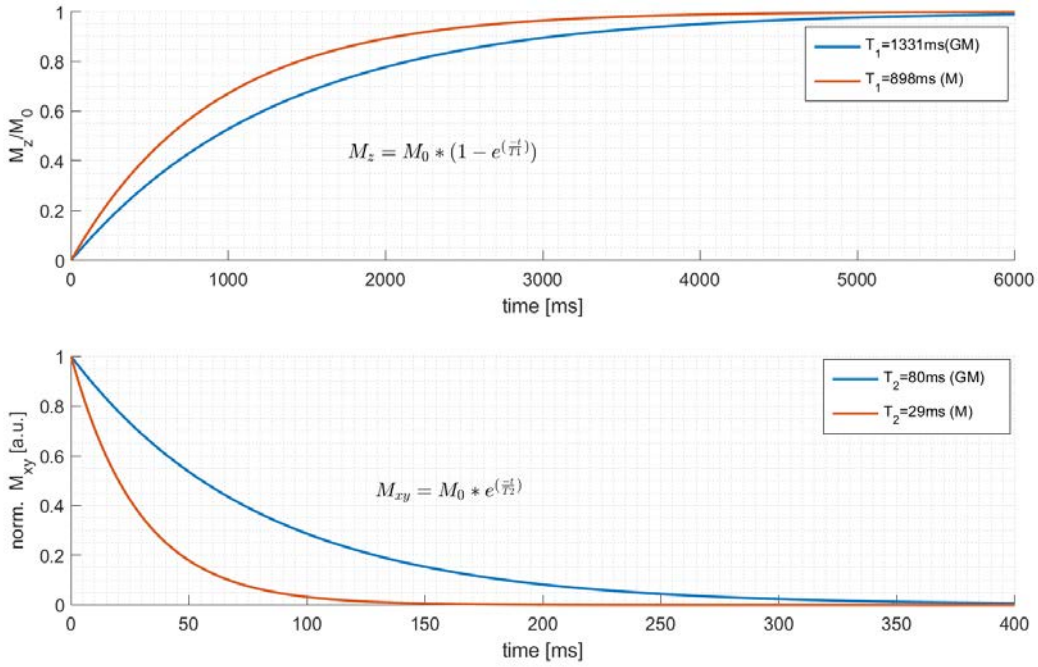

Figure 1.2 – T1- (top) and T2-relaxation (bottom) for grey matter (GM) and muscle tissue (M) at 3T; values taken from [10] for grey matter and [11] for muscle tissue

is acquired, different signal intensities are measured for the different tissue types in the field of view (FOV), which results in different contrasts in the MRI image. As described already, the excitation and relaxation of the spins takes place on the whole sample without any spatial break down. The principle of spatial encoding will be explained in the following.

1.1.3 Spatial encoding and signal detection

Spatial encoding of the magnetization

The principle of NMR imaging is the assignment of a spin at a spatial location to a unique Larmor frequency. This is achieved by additional constant magnetic field gradients in all three dimensions ($G_x = \frac{\partial B_z}{\partial x}$, $G_y = \frac{\partial B_z}{\partial y}$ and $G_z = \frac{\partial B_z}{\partial z}$). These field gradients are produced by gradient coils inside the magnet tunnel. Three sets of coil windings provide a linear field change in the X-, Y- and Z-axis. With the applied magnetic field gradients, the Larmor frequency becomes a function of the location r with

$$\omega_0(r) = \gamma(B_0 + \vec{G}\vec{r}) = \gamma(B_0 + G_x x + G_y y + G_z z). \tag{1.17}$$

The time-dependent NMR-signal amplitude S(t) depends now on the spin density of the volume ρ and its spatial Larmor frequency $\omega_0(r)$ at position $\vec{r}$.

$$S(t) = \iiint \rho(\vec{r}) e^{i\gamma \vec{G}\vec{r}t} d\vec{r}. \tag{1.18}$$

This equation describes a Fourier transformation. By introducing the reciprocal space vector $\vec{k}$,

$$\vec{k} = \frac{\gamma \vec{G} t}{2\pi} \tag{1.19}$$

and by inserting $\vec{k}$ in Equation 1.18, the signal S becomes

$$S(k) = \iiint \rho(\vec{r}) e^{i2\pi \vec{k}\vec{r}} d\vec{r} \tag{1.20}$$

and by taking the reverse transform we get the spin density ρ

$$\rho(\vec{r}) = \iiint S(k) e^{-i2\pi \vec{k}\vec{r}} d\vec{k}. \tag{1.21}$$

The application of magnetic field gradients differentiates between "slice selection," "phase encoding," and "frequency encoding." The slice-selection gradient applied during the RF pulse excites spins in a specific area rather than in the entire subject. This procedure is called selective excitation, in contrast to non-selective excitation without applying the gradient. The width of this area, or slice thickness, is defined by the bandwidth of the RF pulse and the slope of the slice-selection gradient.

In a Cartesian acquisition scheme both the phase- and frequency-encoding gradients are applied prior to and during signal sampling respectively. These gradients impress a specific frequency and phase on the spins according to their spatial position in the excited slice. The signal received by the imaging coil can described as

$$S(k_x, k_y) = \iint \rho(x, y) e^{i(k_x x + k_y y)} dx dy \tag{1.22}$$

where k_x and k_y are the coordinates in the k-space domain. k_x describes the frequency encoding and is determined by frequency encoding gradient strength G_x, the sampling or dwell-time t_d and the index n_x of N_x frequency encoding steps with $n_x = [-\frac{N_x}{2}, \frac{N_x}{2}]$:

$$k_x = \frac{\gamma G_x (n_x t_d)}{2\pi} \tag{1.23}$$

For phase encoding k_y is determined by the duration t_{ph} of the phase encoding gradient strength G_y, which varies for every phase encoding step n_y

$$k_y = \frac{\gamma (n_y G_y t_{ph})}{2\pi} \tag{1.24}$$

For each encoding step n_y, the FID provides one line in the k-space of N_x sample points (Fig. 1.3). After N_y iterations with a repetition time TR, a full 2D Cartesian grid is sampled and an image of the spin density $\rho(x, y)$ can be reconstructed by 2D Fourier transformation. This read-out technique is called Cartesian read-out. Other non-Cartesian methods exist - e.g. radial or spiral sampling - which typically reduce the total scan time and are utilized in fast imaging sequences.

Signal detection

In [12] the signal induced in the coil by the sample magnetization at any point in space is directly proportional to the B_1 field that would be generated in the same

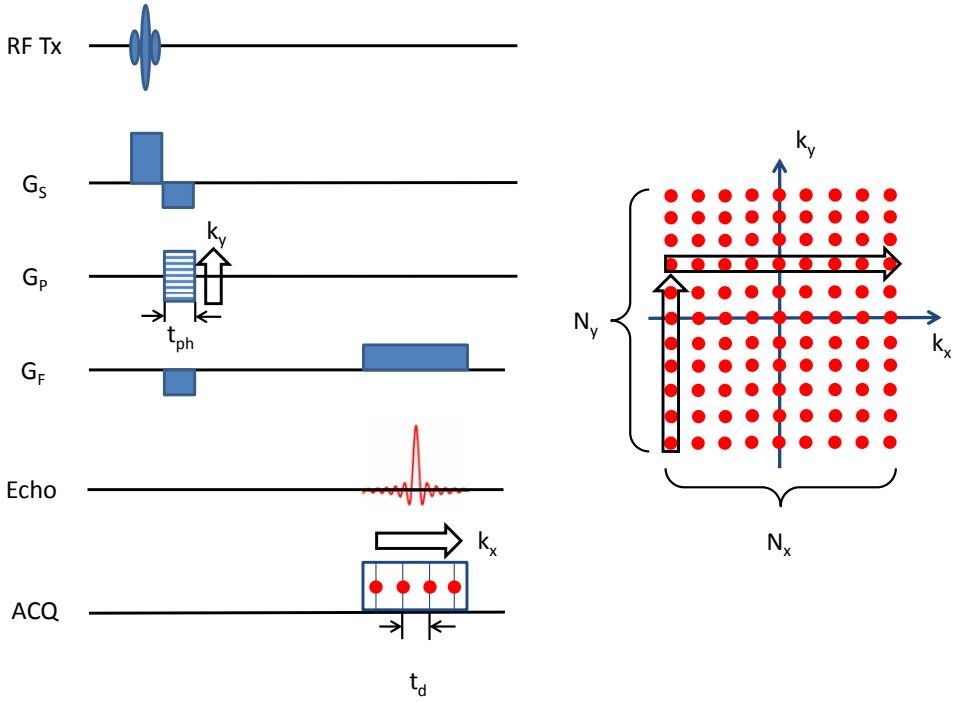

Figure 1.3 – Schematic of a MRI pulse sequence with k-space sampling; RF Tx = RF excitation, G_S = slice selective gradient, G_P = phase encoding gradient, G_F = frequency encoding gradient, Echo = receive signal, ACQ = acquisition window, N_x, N_y = k-space matrix size, t_{ph} = phase encoding duration, t_d = dwell or sampling time

point by unit current passing through the coil. Hence, a rotating dipole $\vec{m}$ in close proximity of the coil generates a higher induced voltage U, than one further away. Equation 1.10 can be expanded to

$$U_S(t) = -\frac{\partial}{\partial t}(\vec{B_1} \cdot \vec{m}) \tag{1.25}$$

This important relationship is called the principle of reciprocity. The induced signal of a sample volume V can be derived from the magnetic fields $\vec{B_1}$ of all points $\vec{r}$ in the volume and the transverse magnetization $\vec{M}_{xy}$ in these points

$$U_S(t) = -\int \frac{\partial}{\partial t}(\vec{B_1}(\vec{r}) \cdot \vec{M}_{xy}(\vec{r}))dV. \tag{1.26}$$

The principle of reciprocity shows that the transmitted magnetic field at each position $\vec{r}$ is proportional to the coil's sensitivity. For optimal results the filling factor η and quality factor Q of the coil should be as high as possible. This is explained in further detail in section 2.1.3.2.

1.2 MRI system hardware

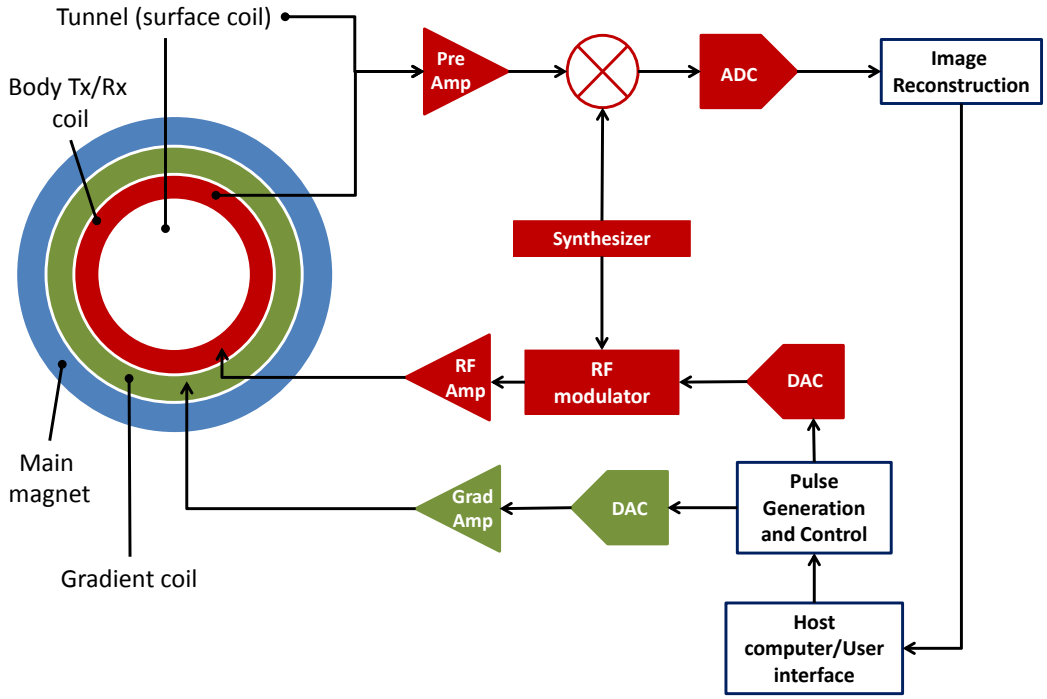

Figure 1.4 – Schematic of a MRI system. green: Gradient sub-system, red: RF sub-system, blue: magnet

The schematic of an MRI system is shown in Figure 1.4. The main components are nested into each other and are placed inside a RF shielded room. The magnet is the supporting structure, generating the main magnetic field. Inside the magnet sit the gradient coils and the body Tx/Rx coil. Inside the MRI tunnel (or inside the body coil), the patient is placed with a dedicated surface coil. The components and their control electronics are explained more in detail in the next paragraphs.

The MRI magnet

The magnet produces a strong, static and homogeneous magnetic field B_0 with a magnetic field strength of 1 to 3 T in clinical systems and up to 7 T and higher in research. The homogeneity is adjusted either by active shim coils producing corrective fields or passively by placing small ferromagnetic plates along the field direction. A homogeneity of <4 ppm over 500 mm area is typically achieved by the shimming. Modern MRI magnets are superconducting magnets and use the property of superconducting materials of zero resistance at temperatures near the absolute zero or 0 K. The imprinted current during the ramping process is circulating indefinitely as long as the magnet winding is sufficiently cooled. The magnet coil windings are placed inside liquid helium with a temperature of 4 K. As this substance is volatile and difficult to produce, recycling mechanisms are in place to reduce the

helium boil-off. In case of an emergency, the magnetic field would need to be shut-off immediately. This is performed by the so called "quench", where the helium is completely released through a quench pipe. The windings are no longer cooled and the magnet field breaks down.

Other magnetic designs e.g. open magnets are electromagnets or permanent magnets, however with a lower magnetic field of e.g. 0.35 T (Fig. 1.5).

(a) GE 1.5T 450w MRI system (b) GE 0.35T Ovation MRI system

Figure 1.5 – Example of different MRI system: a) 1.5T superconducting magnet b) 0.35T permanent magnet

The gradient system

The gradient coils produce linear magnetic field variations of about 50 mT/m in all three spatial axis, which superimpose the B_0 field. This allows the spatial encoding by frequency and phase variation of the spin signal. Depending on the image plane orientation, the coils are driven either as slice-selective gradient, frequency-encoding gradient or phase-encoding gradient. The timing of the activation and the pulse shape is defined by the pulse generation unit. After the conversion to an analog waveform by a digital-to-analog converter (DAC), the signal is amplified individually on each axis, whereas the amplifier performance defines the slew rate of the system.

The RF system

The RF system comprises of a transmitter path, the transmitting coil, the receive coil and a receiver path. The transmitter signal (Tx) generates an alternating B_1 field in the transmit coil, which rotates the magnetization vector of the protons towards the xy-plane. The pulse generator defines the pulse shape, duration and bandwidth of the excitation pulse, which is modulated to the Larmor frequency by the frequency synthesizer. A DAC converts the RF signal into a analog waveform, which is routed to the RF amplifier and to the transmit coil. The RF amplifier output rating is typically about 30 kW in body mode and 4 kW in head mode. For safety assurance, the RF amplifier compares the transmitted power with the reflected power from the coil by directional couplers inside the amplifier. This measurement detects transmit

coil malfunctions and is used to calculate the efficient SAR value during the imaging scan.

Similarly the receive signal (Rx) is demodulated to the sampling frequency of the analog-to-digital converter (ADC). On modern MRI systems, ADCs with sampling rates of 100 MHz and more allow direct sampling and do not need preceding demodulation. The receive signal of view millivolts however needs to be amplified first by an low-noise pre-amplifier to enhance the signal by about 20 dB and reduce noise and matching losses. The analog part of the RF system has a system impedance of 50Ω and each component has to match to this system impedance for optimized signal or power transfer.

Parts which are not shown in the schematic are the transmit-receive or T/R-switch and hybrid splitter on Tx/Rx body coil. The T/R-switch connects the coil to the dedicated path during the pulse sequence, when the coil is used in both modes - in transmit and receive mode. The hybrid splitter divide the RF signal into two path (an I channel and a Q channel) with a 90° phase shift to achieve quadrature drive.

RF coils are an essential part of the MRI system. They are explained in detail in Section 2.1.4.

1.3 Motion in MRI

The sequential encoding principle of MRI, and the time between the excitation of spins and the acquisition of image data, result in a higher vulnerability to motion. Patient motion can be split into two categories: bulk body motion (voluntary or involuntary) and physiological motion.

An MRI exam can last up to 45 minutes, during which the patient has to lie still inside the MRI bore. Voluntary movements to more comfortable positions can occur after a certain period. Claustrophobia or general fear in non-compliant or deranged patients and children typically result in voluntary patient motion. Involuntary motion can be the relaxation of the body during scanning, swallowing, sneezing, wincing when falling asleep or being startled by gradient noise, as well as periodic movements caused by neurological diseases like head tremor. Physiological motion is generated by subconscious muscle contraction. This can be the breathing motion of the diaphragm and lungs, heart motion and blood flow or peristaltic motion of the bowel.

Movements during MRI image generation degrade the image quality. The effect of inter-view (between different phase encoding steps) and intra-view motion (between RF excitation and acquisition) during an imaging sequence is explained further in Section 1.3.1. Further effects of motion on the B_0 field are also explained therein. An overview of motion prevention and correction methods is given in Section 1.4.

Since this work focused on cardiac MRI imaging, the physiology of the heart, blood flow, and respiration is addressed in Section 1.3.2.

1.3.1 Image artifacts caused by motion

The type of motion and the time of occurrence in the MRI pulse sequence determine the motion degradation in the image. In Section 1.1, the evolution of the ^{1}H nuclei magnetization after excitation and spatial encoding is described for the case of static objects. Motion, however, causes a change of the spins' imprinted phase or frequency information, which results in different k-space information and, hence, different image information. One can distinguish between intra-view, inter-view motion or through-plane motion, depending on when during the pulse sequence the spin manipulation by motion takes place. In addition, local magnetic field inhomogeneities occur by position changes of tissue, known as susceptibility effects.

Intra-View motion

Motion that occurs during the TE time is called intra-view motion. At the frequency-encoding gradient activation, spins with the same phase encoding are sampled. Continuously moving spins experience a phase change during this read-out gradient and artifacts occur in the image as a broad phase distribution. Due to the typically short duration between RF excitation and the image acquisition of a few microseconds to milliseconds, only rapid motion, such as blood flow, affects the image. Hence, these effects need to be taken into account particularly in cardiovascular imaging, as they lead to signal loss caused by spin dephasing.

Inter-View motion

If motion appears in between sequence repetitions or between two phase-encoding steps, the phase information becomes inconsistent from one k-space line to the other. Since typical TR times range from milliseconds to seconds, the motion of slower velocity as physiological or patient motion, can have an influence on the image.

In brain imaging, rigid head motion, like translation and rotation, is the main source of motion artifacts [13]. The effect on the k-space is well understood and reported in [14] and [15]. A position change of an object from position (x,y) by a distance (d_x,d_y) causes a linear phase shift in k-space. Rotations of that object of the angle θ results in a rotation at the same angle in k-space. These behaviors are typical properties of the Fourier transform and are also known as Fourier shift theorem (Eq. 1.27) and Fourier rotation theorem (Eq. 1.28) respectively, with f(x,y) as the position in space and F(k_x,k_y) its Fourier transform in k-space

$$\mathcal{F}(f(x-d_x, y-d_y)) = F(k_x, k_y)e^{-i2\pi(k_x d_x + k_y d_y)} \tag{1.27}$$

$$\mathcal{F}(f(x\cos\theta - y\sin\theta, x\sin\theta + y\cos\theta)) = F(k_x\cos\theta - k_y\sin\theta, k_x\sin\theta + k_y\cos\theta) \tag{1.28}$$

Head tremor or respiratory motion are typically periodic movements. The effect of periodic motion on k-space was described by Wood et. al in [16] and [17]. The periodic motion was analyzed by the convolution of the point spread function (PSF) of motion to the phase encoding of image data. Blurring occurs with a wide band PSF, whereas ghosting is caused by frequent oscillations and applies as multiple copies of the image along the phase-encoding direction. Figure 1.6 gives an example of these effects in a cardiac image.

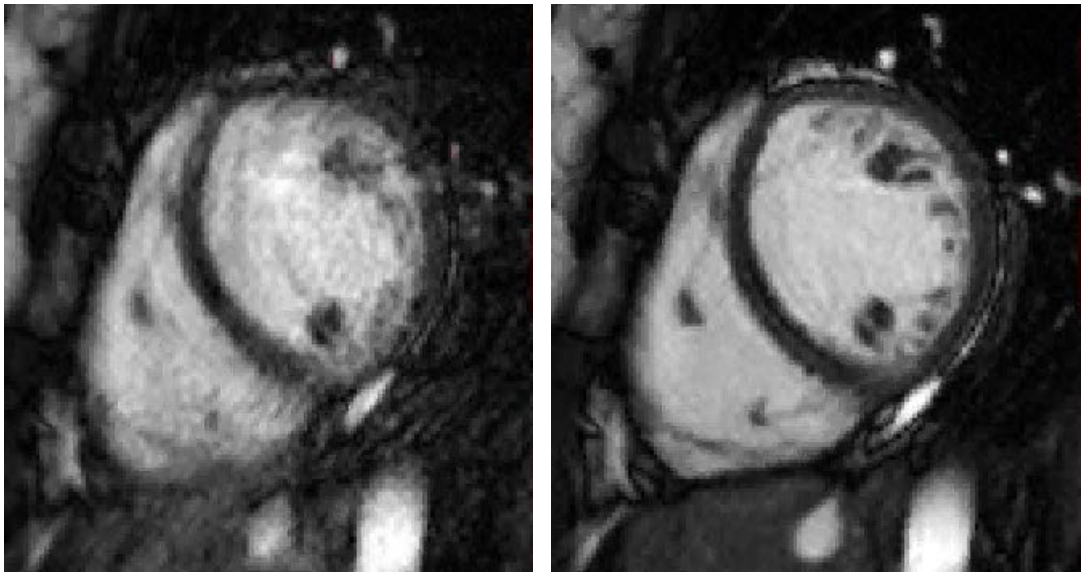

(a) blurring due to motion (b) no motion

Figure 1.6 – Example of blurring in a short-axis heart image; a) blurred image, b) breath-hold image

Through-plane motion

Besides these in-plane k-space effects, motion can also lead to through-plane distortions. This is the case when the object moves not in parallel to the imaging plane but through it. The mismatch between the spin exciation and read-out causes signal voids and geometric distortions in temporal subsequent images. Through-plane motion plays a role particularly in cardiac imaging since the heart performs a complex 3D deformation during the cardiac cycle (see Section 1.3.2) and moves through a specified 2D image plane. Especially in quantitative cardio-physiologic measurements, through-plane motion could lead to an overestimation of end-systolic ventricular volumes [18].

Susceptibility effects

The main B_0 field is modified by the magnetic susceptibility of the various tissue types and interfaces with different susceptibility and geometrical properties. As the patient moves inside the B_0 field, these local susceptibility changes vary with the motion. Even image acquisition of distant body parts like the brain, can be affected by magnetic susceptibility variations from respiratory motion [19]. Influences are reported also on breast imaging [20], spinal cord imaging [21] and spectroscopy [22, 23]. With higher magnetic field strength, the effect increases, as susceptibility variations result in higher magnetic field alterations and thus in more pronounced image artifacts.

1.3.2 Physiological motion in Cardiac MRI

The chest area holds various sources of physiological motion with different motion velocities, which challenges MRI in this area. In cardiac imaging, care needs to be taken for respiratory motion, heart motion, and fast blood flow. In the following, these motion types and its corresponding anatomy are explained further.

1.3.2.1 Respiratory motion

The periodic volume change of the lung is achieved by the movement of the diaphragm and the contraction of the intercostal muscles. The diaphragm accounts for 75% of the respiratory movement and pushes abdominal organs like the liver, kidneys or bowel in the superior-inferior direction on inspiration. The intercostal muscles lift the rib cage in an anterior-posterior direction and increase the diameter of the chest. This also causes a superior-inferior shift, a deformation of the heart and hence a 16% and 14% variation of the left- and right-ventricular cross-sectional areas respectively [24]. In this publication, variations of the blood flow in the aorta, pulmonary artery, and veins, caused by the inspiration and expiration chest motion, are shown as well. The motion frequency for breathing at rest is typically in the range of 0.1 Hz to 0.4 Hz. The average breathing volume or tidal volume at rest is between 500-750 ml [25] but the total lung capacity is 5,000 ml.

Breathing physiology varies between patients and during the imaging exam, e.g. when the patient falls asleep. Primary abdominal breathing with the main diaphragm motion can change to chest-focused breathing with a major contribution of

the intercostal muscles. In Fig. 1.7, the signal of a pneumatic belt at the chest and at the abdomen is compared between two volunteers. One volunteer clearly shows primary chest breathing with a diaphragm motion out-of-phase, while both belts are in sync for the other volunteer with primary abdominal respiration. As reported in Section 1.4, various methods can be used for respiratory motion acquisition. The positioning of the motion sensor (e.g. navigator, marker, probe) has to address this different breathing physiology and is critical for signal reliability.

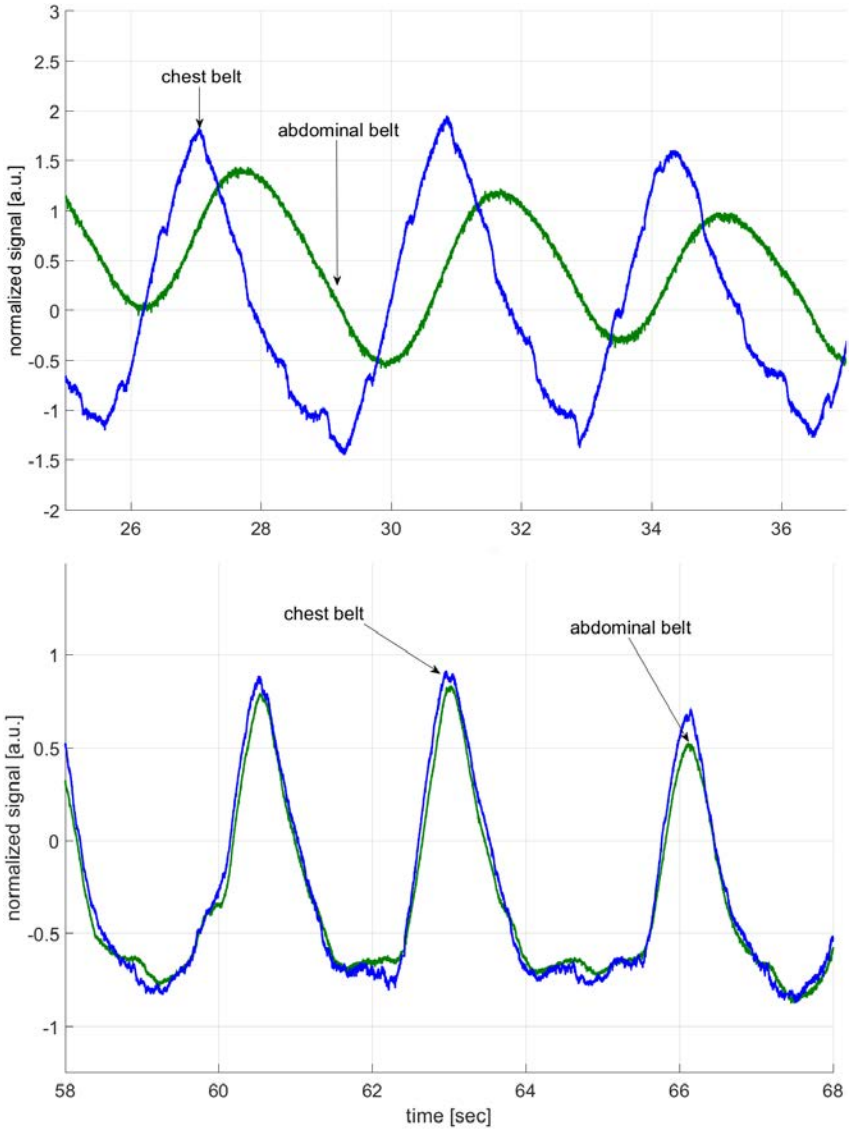

Figure 1.7 – Belt signal of two different breathing pattern; top: chest focused breathing with a phase shift in the abdominal belt; bottom: abdomen focused breathing with both belts in phase

1.3.2.2 Mycardial mechanics

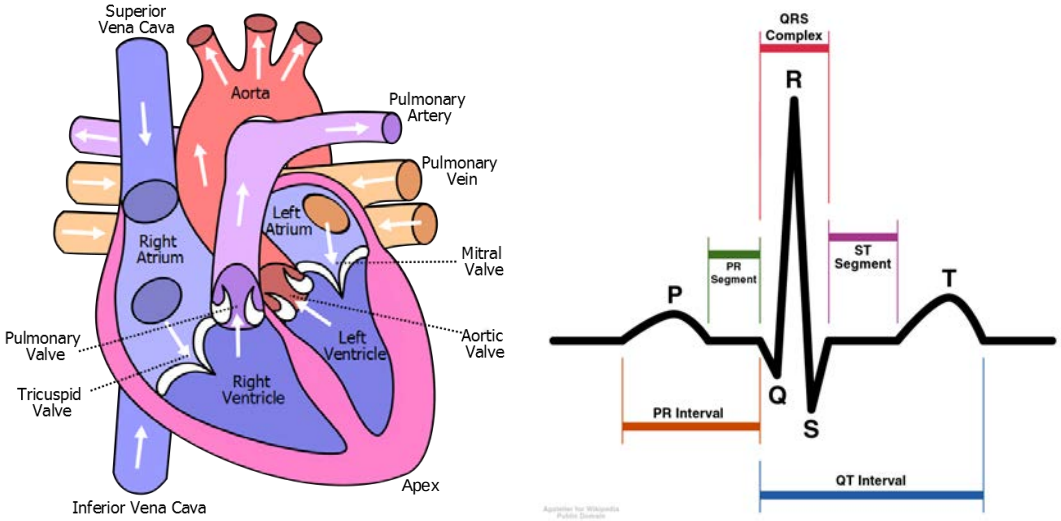

(a) Anatomical diagram of the human heart (b) ECG diagram

Figure 1.8 – Anatomy of the human heart and ECG

Anatomy of the heart

The human heart muscle sits behind the sternum, slightly off-center with its tip - the apex - pointing toward the left (Fig. 1.8a). It is divided into four chambers. The upper left and right atria receive blood from the larger vein vessels (superior and inferior vena cava) and the pulmonary veins respectively. The lower right ventricle forwards the deoxygenated blood via the pulmonary arteries to the lungs. The oxygenated blood is then pumped by the left ventricle into the aorta and the arterial circulation system. Four valves control the blood flow between the atria, the ventricles, and the arteries. They work as one-way outlets and are located in the basal plane. The myocardial muscle performs a complex movement while contracting. The left ventricular (LV) movement during systole is described in three components [26, 27]: longitudinal shortening of the basal plane toward the apex, counterclockwise radial contraction, and rotation of the apex relative to the base. The right ventricle (RV) shows primarily longitudinal contraction with an element of radial contraction toward the apex.

Electrical activity and temporal phases

The mechanical contraction of the muscle occurs by electrical activation of the muscle itself. The electric potential change can be measured by an electrocardiography (ECG) recording on the chest surface (Fig.1.8b). The heart performs between 50 and 80 contractions per minute (or beats per minute [bpm]) at rest and up to 180 to 200 bpm under stress. This corresponds to a motion frequency of 0.83 Hz to 3.33 Hz. The heart cycle can be split into two phases - the systole and the diastole. In the systolic phase, the atria and the ventricles contract successively and push the blood volume in the lung or the arterial circulation system. The ECG represents

this activation in the PR interval (atria activation) and the QRS complex (ventricle contraction). The systolic phase lasts between 270 ms (at 65 bpm) and 160 ms (at 200 bpm) [25]. In the diastole, the heart muscle relaxes and blood flows from the atria into the vessels. About 70% of the blood volume flows passively into the ventricles, while the rest is pushed in the early systolic phase by atrial contraction. This phase lasts 530 ms and 140 ms respectively, and is represented in the ECG by the ST and TP segments. During the end-diastolic phase, the heart motion is at its minimum. For high-resolution CMR, this period is the preferred state for image acquisition.

Volumetric parameters

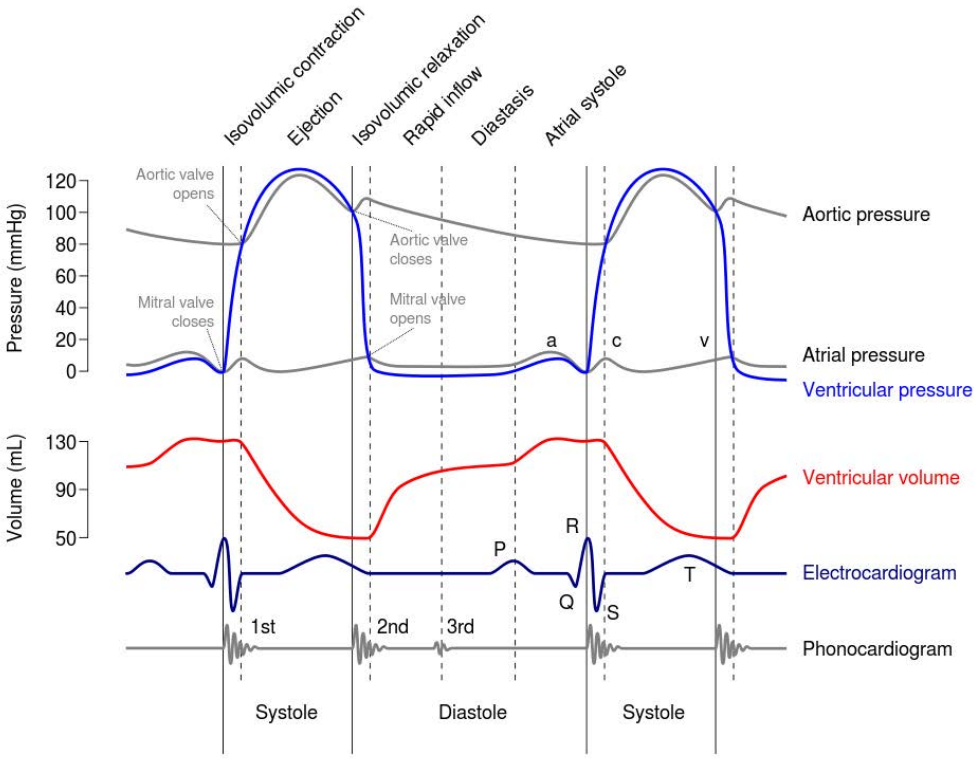

Figure 1.9 – Wiggers Diagram of cardiophysiologic pressure and flow

The average stroke volume (SV) - the blood volume pumped out with every heartbeat - is between 70 ml [25] and 100 ml [28] per ventricle at rest, which sums up to an average cardiac output of 5.0 l/min. The temporal variation of the ventricular volume is illustrated in the Wiggers diagram (Fig. 1.9). At beginning of the systole, the end-diastolic volume (EDV) is increased by the atrial contraction. After the R-peak of the ECG, the volume stays constant during the isovolumetric phase and decreases rapidly with the opening of the aortic and pulmonary valves. The end-systolic volume (ESV) is the remaining blood volume in the fully contracted ventricle. During diastole, the ventricle fills up with blood again to the EDV. The average values of

ESV, EDV and the stroke volume SV for the left and right ventricles are listed in Table 1.

	Parameter	average range (men)	average range (women)
Left ventricle	EDV [ml]	106-214	86-178
	ESV [ml]	26-82	22-66
	SV [ml]	72-144	57-117
Right ventricle	EDV [ml]	118-250	77-201
	ESV [ml]	41-117	24-84
	SV [ml]	68-144	48-120

Table 1 – Volume parameters of atria and ventricles for adults, age 20-68. Values from [28]

1.3.2.3 Cardiovascular flow

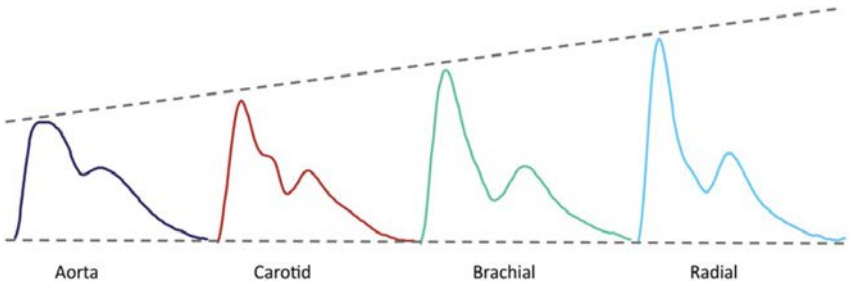

Figure 1.10 – Arterial pressure in different arteries. Due to decreasing diameter, the systolic pressure peak increases towards the periphery and the dicrotic notch is more pronounced.

The blood volume pumped out of the heart and into the circulation system builds up a pressure wave in the arteries that becomes palpable as the pulse. The large pressure of 120 mmHg is attenuated to 40 mmHg and converted into a continuous blood stream by the elasticity of the aorta (Fig. 1.9, Aortic pressure). The pulse shape shows a notch in the declining gradient, called the dicrotic notch. It is caused by the closing of the aortic valve and leads to a secondary pressure increase. As the pulse wave prolongs through the body, it takes a certain transit time (pulse transit time [PTT]) until it arrives in the peripheral arteries. The artery diameter decreases from the body center to the periphery. As a result, the pressure and the velocity of the pulse wave increase (Fig. 1.10). Typical pulse wave velocity (PWV) values are 4 m/s for the aorta, 8 m/s for larger vessels, and 16 m/s for smaller vessels [25]. PWV is the gold standard method to evaluate arterial stiffness, which is an indicator for cardiovascular risk [29]. It is typically measured by external pressure sensors and with Fourier velocity MRI techniques [30].

1.4 Motion artifact reduction and correction

Various techniques are currently available in research and practice to avoid or correct for motion-corrupted MRI image data. Since there is no gold-standard solution, a combination of these various methods could be used to improve image quality. The application of the different methods can depend on several parameters, like the body region to be imaged, patient or clinical environment and one has to use or combine the adequate instrument of the "motion correction toolbox". The various techniques can be split into three categories [31]: motion prevention, motion-insensitive imaging, and motion correction and are explained in the following.

The motion handling in cardiac MRI is specific to the physiological activity of the heart and lungs and is covered separately in section 1.4.5.

1.4.1 Motion prevention

By motion prevention, methods that disable the patient from moving or that train the patient to lie still for extended periods are summarized. Avoiding motion is obviously the best solution for stable image quality. Fixation with foam pads and belts, wrapping (on infants) or sedation (in children) are widely used. Also, training children in a mock MRI system [32] or respiratory feedback during the examination [33] can reduce the motion occurrence.

Breath-hold techniques in CMR

To avoid respiratory-induced motion artifacts, image acquisition in CMR is often performed during end-expiratory breath-holds. This requires fast imaging sequences with a total scan time of five to 20 seconds, and patient cooperation. However, it has been shown that breath-hold techniques are not feasible for every patient [34] or suffer from insufficient reproducibility of the breath-hold position [35]. In longer breath-hold periods, an involuntary drift of the diaphragm can occur at the end of the period, reducing the stability and reliability on the breath-hold state, which could have an impact on motion-correction techniques. Reliable breath-hold and reproducible organ position is reported with an active breathing coordinator used in radio-therapy [36]. The patient receives artificial respiration from the breathing coordinator. Also breath-holds are controlled by the system, which allows reproducible breath-holds in time and lung volume. This provides predictive respiratory motion states, although it requires patient acceptance and compliance.

1.4.2 Motion insensitive imaging sequences

In order to reduce the influence of motion already in the image acquisition, the user can apply alternative strategies. Averaging multiple acquisitions of an image can reduce ghosting artifacts, albeit with a penalty of a long scan time and reduced image resolution. Swapping the phase- and the frequency-encoding direction shift the motion direction in the less sensitive frequency-encoding axis, which could reduce the artifact or, at least, shift it out of the area of interest. Another method is the

usage of saturation bands. These bands saturate the spins in the applied area and lead to a signal void in the acquired image. Motion occurring in this area will not affect k-space properties.

With the analogy to photography, motion effects in an image are reduced the shorter the shutter time (or image acquisition) takes. Motion-insensitive imaging sequences aim for short imaging times, improved phase encoding, and reduced flow sensitivity. Synchronizing the MR sequence with the patient motion can be achieved by gating or triggering and allows image acquisition at the same motion state. The various methods are listed in the following.

Fast imaging techniques

Fast read-out techniques as echo planar imaging [37] reduce the motion influence. Also, fast gradient echo (FGRE) sequences with low-angle excitation [38], steady-state techniques [39], fast spin echo (FSE) sequences with echo-train methods [40] or single shot sequences practically "freeze" the motion state in the image. However, this is usually accompanied with a compromise in the signal-to-noise ratio (SNR) and the image resolution.

Parallel imaging

With the usage of multiple coil elements and the preliminary knowledge of the sensitivity profile, k-space undersampling is possible [41, 42]. The sensitivity profile is typically acquired in a calibration scan before the actual image acquisition. Combination of the signal of each coil element with the sensitivity profile allows undersampled reconstruction and reduces scan time typically by a factor two to three.

Phase reordering

In-plane motion results in ghosting artifacts in the phase encoding direction. Phase reordering is a method to reduce the effect of motion by synchronizing the phase encoding with the respiratory cycle [43]. The k-space line acquisition at a certain time relates to the respiratory motion state at this time. Such respiratory compensation techniques are preferred over respiratory gating, due to the significant shorter scan time.

Gradient Moment Nulling

Gradient moment nulling is a method used to overcome intra-view artifacts due to blood flow [44, 45]. Constant moving spins experience a phase shift during the activation of a standard bipolar gradient. An additional gradient lobe refocus moving spins and compensate for the dephasing. Since static spins behave equally, motion flow artifacts can be successfully reduced. One drawback of gradient moment nulling is the longer scan time caused by the application of the additional gradient lobe.

Non-Cartesian sampling

Non-Cartesian k-space sampling techniques as spiral [46] or radial [47] are less sensitive to motion influence, as the spin magnetization changes are sampled in various k-space positions. This leads to inconsistency of the artifact and, hence, it is less

problematic in the image. However the motion is still visible as blurring and SNR losses needs to be taken into account.

1.4.3 Motion correction

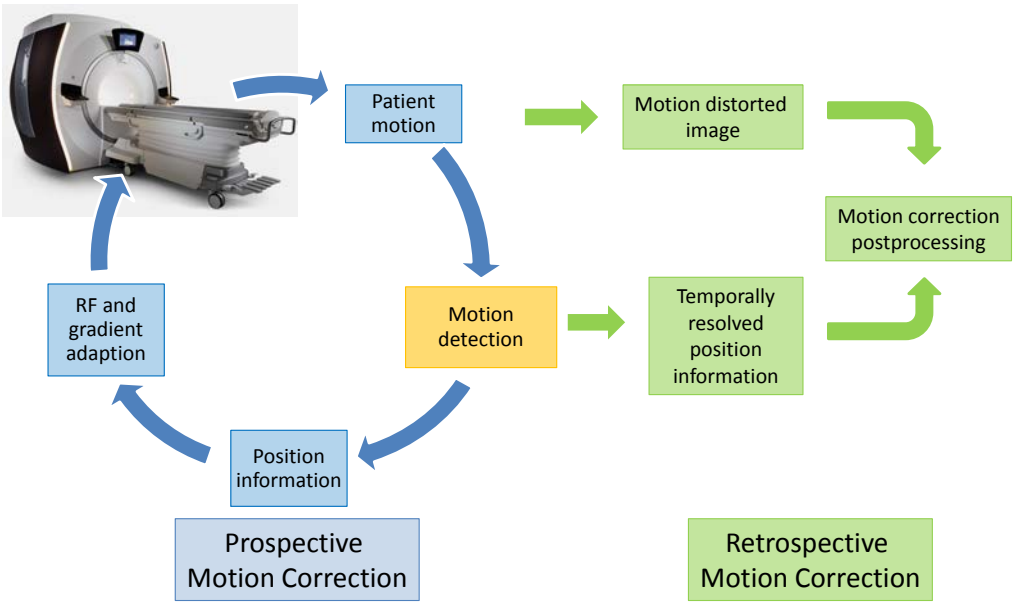

Figure 1.11 – Schematic of prospective and retrospective motion correction. Both methods are independent motion correction solutions, however they can be combined for enhanced image correction. Position information gathering by motion detection techniques is relevant for both methods

Motion-correction methods can be distinguished into prospective (before and during data acquisition) and retrospective motion-correction methods (after data acquisition) (Fig. 1.11).

Prospective techniques apply adaption to the image acquisition and sampling scheme, according to separately recorded motion data in real-time. Thereby, the gradients, RF excitation pulses, and receiver parameters can be adapted, and the acquisition volume follows the moving object [48]. Since the imaging parameters are adjusted "on the fly," this technique is independent of the imaging sequence and only minor changes for real-time correction are necessary. It has the further advantage of reducing the spin-history effect of through-plane motion and is independent of the imaging sequence [13]. High demands have to be made for the motion registration part. The detection and resulting correction parameters need to be completed in a very short time relative to the repetition time and motion frequency. Prospective motion is limited to rigid body motion or linear motion (e.g. respiration). Correction

of non-rigid motion is not possible due to the high computational effort, the time limitation and the limited gradient field control.

In retrospective motion correction, algorithms re-calculate the distorted images according to recorded motion information after the scan. The post-processing algorithm depends on the clinical application. Rigid motion, for instance, can be corrected by applying the Fourier theorems (Eq. 1.27 and Eq. 1.28)[49]. Elastic motion, as performed by the heart, requires more complex reconstruction solutions. In the GRICS method introduced by Odille et al. [50], images are reconstructed with a motion model, whereby both are adapted iteratively (see Section 3.4.2). Other solutions for retrospective correction are the partial k-space data correction [51] or the iterative k-t adaption of cardiac-triggered data [52]. Retrospective correction methods are typically computationally intensive and require a certain time period. In 2D images, they can also correct for in-plane motion only, which could lead to residual artifacts after correction.

1.4.4 Motion detection techniques

For both prospective and retrospective motion-correction techniques, motion information has to be acquired separately. Motion information could be also included in the image data itself (image based methods). The motion data needs to be analyzed in real-time to adjust scan parameters (prospective motion correction) or is recorded and used in post-processing (retrospective motion correction). Hence, different sources or sensors exist for motion registration and are described in the following.

Electro-mechanical sensors

Mechanical patient surface motion, such as the respiratory chest movement, can be captured by sensors that transform the mechanical motion into an electrical signal. One state-of-the-art solution for monitoring the breathing cycle is the application of a pneumatic belt (also called a respiratory belt) fixed on to the chest or abdomen of the patient [53]. The volume variation of the chest is reflected by the tension and contraction of the belt, and the corresponding pressure change can be acquired by a pressure sensor. Another method with a pressure transducer detecting the inhale and exhale flow is reported [54]. An accelerometer [55] and a piezo-electric transducer [56] are reported to deliver motion information about the chest and the head respectively.

Electro-mechanical sensors acquire the motion directly at its source and, hence, need to be fixed on to the patient. The positioning of the sensor is critical for signal stability and reliability.

Acoustic motion tracking

Especially for CMR, acoustic sensors can be used for cardiac triggering. Frauenrath et.al. [57] developed a microphone system to capture heart tones for cardiac triggering. Also doppler ultrasound transducers are reported as reliable trigger sensors for CMR [58, 59]. Two flow waves in the early and late diastole are caused by the filling of the ventricles. Both methods provide a direct mechanical motion representation

by the valve-closing tones or ventricular blood filling. However, a high sensitivity against breathing motion and sensor positioning is reported. Furthermore dedicated filtering needs to be applied to cancel out noise of gradient switching.

Optical motion tracking

Especially in brain imaging, camera systems are used to record head motion. The camera tracks a specific pattern on a marker which is fixated on the patient. There exist in-bore [60, 61] or out-bore solutions [48]. The latter have the advantage of reduced sensitivity to RF and magnetic field; however, dedicated mirror systems are additionally needed. Stereo cameras [62, 63] and time-of-flight cameras [64], [Kudielka et al., 2015b] provide 3D information which allow marker-less and physiological motion tracking. Other optical system can be found in optical fibre systems for respiratory gating [65] or laser [66].

In general, optical systems require a clear line-of-sight and stable mechanical fixation (for the camera and the marker) since gradient vibration or loose marker movement can falsify the motion data. In-bore systems need special shielding to withstand the high RF energies and magnetic fields. Due to this technical effort, such systems are primarily used in research.

NMR probes

NMR probes built by placing solenoid coil around a small sample are used to measure their position relative to the isocenter by applying gradient fields. These probes (typically three or more are used) are fixed on to the patient by dedicated holders. A localization scan is performed prior to the image acquisition in order to obtain the probe position in the gradient field by triangulation [67] or by position encoding for each individual probe separately [68]. This allows rigid body motion in all six degrees of freedom. That is why the method is typically used for head MRI imaging. The samples of NMR probes are made from different materials usually doped with some contrast agent. The NMR probes resonate at their material-specific frequency of ^{1}H [69], ^{2}H [70] or ^{19}F [71, 72]. Non-^{1}H probes allow continuous gradient-field monitoring during standard imaging sequences [72]. Motion induced gradient-field perturbation can be detected in first and higher orders. Especially in high field MRI (B_0>3T) the effect is more prominent.

The additional probe-mounting device and cables might increase patient discomfort. However, specific shielding against RF or magnetic fields is not needed, as the NMR probes utilize these fields occurring during the imaging process to capture motion.

RF field measurements

The electromagnetic properties of body tissue depend on the tissue type and vary with frequency (Section 2.3). RF waves can distribute through the body and are reflected at the tissue boundaries of different dielectric properties. Motion-dependent variations can be detected by dedicated systems. Ultra-wideband (UWB) radar was shown to be an MR-compatible motion detection system in cardiac imaging [73, 74]. UWB radar typically provides a broad bandwidth of 0-5 GHz; however, this needs to be limited for MR compatibility (e.g. 1-5 GHz). By placing multiple

neighboring transmit and receive units around the body, the motion along various axes can be captured. Respiratory motion was also measured using pick-up coils (PUC) distributed along the MR bore diameter [75]. Originally designed for power monitoring in parallel-transmission MRI systems, pick-up coils measure the current of the transmit coil during RF excitation. Due to coupling effects (see Section 2.1.3.2), the power varies with the respiratory chest movement, resulting in an aligned signal in the pick-up coils.

Utilizing the MRI imaging coil itself as a motion indicator was first reported by Buikman [76] by continuous measurement of the Q-value of the coil. This thesis further investigates the effect on coil loading changes. Recently, another approach for RF coil motion sensing was reported with the utilization of the coil's noise variance [77]. As thermal noise represents the losses resulting from the resistance of the coil, the measurement of the noise variance is an indicator for the motion-induced impedance change of the coil.

These techniques provide remote motion detection or, at least, no additional sensors (when using the imaging coil). The temporal resolution can be very high (e.g. 3.2 μs in [75]). However the measurement system needs to be placed inside the MR bore (UWB, PUC) and might be a complex setup. Filtering and post-processing techniques need usually to be applied.

Navigators

Navigators are integrated pre-pulses in the imaging sequence capturing the motion before the image acquisition. They record the motion in every sequence cycle in the k-space in 1D [15], 2D [78] and 3D [79]. Depending on the trajectory, motion data can be acquired in various directions and degrees of freedom. Image-space navigators acquire a low-resolution [80, 81] or fat-selective image [82] for motion information. With multiple coil elements, an FID navigator can give 2D information about the signal change in the elements caused by patient motion [83]. Pencil-beam navigators are widely used in clinical practice to track the motion of the diaphragm-lung border for respiratory gating. Acceptance windows can be defined to acquire image data only in the quietest motion states.

Navigators come along without any extra hardware placed on the patient, as they are fully integrated in the imaging sequence. However, they are not available on every pulse sequence as they require some time in the pulse sequence and need to be explicitly programmed. As a result, navigator sequences require longer scan times compared to non-navigated sequences.

Image based methods

Self-navigation methods obtain the motion information from the MR images itself and are independent of any external sensors or navigators. The direct current (DC) or 0 Hz-signal in the k-space (at the center position of the k-space) contains the full transverse magnetization of the object after RF excitation. Motion leads to changes of the DC signal and, with repeated sampling of the k-space center, a motion signal can be acquired [84]. Typically, k-space center oversampling further increases the motion-sampling rate. Hence, radial read-out techniques are often used. This method has been shown also for fat-suppressed cardiac Cine MRI [85], prospective

motion correction in cardiac imaging [86], and cardiac Cine imaging with utilization of multiple coil elements [87].

Retrospective image-based motion correction can be achieved by optical-flow methods [88]. Signal-intensity variations between following images were used to acquire in-plane motion information. This gives a high spatial resolution and the ability to acquire non-rigid motion but assumes constant pixel brightness in the resting state and is sensitive to through-plane motion.

Image-based methods require no additional hardware but need specialized pulse sequences, which are typically longer compared to standard sequences. Applications in cardiac imaging involve a filter to split respiratory and cardiac motion signal from the k-space DC signal, which results in filter delays.

1.4.5 Motion handling in CMR

Due to the complex motion of the heart, motion handling needs special care in CMR. Besides fast imaging sequences, the image acquisition can be triggered to a specific motion state, but magnetic field effects need to be taken into account. Imaging can also be gated to respiration movement if breath-hold techniques fail.

Triggering and Gating

Periodic physiological motion allows the usage of sequence triggering and gating to reduce image artifacts. Image data can be either collected at the same phase of the motion cycle (triggering) or acquired continuously and then reordered retrospectively (retrospective gating, Fig. 1.12). In CMR, these methods are used to image the heart at a specific motion state (cardiac triggered), capture a set of motion states (Cine imaging) or reduce image artifacts due to breathing (respiratory gating). Triggering and gating requires motion tracking, which is typically performed with pneumatic belts for respiratory gating and electrocardiography (ECG) for heart motion triggering.

Imaging sequences for cardiac motion capture

In CMR, fast sequences are essential to acquire the image data of the continuously moving heart with a sufficient image resolution. Suppression techniques are typically used to minimize the fat signal, which could mask lower-intensity features, or the blood signal for an increased contrast of the myocardic wall (black blood preparation).

A cardiac-specific pulse sequence is Cine imaging, which records multiple heart phases with FGRE sequences during breath-hold and performs a retrospective gating of the data. This represents a movie of the heart motion, and gives information about the cardiac function and wall motion. Cine imaging in combination with a tagging preparation, allows visual investigation of the cardiac motion. The preparation scheme imprints a spin saturation in form of a grid pattern at the beginning of the sequence. During the cardiac cycle the grid lines move according to the heart muscle motion.

With post-processing techniques, the tissue edges can be defined manually or (semi-)automatically. The resulting area of e.g. the left ventricle can be combined

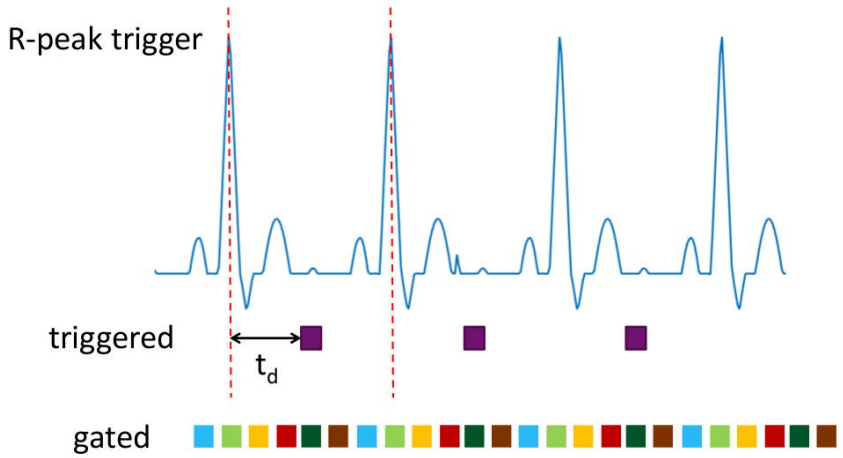

Figure 1.12 – Triggering and gating in cardiac imaging: The trigger point is defined by the R-peak of the ECG. After a defined trigger delay time t_d the image is acquired. In cardiac gating the image acquisition is performed continuously and reordered retrospectively (various cardiac phases are illustrated in different colors)

throughout all cardiac phases, and allow volumetric assessment of the ventricles and atria (Fig. 1.13). In the experiments described in Section 6.2, the volume of the left ventricle was analyzed for the comparison of coil load changes.

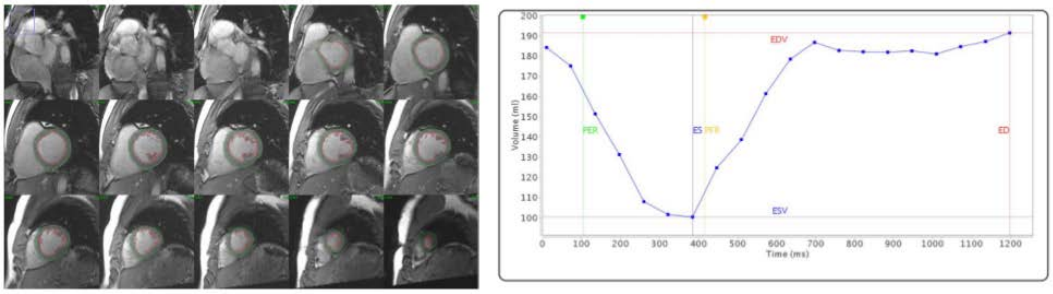

Figure 1.13 – Segmented Cine images and resultant ventricle volume course; left: Short-axis Cine images of different cardiac phases with left ventricle segmentation (green and red lines); right: calculated volume course over the whole cardiac cycle

Electrocardiography

ECG is the classical method to measure the electric activation potential of the heart. The voltages of multiple leads across the potential axes are combined with the ECG signal and the R-peak is utilized as a trigger signal for the pulse sequence. In MRI, the ECG signal, however, is influenced by gradient fields and the magnetohydrodynamic (MHD) effect [89], which is caused by systolic blood flow in the aortic arch. Blood contains ions, which experience a force in a direction perpendicular to the magnetic field while moving inside the blood vessel. The ions accumulate near the vessel walls and cause an electric potential difference. Inside the magnet, a voltage increase in the ECG at the T-wave is observable, when the blood volume transfers from the left ventricle into the aortic arch. An elevated T-wave could be misinter-

preted as the R-peak and triggers the pulse sequence at the wrong time [90]. The MHD effect increases with higher field strength [91] as illustrated in Fig. 1.14 for 7T.

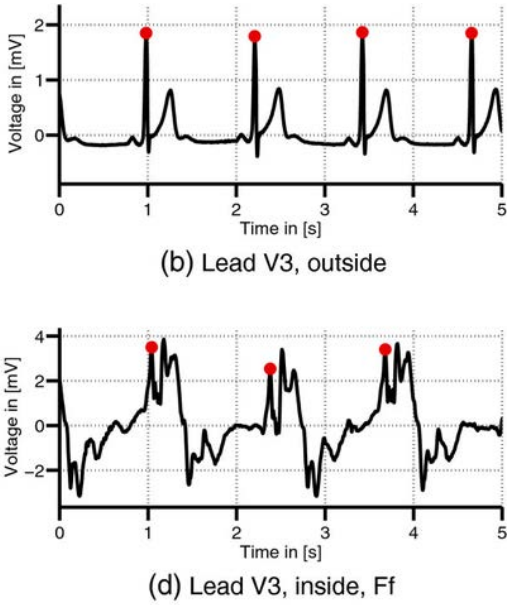

Figure 1.14 – Effect of magnetohydrodynamic effect on ECG; b) ECG signal out-side the magnet, d) same signal inside a 7T magnet, Red dots mark the R-peak. Figure in [92], copyright information see List of Figures

It is generally recommended to use an orthogonal vector lead ECG configuration that reduces the sensibility against the MHD effect. Various filter techniques were developed for more reliable R-peak detection [93, 94, 92, 95] or to correct for gradient-induced voltage [96]. Alternatively pulseplethysmography (PPG) is available on MRI systems and registers the pulse waveform in the finger. This method is not influenced by the MHD effect, however it is less precise and due to the peak shift caused by the pulse transit time, trigger delays need to be adjusted accordingly.

As mentioned before, ECG represents the electric activation of the heart but does not directly deliver a mechanical motion. Due to the mentioned distortion effects, triggering is preferred over a gating approach. In order to acquire images at the correct cardiac phase (e.g. end-diastolic), trigger delay times need to be defined as a function of the heart rate [97] or manually from Cine images. The theoretical model approach is based on the data of 211 healthy subjects and gives an estimate of the end-diastolic time according to the heart rate. Since the heart rate typically varies during the exam, this could lead to inaccuracy in recorded cardiac phases. The visual readout of trigger delays from Cine images is reported to be error-prone due to different approaches for cardiac phase selection [98]. This raises the need for motion tracking techniques which represents the physiologic action of the heart to improve the triggering at the correct motion phase. Some of the previous mentioned methods provide such information. The ability of the imaging coil for physiologic heart motion capture is investigated in this work.

1.5 Summary

Magnetic resonance imaging results from the excitation and relaxation of hydrogen nuclei in a magnetic field. The long examination time, depending on the relaxation times and the sampling scheme, makes MRI sensitive to position changes of the patient during the scan. Distortions like image blurring or ghosting artifacts are the consequence. This is a major disadvantage especially in cardiac MRI, due to the constantly moving heart and respiration.

A variety of solutions to this problem are available nowadays. Fast imaging techniques, immobilization or training reduce the motion occurrence. Prospective and retrospective correction methods synchronize the imaging to the motion and correct images according to motion information respectively. This requires some knowledge about the motion direction and amplitude, which is provided by various motion-tracking techniques. Image-based methods detect the motion change in the image or k-space directly. However, these methods are not available for every pulse sequence and, hence, are limited in use. External sensors on the patient or in close proximity detect the motion independently from the imaging sequence. RF and magnetic field compatibility is a prerequisite for such sensors. The advantage and disadvantages of the various methods are summarized in Table 1.5.

One technique, which has been investigated only superficially until now, detects impedance variations of the imaging coil itself. No extra sensors are required and the motion measurement is pulse sequence-independent. In addition, it could increase patient comfort and preparation workflow in clinical practice. The current research presented here focuses on the motion detection with such imaging coils addressing especially cardiac and respiratory motion.

The following chapter will cover the RF technology in MRI and imaging coil design, and explain the effect of moving tissue on the coil.

Method	Advantages	Limitations
Electro-mechanical sensors (accelerometer, pneumatic belt)	• plain setup • detects mechanical motion • absolute motion measurement [+]	• detects only surface motion • subject to drift or saturation • sensitive to positioning
Acoustic sensors (microphone, ultrasound)	• detects mechanical motion intracorporeal	• sensitive to gradient noise • sensitive to positioning
Optical sensors (camera)	• 2D/3D motion information • high spatial and temporal resolution • detects surface and physiologic motion • localized, absolute quantification	• direct sight necessary • marker fixation critical • sensitive to light scatter • local measurement
NMR probes	• uses gradient field • does not interfere with imaging	• detects surface motion only • complex setup
Imaging coils (incl. mounted pick-up coils)	• motion detection during scan • detects mechanical motion intracorporeal[#] • no hardware in magnet bore[#]	• sensitive to positioning[#] • volume motion only (no localization)

Tables continuous on next page

Method	advantages	limitations
ECG	• elaborate cardiac motion detection method • precise trigger	• sensitive to positioning • signal corruption by MHD effect
UWB	• high temporal and spatial resolutions • penetration into object • low power	• requires comprehensive measurement system • setup reduces tunnel diameter
Navigators	• no extra hardware in magnet bore • penetration into object	• not available for every sequence • sensitive to positioning
Image based	• no extra hardware in magnet bore	• detects in-plane motion only • not available for every sequence

Table 2 – Summary of advantages and limitations of various motion detection methods; $^{+}$ true for accelerometer only; $^{\#}$ true for surface coils only

2

Introduction to radio frequency technology in MRI

As explained in the previous chapter, RF technology is an essential part of MRI imaging. The excitation of the spins and relaxation signal acquisition relies on the nuclear induction described by Bloch [6] (see also Section 1.1.2). Transmission and reception units for such signals - so-called coils - have to be designed carefully to provide homogeneous excitation fields and to detect the small relaxation signal with the highest possible SNR. The physical principle behind imaging coils and various coil designs for MRI imaging are introduced in Section 2.1.

For building and analyzing RF components or circuits, computer model simulations and various measurement techniques are available today. An introduction of electromagnetic simulations in given in Section 2.4. In this thesis, EM simulation were performed to analyze the tissue dependent coil impedance.

Two measurement techniques used in the experiments, namely S-parameter measurements and I-V method for impedance evaluation, are discussed in Section 2.2.

The main topic of this work covers the influence of conductive material (e.g. also the human body) on the coil's performance. Section 2.3 explains the electromagnetic properties of biological tissue and its applications in medical diagnostics.

2.1 RF coil design for MRI

RF coils are an essential part of a MRI system. They serve the purpose of creating the homogeneous magnetic field B_1 perpendicular to the main B_0 field in the transmit case and acquiring the signal emitted from the nuclei with a high SNR. MRI RF coils are electrical resonating circuits, tuned to the Larmor frequency of the nucleus of interest (in MRI typically the ^{1}H nucleus). The fundamentals of electrical resonating circuits are described in Section 2.1.1. The coil design is critical for the image quality. It has to address, for the narrow bandwidth of the Larmor frequency, the low signal from the nuclei as well as losses due to coupling effects with the patient. Section 2.1.2 captures the tuning of the coil and the matching to the MRI system. Coil sensitivity and losses are further explained in Section 2.1.3.2.

Receiving a high-resolution signal, e.g. of the brain, involves different requirements than generating a homogeneous magnetic field throughout the whole body. Hence, there exist several coil designs for different purposes and imaging areas. These are introduced in Section 2.1.4.

2.1.1 The RLC circuit

A rotating magnetic field induces a voltage in a wire loop perpendicular to the magnetic field (Eq. 1.10) The pure induced signal of the electromagnetic force (emf) in a loop coil, however, is too low to measure the NMR signal reliably. Modifying the conductive loop to a resonant circuit with a quality factor Q, multiplies the emf signal by this factor. Electrical resonating circuits are built from inductance (L), capacitance (C), and resistance (R). Physically, coils are constructed from conductive wire with capacitors. The type of wire and the coil's design define its L and R, while the resonant behavior and quality are adjusted by C.

The complex impedance Z of the components is frequency-dependent (Table 3). At RF, the resistance is affected by the skin effect. Due to this effect, the current does not distribute through the whole conductor, but is concentrated on the surface of the conductor. This effect leads to a higher resistance than the DC-resistance value R_0 with increasing frequency. The impedance of the inductance and capacitance contain only an imaginary part linearly aligned with the frequency. Combining the components results in a resonant circuit at a defined frequency.

resistance R	**inductance L**	**capacitance C**
$R \approx R_0\sqrt{f}$	$Z_L = jX_L$	$Z_C = -jX_C$
	$X_L = 2\pi fL$	$X_C = \frac{1}{2\pi fC}$

Table 3 – Frequency behavior of the impedance of resistor, inductance and capacitor. R_0 is the resistance at DC, X_L and X_C the inductive and capacitve reactances

RLC circuits can be combined in parallel or series configurations or can be a mixture of both. The resonant loop coil can be described with a parallel LC circuit, whereas R is in series with L representing the losses in the coil (Fig. 2.1b). The complex impedance of a the given RLC circuit Z_R is the sum of individual component impedances

$$\frac{1}{Z_R} = \frac{1}{R + Z_L} + \frac{1}{Z_C} = \frac{1}{R + jL\omega} + jC\omega \tag{2.1}$$

with $\omega = 2\pi f$ the circular frequency. Mispelter et.al. [99] give Z_R as the algebraic solution for parallel circuits

$$Z_R = \frac{RX_C^2}{R^2 + (X_L - X_C)^2} - jX_C\frac{R^2 + X_L(X_L - X_C)}{R^2 + (X_L - X_C)^2} \tag{2.2}$$

Resonance occurs when the imaginary part approaches zero:

$$R^2 + X_L(X_L - X_C) = 0 \tag{2.3}$$

which results to

$$LC\omega^2 = 1 - \frac{R^2C}{2L} \tag{2.4}$$

Since R is typically very low it could be neglected and a good approximation for the resonant frequency ω_0 can be made

$$\omega_0 = \frac{1}{\sqrt{LC}} \tag{2.5}$$

RLC circuits with a defined resonant frequency have an dedicated impedance according to the circuit components. Connecting the imaging coil to the MRI system, modifications to the RLC circuit are necessary to achieve the correct impedance and frequency of the system. In the next Section 2.1.2 this will be further adressed.

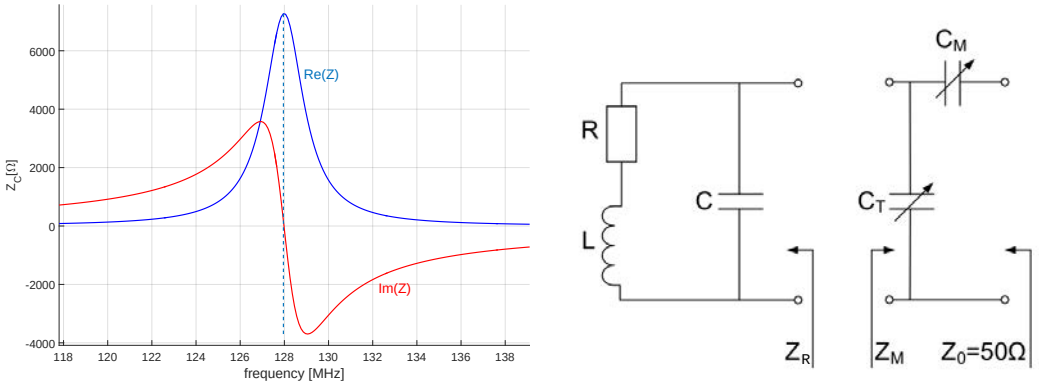

(a) Frequency response of RLC circuit

(b) Schematic of coil and tune-match unit

Figure 2.1 – a) Real (blue) and imaginary (red) part of frequency dependent impedance of coil circuit. Resonance frequency is at 128MHz (dashed line) with R=2Ω, L=150nH, C=10pF. b) Schematic of coil circuit (left) and tuning and matching network (right). The aim of this network is to adjust the impedance of the coil to the system impedance of $Z_0 = 50\Omega$

2.1.2 Tuning and Matching

For the connection of RF circuits, coaxial cables are typically used. However, power reflections could occur if the impedance of the components and cables is not matched. Therefore, various conventions for the impedance of cables exist in RF technology. In MRI, RF cables with a characteristic impedance of $Z_0 = 50\ \Omega$ are used. This requires an accordant adaption of the RF components to this impedance.

In MRI coils, a tuning and matching network is added to the coil to adjust the coil impedance Z_C to the system impedance $Z_0 = 50+j0\ \Omega$ (Fig. 2.1b). The tuning capacitor C_T is connected in parallel to the capacitance of the coil. This shifts the resonance frequency so that the real part of the impedance is 50 Ω at the desired frequency. Using Eq. 2.2, X_C would change to $X_C=1/(\omega(C+C_T))$.

The matching capacitor C_M in series with the coil circuit reduces the imaginary impedance of Z_R by $Z_{CM}=-1/(j\omega C_M)$. Z_{CM} has to compensate for the residual imaginary impedance, so that, with C_T and C_M applied, the coils' impedance $Z_R = Z_0 = 50+j0\Omega$.

Besides the capacitive coupling network, a solution with inductive coupling is possible as well. However, this method was not used in the present work and the interested reader is referred to [99].

2.1.3 Coil Sensitivity, Q-value and losses

An important parameter defining the image quality and coil performance is the SNR. It is a measure of the signal voltage in comparison to the voltage caused by losses given by SNR = U_S/U_N. The signal voltage U_S is described in Equation 1.26. The thermal noise voltage U_N is defined as

$$U_N = \sqrt{4k_B T R \Delta\vartheta} \tag{2.6}$$

where k_B is the Boltzmann constant, T the temperature, $\Delta\vartheta$ the acquisition bandwidth and R the noise resistance. The latter is a combination of various loss effects, explained in Section 2.1.3.1.

With U_S and U_N, the SNR results in

$$SNR = \frac{-j\omega_0 \vec{B_1} \vec{M_{xy}} V}{\sqrt{4k_B T R \Delta\vartheta}}. \tag{2.7}$$

It can be observed that the SNR also depends on scan parameters resulting in M_{xy}. This is diffcult to simulate in lab setup however. To analyze the intrinsic SNR of coils on the lab bench, the analysis of the quality factor Q is used for quantification of the coils quality, which explained in detail in Section 2.1.3.2. The influence of moving structures like organs or blood flow on the coil loading is further addressed in Section 2.1.3.3.

2.1.3.1 Loss factors on RF coils

Depending on the coil loading or the coil design, losses can be caused by different sources which can be split into resistive, radiation, inductive and dielectric losses

Resistive Losses

Losses in an empty or not loaded solenoid coil were described by Hoult and Lautbur [100] as

$$R_C \cong \frac{3\zeta n^2 a}{l\sigma\delta} \tag{2.8}$$

with ζ as the proximity factor, n the number of windings, a the coil radius, l the coil length, σ the conductor conductivity, and δ the skin depth. The losses are due to the geometric dimensions (n, a and l), the material, and the influence of the skin effect. The resistive losses are increased by coupling between coil elements (e.g. solenoid windings), described by the proximity effect. An optimized design, high-quality components, and careful construction of the coil can minimize the resistive losses of a coil. In [100], the usage of superconducting material at low temperatures is suggested to reduce such losses, which found some application in research.

Radiation losses

In the transmit case, the coil also emits energy as electromagnetic waves in the far field, while only the energy of the near field affects the nuclei. These radiation losses can be minimized by RF shielding, which is typically applied in MRI systems. Segmenting the coil wire in sections to 1/10th of the wavelength λ, these losses can be further reduced.

Inductive losses

On placing the coil on a conductive object or tissue, additional losses occur. The oscillating B_1 field generates eddy currents in the conductive material close to the coil which dissipates energy. This energy loss is characterized as inductive losses and expressed in [100] for a conductive sphere with the radius b as

$$R_M = \frac{\pi \omega_0^2 \mu_0^2 n^2 b^5 \sigma}{30(a^2 + g^2)} \tag{2.9}$$

Besides of the geometry of the coil (radius a, length g, number of turns n) and the frequency ω_0, the conductivity σ of the sample is affecting the inductive losses. However, the magnetic coupling of the coil and the sample is a prerequisite for MRI imaging and these losses cannot be avoided.

Dielectric losses

Dielectric losses are caused by the electric fields of the RF coil generating dissipative RF currents in the conductive tissue. These currents cause capacitive coupling in the RF coil and, thus, generate noise. A dielectric loss can be expressed as resistance R_D in high fields with

$$R_D \cong \frac{\omega_0^2 L^2 C_C^2}{R_S (C_C + C_S)^2} \tag{2.10}$$

with R_S and C_S in parallel as the equivalent circuit of the sample, and C_C as the stray capacitance [101]. Dielectric losses can be minimized by distributing the coil capacitors throughout the coil diameter [99] and choosing a proper coil dimension in accordance of the region of interest (ROI) [102]. However for the body birdcage resonator this cannot be achieved and dielectric losses highly depend on the body radius [103] and dominate over other loss factors.

A different approach for loading analysis was presented by van Heteren et.al. [104] (Fig. 2.2). The coil and the sample are described in a combined equivalent electrical circuit. This approach is suitable for analytical investigation of the coil loading as it addresses also radiation losses. In Q-ratio measurements these losses are neglected since the coil design (shielding, capacitor splitting) is supposed to compensate for it. The equivalent circuit considers magnetic field coupling by introducing a dissipative inductance L_m and resistance R_m coupled to the coil with the coupling factor K. Capacitive coupling is represented by an capacitor C_1 and the electric field losses are modelled by a parallel circuit of R_e and C_2. R_m and R_e are related to the samples conductivity and coil geometry by correction factors. The sample impedance can be summarized to

$$Z_S(\omega) = K Z_m(\omega) + Z_e(\omega) \tag{2.11}$$

with Z_m the impedance of the inductive losses and Z_e the impedance of the radiation and dielectric losses described by

$$Z_m(\omega) = R_m(\omega) + j\omega L_m \tag{2.12}$$

and

$$Z_e(\omega) = \frac{1}{j\omega C_1} + \frac{R_e}{1 + R_e j\omega C_2} \tag{2.13}$$

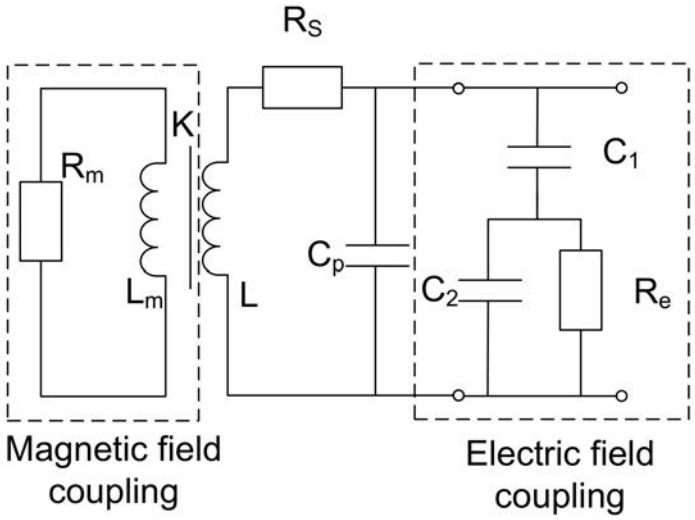

Figure 2.2 – Equivalent circuit for sample losses [104]; Magnetic field effects are represented by R_m, L_m and K, losses caused by electric field interactions are represented by R_e, C_1 and C_2

2.1.3.2 Q-value

The resistance R of a coil represents its losses. To quantify the effectiveness of a coil, a quality factor Q was introduced as the ratio of the magnetic energy stored in the inductor (X_L) to the energy consumed by the losses (R)

$$Q = \frac{X_L}{R} = \frac{\omega L}{R} \tag{2.14}$$

The Q value of a loaded coil Q_l reflect the sum of all occurring losses between the coil and the sample, whereas the Q value in the unloaded state Q_u contains only the losses from the coil itself:

$$Q_u = \frac{\omega L}{R_C} \tag{2.15}$$

and

$$Q_l = \frac{\omega L}{R_C + R_M + R_D}. \tag{2.16}$$

The Q-ratio Q_u/Q_l gives an indication on the dominating loss mechanisms and the coil sensitivity.

$$\frac{Q_u}{Q_l} = \frac{R_C + R_M + R_D}{R_C} \tag{2.17}$$

A sample loss domination ($Q_u >> Q_l$) is aimed for high sensitivity and SNR. The intrinsic SNR of a coil relates to the Q-ratio by

$$SNR_{coil} \cong \frac{1}{\sqrt{\frac{Q_u}{Q_l}}} \tag{2.18}$$

2.1.3.3 Influence of motion to sample losses

Movement of conducting structure in close proximity to the coil or inside a volume coil causes variations of losses in the coil. Bulk body motion inside a volume coil causes changes in the capacitive coupling caused by distance change between the body and the coil. Similarly organ motion in the sensitivity field of a loop coil is influencing the capacitive coupling.

Furthermore tissue changes its conductivity and permittivity which is typically related to motion. The dielectric properties of lung tissue changes by a factor of 2 between inspiration and expiration [105]. This is primarily caused by the air content of the lung tissue and the coherent distance and size of alveole [106]. In the heart region, loss changes are a combination of blood volume variations in the ventricles and the heart muscle motion. A volume between 68 and 144 ml of blood is ejected from each ventricle on every heart beat (chapter 1.3.2), which changes the local dielectric properties. As shown in chapter 6.1, blood volume changes in peripheral arteries causing also impedance variations whereas the effect is reduced due to the smaller volume.

2.1.4 Coil types for MRI

RF coil design depends on the application and the region of interest of the human anatomy. RF coils serve two purposes - to generate a RF magnetic B_1 field and to receive the NMR signal. This functionality can be performed by one and the same coil via a T/R switch or by two separate coils. In clinical imaging, the body coil is often used for the RF excitation, while surface coils receive the echo signal in the ROI.

RF coils are classified into volume coils and surface coils and are explained in the following.

2.1.4.1 Volume coils

Volume coils are designed to produce a homogeneous B_1 field in the whole object inside the coil. Hence these type of coils are often used for spin excitation in MRI imaging. Different designs exist, which produce either a linear magnetic field in parallel to their design axis (solenoid coil, Helmholtz coil) or a circular magnetic field perpendicular to the design axis (saddle coil, birdcage coil, transmission line coil). A solenoid coil is built from cylindrical wounded wire or conductive sheet and is used in NMR experiments or multi-nuclear spectroscopy. With known samples inside the solenoid, such NMR probe can be used for gradient field monitoring [107] or motion detection [69]. The circular magnetic fields are generated by saddle-shaped and birdcage coils. Their specific design allows the positioning inline with the magnetic field and simplifies the access in horizontal cylindrical magnets which are used in MRI. The birdcage coil design is the classical transmit and receive coil in a MRI system and was investigated for physiological impedance fluctuations in this work. Its design explained in more detail in the following.

Birdcage coil

Hayes et.al. [108] developed the birdcage coil, named due to its design (Fig. 2.3a). It produces a transverse circularly polarized magnetic field by longitudinal conductors equally spaced - also called rungs - connected with end-rings on each end of the cylindrical structure. For current distribution evaluation, one can split up the cylinder and analyze the ladder network of the resonator (Fig. 2.3b). In each element

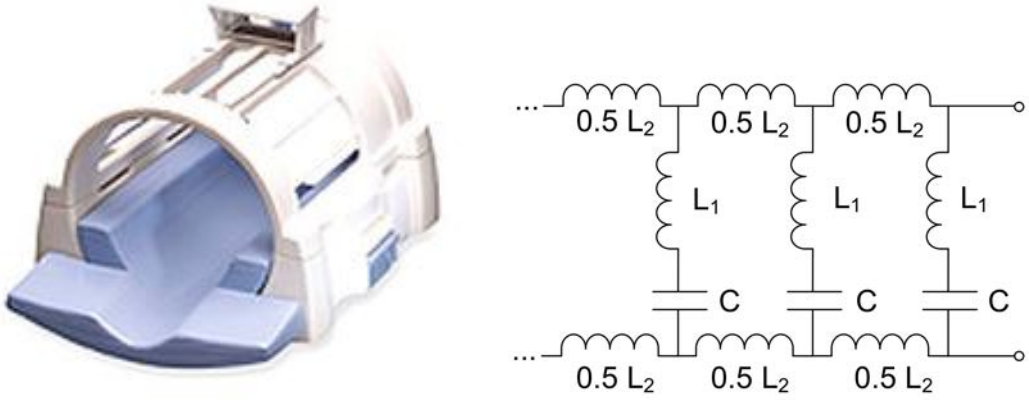

(a) Clinical birdcage head coil (b) Schematic of birdcage network

Figure 2.3 – a) Clinical birdcage headcoil, b) Ladder network of a low-pass birdcage coil

a current with a phase shift defined by its relative angle position of the leg occurs. This causes multiple resonance frequencies called modes or harmonics, which can be calculated for the given circuit given as

$$\omega = \frac{2}{\sqrt{L_1 C}} \sin \frac{\pi n}{N} \tag{2.19}$$

with n = [1, N/2] and N the number of rungs. This ladder network shows a low-pass birdcage coil. The frequency for n=1 is the most prominent in this case which produces a homogeneous magnetic field. Birdcage coils can be designed in low-pass-, high-pass- or band-pass configuration, which affects the distribution of the modes. Fig. 2.4 shows the frequency spectrum of a 3T birdcage body coil in a hybrid design. The Larmor frequency at 128 MHz is clearly determinable by the strong reflection factor, whereas the other resonant frequencies show lower reflection factors and, hence, less sensitivity. The harmonic modes were further investigated in this work as a motion signal carrier (Section 5.2). The birdcage coil design allows a quadrature drive due to its design. Introducing power spatially oriented by 90° and with a phase difference also of 90° generates a doubled circularly polarized field. This reduces the transmit power by a factor of $\sqrt{2}$ and doubles the receive signal voltage, while the receive noise increases by $\sqrt{2}$ only.

2.1.4.2 Surface coils

The major prerequisite for MRI imaging is the homogeneous excitation of the nuclei in the volume and a high SNR in the received signal. The first requirement is achieved by volume coils, but the receive SNR is not optimal. The signal of a

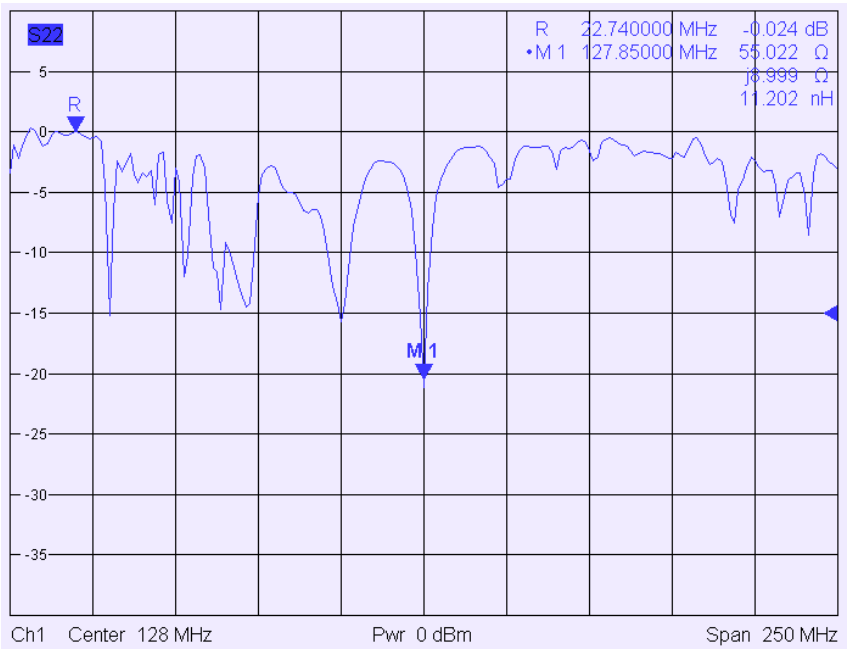

Figure 2.4 – Harmonic frequencies of 3T birdcage body coil; M = Marker at 128MHz Larmor frequency

limited ROI is accompanied by the noise contribution of the whole volume [12, 100]. A surface coil positioned directly on the patient, limits the noise influence to the ROI. However, due to its design the magnetic field decreases rapidly with the increasing distance and is largest at its surface (hence its name). Due to that reason, in clinical imaging surface coils are used as receive-only coils with the usage of volume coils for spin excitation. Surface coils can be designed as one-channel loop coils (Fig. 2.5a) or multi-channel phased array coils for various body regions (Fig. 2.5b and 2.5c).

(a) Single loop 31P coil

(b) 36-channel peripher vascular coil

(c) 30-channel head neck coil

Figure 2.5 – a) Single loop 31P coil, b) 36-channel peripher vascular coil, c) 30-channel head neck coil

Single Loop Coils

Single loop coils is a basic coil design introduced in MRI by Ackerman et.al [109]. It consists of a single loop balanced with a capacitance to the resonance frequency and produces a heterogeneous magnetic field along its axis. In a close approximation

the sensitivity decreases to 35% at the distance of its radius [102]. A compromise between SNR and ROI has to be met while designing the coil.

Due to its inhomogeneous magnetic field, surface coils are typically used as receive-only coils, while the birdcage body coil provides the excitation field. In this case the loop coil needs to be decoupled during the RF excitation to prevent coil damage and to ensure patient safety. Decoupling is performed by fast switching, low RF resistive PIN diodes, which connect an additional inductance to the coil during the transmit RF pulse, causing a shift of the resonant frequency. The switching can be performed actively with DC voltage applied by the MR system, or passively by current in the loop wire.

Coil arrays

The demand of high SNR over a large ROI for applications as spine imaging, lead to the combination of multiple single loop coils to coil arrays or phased arrays [110]. The single loop elements can be arranged one-, two or three-dimensional. One major objective in designing such coils is the minimization of the mutual interference between two neighbored coil elements by inductive coupling. Solutions can be found in overlapping coil elements [110], capacitive decoupling [111] or preamplifier decoupling [110]. In modern MRI imaging, phased array coils are widely used not only for the high SNR but also for their ability to reduce scan time with parallel imaging technique [42]. A 4-channel cardiac coil was utilized in this work to register motion at different body parts in real-time.

2.2 RF measurement techniques

The measurement of electric properties of a radio frequency system is different from measurements on a DC system by the frequency dependency of electric parts and the resulting effects (e.g. phase shifts, reflection). In this study the impedance variations of coil elements were the subject to measure. Various impedance measurement methods can be found in [112], namely bridge method, resonant method, I-V method and network analysis method. In the following the two techniques used in the experiments of this work are explained more in detail. The network analysis method or scatter parameter measurement is typically used to understand frequency behavior of electric circuits (Section 2.2.1). A modified version of the I-V method can be found in the measurement of coupled power (Section 2.2.2).

2.2.1 Scatter parameters for characterization of RF circuits

Scatter parameters (S-parameters) are measures of the frequency-dependent properties of electrical components or systems. The measurement is performed by vector network analyzers (VNA) with one to four ports. With subsequent switching matrices, the number of measurement ports can be increased. The complex value S_{nm} contains the magnitude and phase information about the transmission and reflection behaviors at connection points or ports, where n and m indicate the signal entry and exit ports respectively. Typical RF circuits are two-port systems with input and output ports, like filters, attenuators, amplifiers or mixers. Imaging coils can be one-port systems (single loop coil, solenoids), two-port systems (birdcage coil in quadrature mode) or multi-port systems with more than two ports (coil arrays). Scatter parameters describe the ratio of the normalized incident and reflected power waves a_n and b_n at the ports n. For a system with N ports, N^2 scattter parameter exist (Fig. 2.6). On a one-port system the only S-parameter S_{11} is related to the reflection factor $\Gamma(\omega)$.

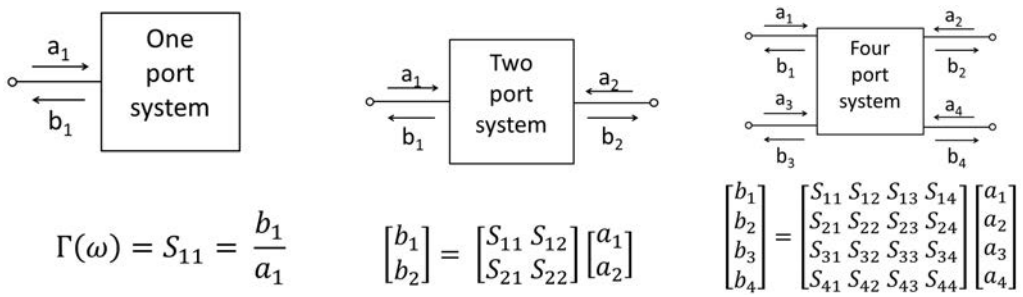

(a) One port system (b) Two port system (c) Four port system

Figure 2.6 – S-parameters of one-, two- and four-port systems

The incident and reflected waves hold the frequency dependent voltages U_C and currents I_C at the ports

$$a(\omega) = \frac{U_C(\omega) + Z_0 I_C(\omega)}{2\sqrt{Z_0}} \tag{2.20}$$

and

$$b(\omega) = \frac{U_C(\omega) - Z_0 I_C(\omega)}{2\sqrt{Z_0}} \tag{2.21}$$

As described before, $Z_0 = 50 + j0\Omega$ is the reference impedance. The frequency dependent complex impedance Z_R can be calculated from

$$Z_R(\omega) = \frac{U_C(\omega)}{I_C(\omega)} \tag{2.22}$$

The reflection factor $\Gamma(\omega)$ is described by

$$\Gamma(\omega) = \frac{b(\omega)}{a(\omega)} = \frac{Z_R(\omega) - Z_0}{Z_R(\omega) + Z_0} \tag{2.23}$$

In the ideal case of full power transmission at resonant frequency ω_0 the coil impedance is matched to the reference impedance and $\Gamma(\omega_0)$ =0. The magnitude of the S_{11} coefficient is at its minimum in this case. As the resonance capability of a electrical circuit depends on the influence of losses, the bandwidth $\Delta\omega$ at half of the S_{11} magnitude (3 dB bandwidth) indicates the effectiveness of the circuit (Fig. 2.7. Hence the quality factor Q can be directly measured from the S_{11} coefficient by

$$Q = \frac{\omega_0}{\Delta\omega} \tag{2.24}$$

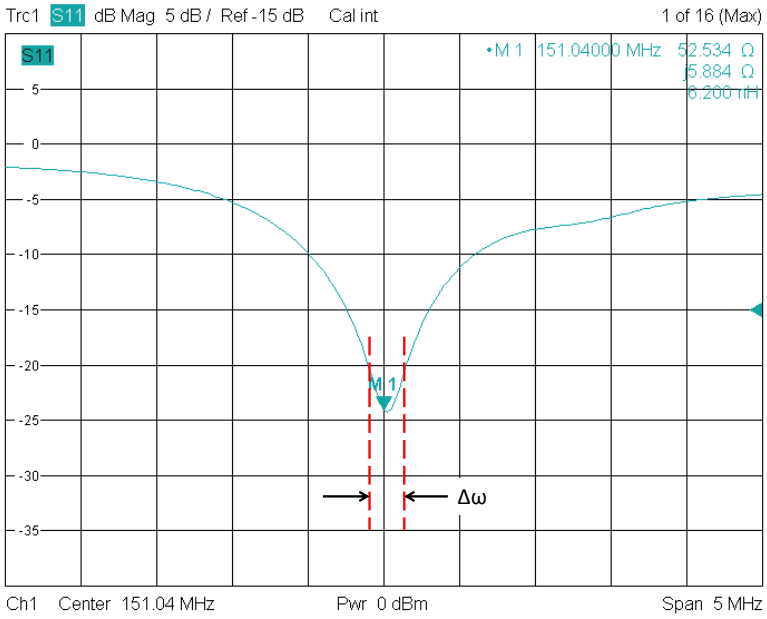

Figure 2.7 – Magnitude of S11 coefficient of a coil measured with a VNA; Marker M1 indicates the resonant frequency ω_0 and $\Delta\omega$ the 3 dB bandwidth. The ratio of both values is the quality factor Q (Eq. 2.24)

Considering motion induced losses as described in chapter 2.1.3.3, $\Gamma(\omega)$ of a coil is influenced by a variable load impedance

$$\Delta Z_L(\omega) = Z_R(\omega) + \Delta Z_S(\omega) \tag{2.25}$$

and results to a varying reflection factor

$$\Delta\Gamma(\omega) = \frac{\Delta Z_L(\omega) - Z_0}{\Delta Z_L(\omega) + Z_0} \tag{2.26}$$

whereas $Z_C(\omega)$ is the complex impedance of the coil and $\Delta Z_S(\omega)$ is the varying sample impedance.

2.2.2 Impedance determination by power measurement

VNAs are powerful measurement devices, however also expensive and not always available. Alternative methods to determine the impedance of a RF circuit can be found in bridge methods or I-V methods [112]. A modified RF I-V method is the comparison of the forward and reflected power. For the reflection factor applies also

$$|\Gamma(\omega)|^2 = \frac{P_{FWD}}{P_{REF}} \tag{2.27}$$

with P_{FWD} the incident power and P_{REF} the reflected power. This indicates that the absolute varying impedance relates to the power ratio. A measurement component which allows the measurement of the incident and reflected power separately on the same cable can be found in directional couplers. A coupler typically consist of two TEM-lines in parallel and in short distance to each other. While one line carries the power of the circuit to be measured, the second line couples to the main line and holds incident and reflected power at lower power rate (Fig. 2.8). The coupling factor κ is defined by the distance of the two lines. Directional couplers were used in the experiments described in Sections 5.1, 5.2 and 6.1. The forward coupled port was terminated with 50 Ω, while a power meter was connected to the reflected coupled port.

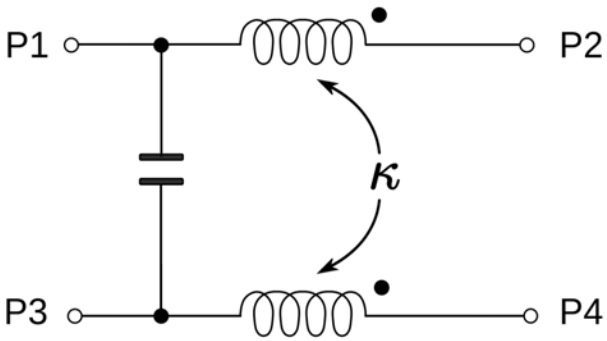

Figure 2.8 – Schematic of a directional coupler: The power of the main line between P1 and P2 is coupled according to the coupling factor κ to a secondary line providing a attenuated forward (P3) and reflected (P4) power levels

A method utilizing the magnitude and phase information is reported in [113]. Both coupled power levels are combined in a RF mixer. The resulting signal holds the motion data and preserving the phase of the baseband signal as an additional motion information.

2.3 Electromagnetic properties of biological tissue

Biological tissue can be considered as a dielectric material. In MRI static and varying magnetic fields and RF fields are applied to the human body and interact with the tissue according to its electromagnetic properties [114].

The dielectric properties of a material are described by the complex relative permittivity

$$\epsilon = \epsilon' + j\epsilon'' \tag{2.28}$$

with $\epsilon' = \epsilon_r$ the relative permittivity of the tissue and

$$\epsilon'' = \frac{\sigma}{\epsilon_0 \omega} \tag{2.29}$$

with ϵ_0 the permittivity in free space, σ the conductivity of the tissue and ω the angular frequency. The relative permittivity and conductivity are frequency dependent but not linear (Fig. 2.9). The interaction mechanisms between the biological

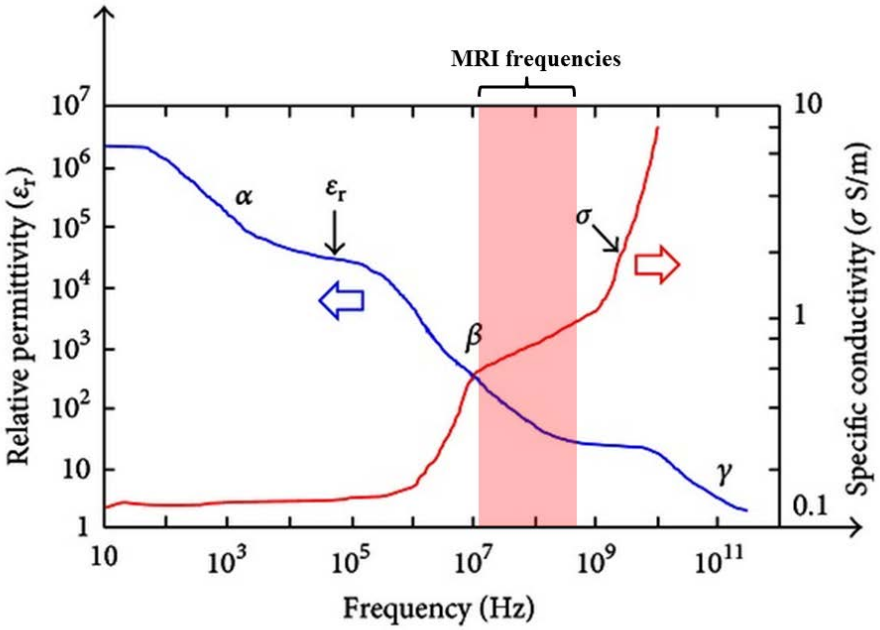

Figure 2.9 – Frequency dependent permittivity and conductivity of tissue. Red are indicates the frequency range in MRI

tissue and the electromagnetic waves results in α-, β- and γ-dispersions [115]. In the frequency range of MRI (10^7-10^8 Hz), the relative permittivity and conductivity change linearly. Biological effects of the radiofrequency waves are primarily caused by the magnetic field component [114]. This is due to quasi-static approximation for the near-field region with the distance between source and sample $L \leq \lambda$. In the near field region either a primarily electric or magnetic field is dominant. The main effect of the field on the tissue in the MRI-frequency range is thermal heating, due to the direct energy absorption. For patient safety it is relevant to understand these

effects, arrange safety limits (e.g. specific absorbtion rate, SAR) and address these limits in MRI coil design.

	64MHz		128MHz	
Tissue type	relative permittivity	elec. conductivity [S/m]	relative permittivity	elec. conductivity [S/m]
Lung inflated	37.1	0.289	29.5	0.316
Lung deflated	75.3	0.531	63.7	0.576
Heart muscle	107	0.678	84.3	0.766
Blood	86.4	1.21	73.2	1.25

Table 4 – Permittivity and conductivity values for heart and lung at 64MHz and 128 MHz out of [105]

Dielectric values are not only dependent on the tissue type or to a specific organ, but vary with physiological events related to organ motion. As shown in Table 4, the filling of the lung changes its permittivity by a factor of 2 and its conductivity by a factor of 1.8. Similarly the dielectric values of the heart vary between the end-systolic (heart muscle dominated) and end-diastolic (blood volume dominated) phase by a factor of 0.8 and 1.7 respectively. Due to its content of ions, blood has a considerably higher conductivity, compared to muscle and lung tissue. These observations vary only slightly between the Larmor frequencies for magnetic field strength of 1.5 T and 3 T.

The measurement of electromagnetic properties found interest for medical diagnosis in the past. Impedance cardiography is reported as a non-invasive cardiac output measurement technique [116]. A combination of multiple electrodes is used for electric impedance tomography to determine spatial lung function information and pathology [117]. Cardiokymography is a method based on the reflection of an RF probe for myocardial wall motion assessment. [118].

2.4 Electromagnetic simulation for MRI systems

Electromagnetic (EM) simulations are an essential part of MRI coil construction. The complex electromagnetic fields can be analyzed with high spatial resolution and coil design can be optimized without expensive hardware modifications. Furthermore, the effects on conductive samples - from simplified phantoms like spheres or cylinders to sophisticated heterogeneous human models can be calculated. In MRI, SAR level and temperature distributions are of special interest [119], since these are important safety parameters, especially on patients with implants [120] or on multi-channel transmission systems [121].

For the analysis of the magnetic field interaction between the coil and the subject, the boundary-value problem given by the Maxwell equations needs to be solve [122]. This includes the RF coil itself, the subject and the neighbored formations with different electromagnetic properties. Various approaches exist to model the electromagnetic fields precisely in time or frequency domain. The most popular are Finite-Difference Time-Domain method (FDTD), Finite Element Method (FEM) and Method Of Moments (MoM).

With the FDTD method the entire simulation domain is discretized by rectangular cells. The cell size depends on the wavelength of the desired frequency. The resolution of the time axis also depends on the desired frequency and is linked to the model resolution. Magnetic field components of a specific time step are calculated from the surrounding electric field components by using discretized Maxwell's equations. In FDTD it is relatively easy generate models, as voxel-based data of conductors or human models are used. Round-shaped objects have to be modeled by so-called staircase approximations, which limits the geometric modeling (e.g. for thin structures).

The FEM uses tetrahedral shapes which allow arbitrary shaped objects. For each cell, test functions are defined which are inserted in the partial differential equations, which result in starting, border and transfer conditions. In both methods, FDTD and FEM the entire volume is discretized and included in the calculations. In order to simulate border conditions correctly, absorption layers or perfectly matched layers (PML) need to be introduced at the outer boundaries to avoid artificial wave reflections which result in simulation errors.

Another efficient approach for numerical electromagnetic simulation can be found in the Method Of Moments (MoM). Here integral equations of surface currents on conducting surfaces are calculated in the frequency domain. Since the surrounding of the object is not considered, border attenuation (e.g. PML) is not needed with MoM. This reduces the amount of unknowns in the equation, however has no effect in computation time. This is due to the fully populated coefficient matrix, in contrast to symmetric and sparse matrices in FEM.

Each method is suited for different applications. For EM simulations on MRI RF coils, the method should allow the import of (partial) human models. FTDT is most suitable for that, but with some adaptions these models can also be included in other methods. To investigate field effects in human tissue, a variety of human models are available in different sizes, shapes, tissue types and spatial resolution. Figure 2.10 shows the Virtual Population provided by the IT'IS foundation.

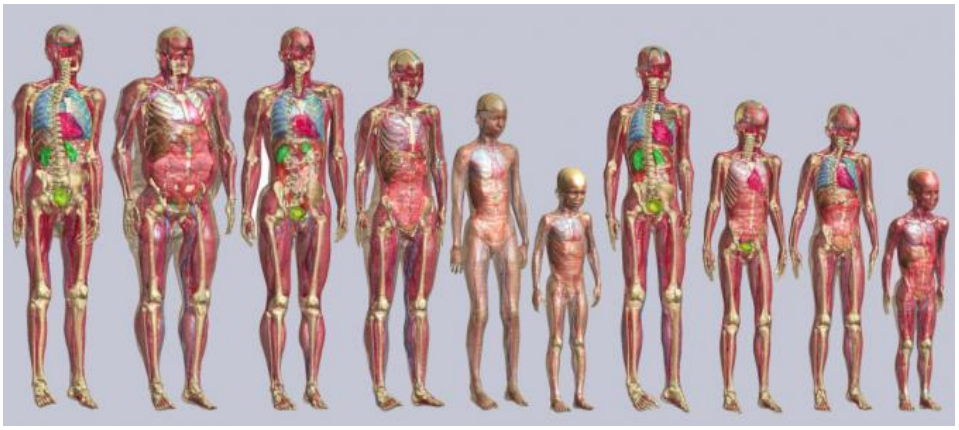

Figure 2.10 – Virtual Population by IT'IS foundation

The simulated fields can be validated with different methods. In MRI $B1^{+}$ mapping or MR thermometry can visualize the excitation profile of a coil and SAR distribution respectively in a phantom or in-vivo. Electromagnetic fields of RF coils could also measured on the lab bench with field probes. However these measurements come with limitations, as a field probe measures the only the magnitude of the field in only one location. Field sampling in the 3D space is possible, however requires elaborated hardware setups.

In this work, SEMCAD X (SPEAG, Zürich, Switzerland) - a FDTD solver - was used for EM simulations. Tissue dependent coil impedance was simulated with organs of the Duke model. This model represents a 37 year old man, with 1.77 m height and 72.4 kg weight, containing 77 different tissue types. The simulated results were compared to in-vivo lab bench experiments, where Q-value variations of the MRI coil were measured with a network analyzer (see Chapter 4).

2.5 Summary

This chapter covered an introductory to RF coil design and RF measurement techniques, which were used in experiments of this thesis. RF coils are based on resonant RLC circuits. Various designs exist, whereas in MRI a parallel LC circuit is most often used for surface coil design. The resistance is typically not added separately but describes the resistive losses of the inductance L. To detect the low relaxation signal of the protons, the coil needs to be tuned to the Larmor frequency with the narrow bandwidth, resulting in high quality factors Q of about 200. In conjunction with tuning, the coils' impedance has to be matched to the system impedance of 50+j0Ω. Accordant tuning and matching circuits are available and the capacitive matching was explained here (Section 2.1.2).

The losses of a coil increase the noise of the signal and affecting the image quality. The different loss effects were investigated in research and allow to define and predict the impact of losses on specific coil types. The most effects can be minimized by coil design metrics, although inductive and capacitive coupling with the sample can hardly be avoided. A equivalent circuit for the interaction of the coil with a conductive sample is shown by [104] and introduced in this chapter. Depending on the application, different coils are available to always achieve a high SNR in each application. The birdcage coil, the single loop coil and the coil array are explained more in detail, as impedance variations were investigate on these coil types.

For RF circuit analysis, S-parameter can give an information about the frequency dependency of the circuit. S-parameter analysis is performed with vector network analyzers (VNA) and delivers essential characteristics of MRI coils like the impedance and Q-value. However, VNAs are expensive and not always available, and coil impedance variations have to be measured with alternative methods. One of these is the direct comparison of forward and reflected power values. Wave reflections occur on an impedance mismatch between two RF components. As the loading of a coil is changing by motion events, power reflections provide information about the resultant impedance change.

As said before, coil loading is due to coupling between the coil and the conductive sample. Biological tissue can be considered as dielectric material, with tissue type dependent permittivity and conductivity values. Different medical diagnostic methods take advantage of this tissue properties by e.g. measuring the body surface impedance. The impact of dielectric changes on MRI imaging coils was investigated in this thesis.

In order to understand electromagnetic fields in various coil designs, numerical simulation methods provide a visualization of these fields. In MRI the sensitivity of a coil design and the interaction with the patient are from major interest. Different methods exist, where the coil geometry can be defined and electromagnetic fields can be calculated. This can be performed on empty coils or with including phantoms or human models. In this research work, EM simulations were performed on lung tissue and compared to network analyzer results.

3

Equipment and methods to measure coil impedance changes

This chapter gives background information about the two collaboration sites at GRC, Munich and IADI, Nancy. Furthermore all methodical aspects are explained. In the collaboration of GRC and IADI, a flexible data acquisition unit ("SAEC") was further developed and built at GRC Munich (Section 3.1.3). This system allowed simultaneous measurement of physiological motion and scan information. The recorded data was used in signal-processing in MATLAB, further explained in Section 3.4.1, as well as in retrospective motion correction with the GRICS algorithm [50] (Section 3.4.2).

Coil loading variations of product coils and self-built loop coils were analyzed and served as motion information sources. Section 3.5 gives information about the loop coil constructions. Different measurement setups were realized for motion detection with the coils (Section 3.2) and accordant software applications were written with LabView (Section 3.3).

My personal contribution on the setup preparation and data analysis includes:

- providing MRI system information to the software developer for new SAEC application
- design and construction of the mobile SAEC system at GRC
- assembling and calibration of all experimental setups described in Section 3.2
- programming of all LabView software
- programming of all post-processing code with MATLAB, except for the filter functions

3.1 The work environment at IADI and GE Global Research

An overview of the research focus and work environment of IADI, Nancy and GRC, Munich is given in the following. One part of this thesis was the further development of the Signal and Acquisition and Event Controller (SAEC), a data acquisition unit designed at IADI [123]. This system and the features of the new version is explained in Section 3.1.3.

3.1.1 Clinical instrumentation at IADI

Currently the laboratory Imagerie Adaptive Diagnostique et Interventionelle (IADI) has 32 full-time employees and 15 PhD students. The research field is motion acquisition and correction for MRI. The aim is to improve the imaging of moving organs for diagnosis in cardiac, pulmonary, renal, liver, and brain imaging, and for understanding the organs' functions. The laboratory is affiliated with the Université de Lorraine in Nancy, the French institute of health and medical research (INSERM), the center for clinical investigation (CIC-IT) and the central university hospital (CHRU) Nancy-Brabois. This enables research close to clinical application and provides access to patients and volunteers for imaging experiments in line with ethical approvals.

IADI has access to a 1.5T HDxt and a 3T HDxt MRI system (GE Healthcare, Waukesha, WI, USA). Both scanners are equipped with a SAEC system in version 2.5.5 for simultaneous motion and system parameter acquisition. Physiological data can be acquired with MR-compatible patient-monitoring devices (Maglife, Schiller, Wissembourg, France), which also support cardiac triggering of the MRI scanner. These patient monitors support two respiration belts and four-lead ECG signals, and are modified for usage with the SAEC system. For this work, the 3T system was used for a volunteer study (Section 6.2) and reflected transmit power measurements (Section 5.1).

To archive image data of the different research studies, the lab developed its own picture archiving and communication system (PACS) "Archimed." This allows the import of SAEC information and data from various devices or research prototypes to archive images with their corresponding motion information. Dedicated MATLAB scripts, which communicate with the Archimed server, allow effective post-processing of images and sensor data.

3.1.2 RF and MRI labs at GE Global Research

The present research focus of the the Diagnostics, Imaging and Biomedical Technologies Laboratory (DIBT) at GE Global Research Europe in Munich is on the optimization of MRI pulse sequences and image reconstruction for cardiac and neurology applications. Further research areas are MRI spectroscopy, electromagnetic field simulations, and X-ray imaging.

At DIBT, two 3T MRI systems - a 3T HDxt and a 3T MR750w - are currently available. The main technical differences of both systems are shown in Table 5. For this work, the HDxt system was used for all non-clinical single-loop coil (Section 6.1) and coil array experiments (Section 6.3), as well as for the investigation on birdcage coil harmonics (Section 5.2). Reflected transmit power measurements were performed on the MR750w system (Section 5.1).

For electronic development, smaller mechanical tasks, and coil building, an electronic workshop - the "RF lab" - is available. A set of laboratory devices, such as power supplies, oscilloscopes, signal generators, as well as some mechanical tools are deployed for developing imaging coils or other research prototypes. For MRI coil construction, a two-port and a four-port Rohde&Schwarz network analyzer (ZVB2

	3T HDxt system	**3T MR750w system**
Imaging FOV (X,Y,Z)	450,450,480 mm (440,440,350 mm)*	500,500,500 mm
Max. gradient slew rate	80 T/m/s (150 T/m/s)*	200 T/m/s
Max. gradient amplitude	23 mT/m (50mT/m)*	44 mT/m
RF transmission	one channel in I/Q configuration	two independent channels in quadrature or independent mode
Max. RF output power	35kW body, 4kW head	2x15kW body, 4,5kW head
Receivce channels	16	32
Tunnel diameter	600mm	700mm

Table 5 – Technical specifications of GE HDxt and MR750w MRI systems; *) Gradient system can be driven in two different configuration

and ZVB4) are provided. Also, several RF components like amplifiers, power splitters, couplers, switches or mobile power meters were utilized for many experiments in this work. A detailed list of the used equipment can be found in Table 6.

Equipment type	**Manufacturer**	**Product name**
vector network analyzer	Rohde&Schwarz	ZVB4
signal generator	Agilent	A3320
power sensor	Rohde&Schwarz	NRP-Z11
frequency synthesizer	PTS	PTS 160
USB - DAC	National Instruments	USB-6008
frequency doubler	MiniCircuits	MK-3
RF amplifier (+23dB)	MiniCircuits	ZHL-3010+
high-pass filter	MiniCircuits	BHP-100+
directional coupler (-6 dB)	Werlatone	C6933-102
directional coupler (-30 dB)	Werlatone	C1569-12
RF switch	Teledyne	CCS-32N50-T-1
lab power supply	Rohde&Schwarz	NGMO2

Table 6 – RF lab equipment used for experiments in this thesis

3.1.3 Signal Acquisition and Event Controller (SAEC)

The SAEC is a system designed to acquire and save data from different sources and different signal types in real-time. It was designed by the IADI lab in 2007 [123] with the aim of precisely acquiring MRI scan information and physiological data, whereupon the signal sources are determined on GE MRI systems and Schiller Maglife patient monitors. This system was re-built and extended as a part of this thesis.

The system consists of two parts: the data-acquisition electronics and a Linux computer with a real-time kernel (Fig. 3.1). Physiological data from the modified Schiller Maglife system is transferred via fiber-optic cables. Optoelectronics and TTL-to-RS232 converters (FTDI Chip, Glasgow, UK) route the patient monitor data to a USB hub for further processing in the computer. The following MRI system data is acquired by PIC micro-controllers (Microchip, Chandler, AZ, USA):

- time progress of X-, Y- and Z-gradients
- RF envelope of transmit pulses
- time point of image acquisition ("acquisition window") as a TTL signal

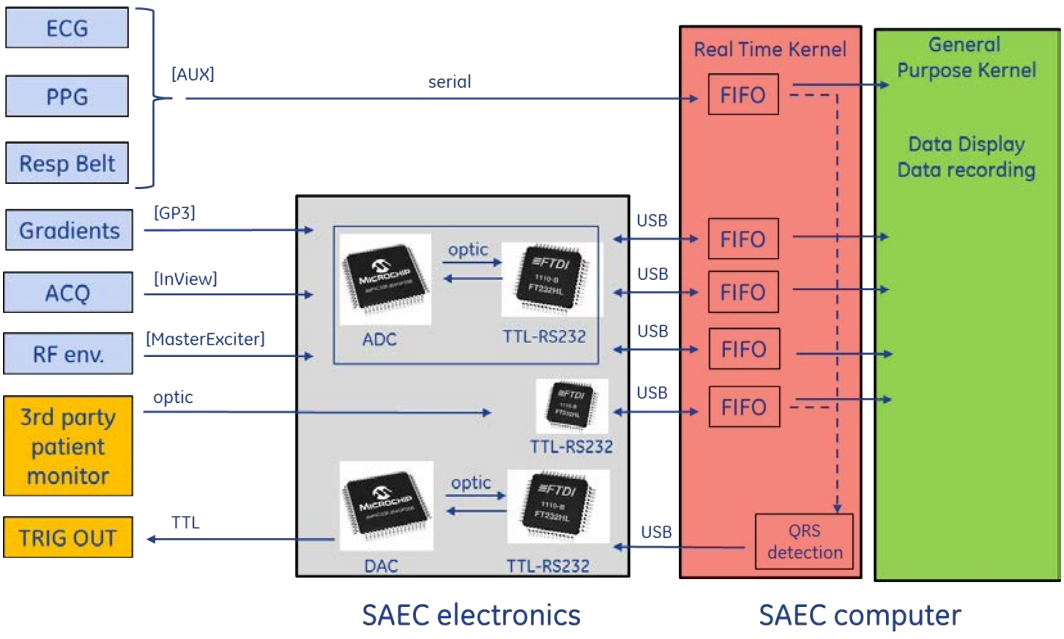

Figure 3.1 – Schematic of the new SAEC system; Blue areas is data provided from MRI system. Indications in [] are the connection ports at the GE HDxt MRI system

The gradient signal is routed through an additional third-order low-pass filter to suppress RF signals on cables. The corresponding connections are directly available at the system cabinets of the GE HDxt MRI systems. To ensure galvanic isolation, the output of the PIC boards is converted into an optic signal, routed through fiber optics to the FTDI converters and via RS232 communication to the USB hub. Due to different signal frequencies, the sampling rates vary according to the signal frequency

(Table 7): The Linux real-time kernel acquires the data and stores it in first-in first-

Singal type	sampling frequency
RF signal	15 kHz
Gradients	5 kHz
ACQ	190 Hz
ECG (Maglife)	1 kHz
Respiratory Belt (Maglife)	1 kHz
ECG (MRI)	200 Hz
Respiratory Belt (MRI)	200 Hz
Pulseplethysmograph (MRI)	200 Hz

Table 7 – Sampling frequencies of the SAEC system

out (FIFO) buffers. A QRS detection for the ECG signal is implemented and the trigger signal generated can be applied to the MRI system (TRIG OUT). The non time-critical functions, such as data display in the graphical user interface (GUI) and storage, are performed by the general-purpose kernel. Additionally, low- and band-pass filters can be applied to the acquired data. The acquired data is saved in a proprietary .AEC-file, which can be extracted with a dedicated MATLAB code.

Features of SAEC version V2.7.5

The new version V2.7.5 was developed in collaboration between GRC and IADI, and is used at both locations. A mobile model of the new SAEC was built at GRC in a moveable 19 inch rack (Fig. 3.2). One new feature is that physiological data from the MRI system can be acquired. The GE HDxt MRI platform allows the transfer of the respiratory belt signal, the peripheral pulse signal, and the ECG signal via an RS232 protocol. The SAEC software was modified so that it also monitors the nine-pin D-sub serial port of the computer for incoming signals besides the information received from the USB hub. This allows the acquisition of physiological information directly from the MRI system, without the third-party patient monitor. Some further modifications on the GUI, the data acquisition on the PIC boards, and the galvanic isolation were implemented in this version. For the experiments described in Section 6.1, the input signal configuration was changed. The PIC board for the gradient signals was reprogrammed to an RF signal port. This change to two RF input ports enabled the acquisition of the pre-filtered respiratory and cardiovascular motion signals by coil load changes. The filtering and scaling was performed by a LabView application (Section 3.3) in this case.

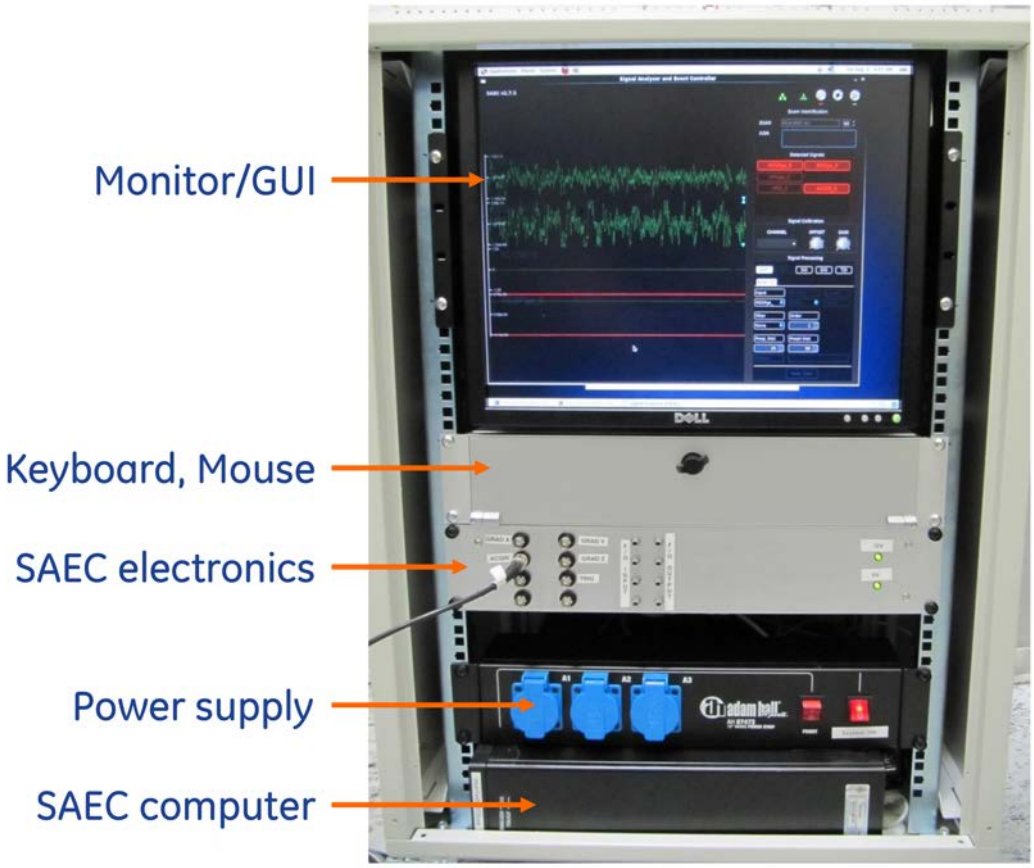

Figure 3.2 – Mobile SAEC at GRC Munich: All components are mounted in a 19 inch rack. Data transfer is available through USB and TCP/IP (for saved data only)

3.2 Measurement systems for coil load change acquisition

The measurement of motion induced coil load changes was performed with different setups on various coils:

- The reflected power of the body birdcage coil during the RF transmission pulse was measured (Section 3.2.1)
- A flexible, MR system independent power reflection measurement setup was built. This setup was applied on lab-bench experiments with body coil modes and single loop coils (Section 3.2.2)
- For power monitoring on birdcage coil modes during imaging, a dedicated switching logic was designed (Section 3.2.3.1)
- An experimental setup for continuous S-parameter recording of a single loop coil was established for a volunteer study at IADI and for a multi-channel coil array (Section 3.2.3.2).

The different setups address the individual needs for the measurements (e.g. switching the coil between motion measurement and imaging). Especially the latter is unique in its kind, as it uses the VNA for impedance measurement during imaging, which differs from the typically usage in lab-bench experiments.

3.2.1 Reflective power measurement on MRI RF amplifier

Coil impedance variations can be measured by the reflection factor or the ratio of the transmitted power P_{FWD} to the reflected power P_{REF} (see Section 2.2.2). In MRI the incident power of the transmit RF pulses is typically constant throughout the scan. For instance in a Spin Echo sequence, the excitation with a flip angle $\alpha = 90°$ and the refocusing pulse $\alpha = 180°$ have fixed values, while the gradient play-out varies for spatial encoding. Therefore, the reflected power P_{REF} measured at the RF amplifier directly represents the reflection factor changes on the coil and is used to monitor the power deposition in the patient.

The RF amplifiers of both, the 3T MR750w and HDxt system, provide connections to internal directional couplers. The coupling attenuation is -51 dB and -69 dB respectively. For measuring the reflected power of the excitation RF pulse, two power sensors were connected to the forward coupled port ("FWD") and reflected coupled port ("REF") of the RF amplifier. The power of the excitation pulse was integrated over the duration of this pulse (Fig. 5.1). The power meters were triggered by the "scope trigger" signal of the MRI system. This signal is a TTL pulse at the beginning of every pulse sequence cycle and is provided at a dedicated port on the MR system electronics. The data of the respiratory belt and the reflected power of the body coil were recorded separately on the MRI system and merged with MATLAB retrospectively.

3.2.2 Flexible power reflection measurement system for MRI coils

An MRI system independent setup was built to measure coil load variations on loop coils at various positions on the human body (Section 6.1) and on birdcage coil mode frequencies (Section 5.2). Fig. 3.4 gives a schematic overview of the setup. This setup consisted of an external RF source (PTS Inc., MA, USA) with a continuous wave (CW) signal of 10-160 MHz and 0-10 dBm output power, which was connected to a directional coupler with 6 dB coupling attenuation. A constant power of $P_{FWD} = 10$ mW was applied to the loop coils described in Section 3.5. The reflected power was measured with a Rohde&Schwarz power sensor connected to the coupled reflected port of the directional coupler. A dedicated LabView application was written to read, process, and save the reflected power values. This is explained in detail in Section **??**. The measurement on the birdcage coil modes was performed

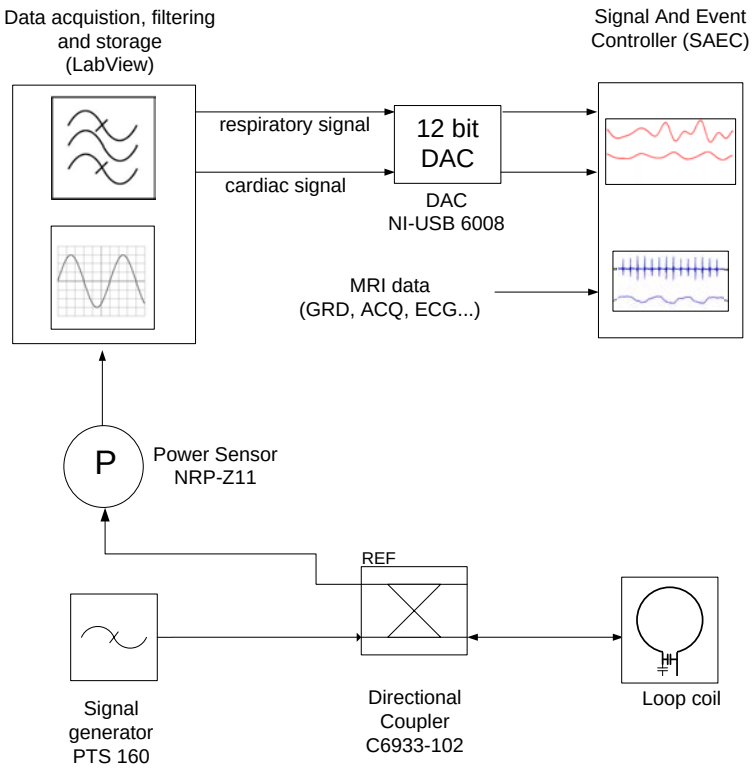

Figure 3.3 – Schematic of motion acquisition by reflected power measurement: A continous wave signal from the signal generator is transferred to the loop coil via a directional coupler. Reflected power is measured at the coupler with a power meter. This power is scaled and filtered and forwarded to a DAC, which converts the signal into voltages for the SAEC input. For comparison physiologic signals and sequence parameters from MRI can be routed to the SAEC

on the I-port of the coil, while the Q-port was terminated with 50 Ω. A frequency multiplier and an amplifier (MiniCircuits, NY, USA) were placed at the output port

of the RF source to generate frequencies larger than 160 MHz. The amplifier has a fixed gain of 23 dB to compensate for the insertion loss of the multiplier and to ensure incident power of 10 mW in the coil.

3.2.3 Coil load measurements during imaging

Impedance measurement during imaging requires additional care in the design to avoid component damage by the RF excitation of in the kW-range and ensure volunteer safety. Two different setups are introduced here. The first one outlines the imaging and motion capture with the same birdcage coil by introducing a switching logic (Section 3.2.3.1). The second setup covers the continuous and simultaneous motion detection with a loop coil at a different resonance frequency and a S-parameter measurement with an VNA (Section 3.2.3.2).

3.2.3.1 Motion tracking on mode frequencies of a birdcage coil

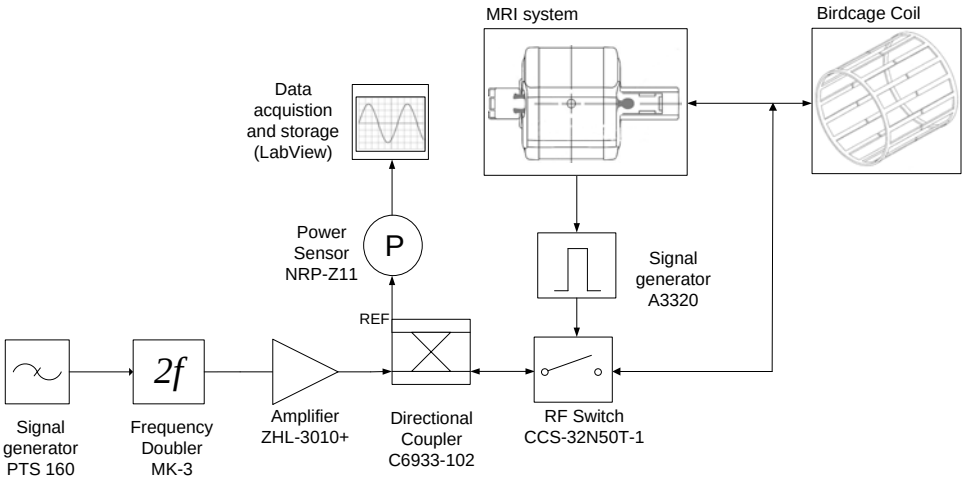

Figure 3.4 – Schematic of switch setup for motion acquisition on birdcage coil modes. The switch is controlled by an delayed trigger pulse of a pulse generator and disconnects the measurement system during excitation and image acquisition

In this experiments, coil load variations were recorded during imaging. In one case, the motion signal was derived from modes of a head birdcage coil, while the resonant mode at the Larmor frequency was used for the transmission and reception of the imaging signal (Section 5.2.2). To avoid interaction of the current on the two frequencies, an electro-mechanical RF switch was disconnecting the motion measurement setup during excitation pulses and image acquisition (Fig. 3.4). The

RF switch was placed in between the coil and the coil connector to the system. Since the ports of the switch have an impedance of 50 Ω, the transmit signal to the coil and the receive signal back to the system was not influenced by the additional RF switch. The switch was controlled by a TTL signal of a signal generator. The TTL pulse length and the delay of the signal generator were defined manually according to the TR and TE time of the pulse sequence. The scope trigger signal of the MRI system ensured synchronized switching with the pulse sequence (see also Fig. 5.9).

3.2.3.2 Continous measurement of S11 data of a 31P-loop coil

In a second in-vivo experiment, a 150 mm ^{31}P loop coil (GE Healthcare, Waukesha, WI USA) tuned to the Larmor frequency of ω_0(3T)=51.7 MHz was utilized for motion detection, during image acquisition with the birdcage body coil (Fig. 3.5). The coil was connected to a vector network analyzer (VNA) and S11 parameters were acquired continuously at the ^{31}P Larmor frequency. The VNA was set in CW mode with a power level of 0 dBm. A LabView application collected the data from the VNA via a TCP/IP connection and transferred the signal via a 12-bit digital-analog converter to the SAEC system. The motion data of the VNA, the ECG, the respiratory belt data, and QRS-trigger events of an external patient monitor, and the acquisition window trigger of the MR system were recorded by the SAEC simultaneously. Before the volunteer measurements, phantom tests were performed

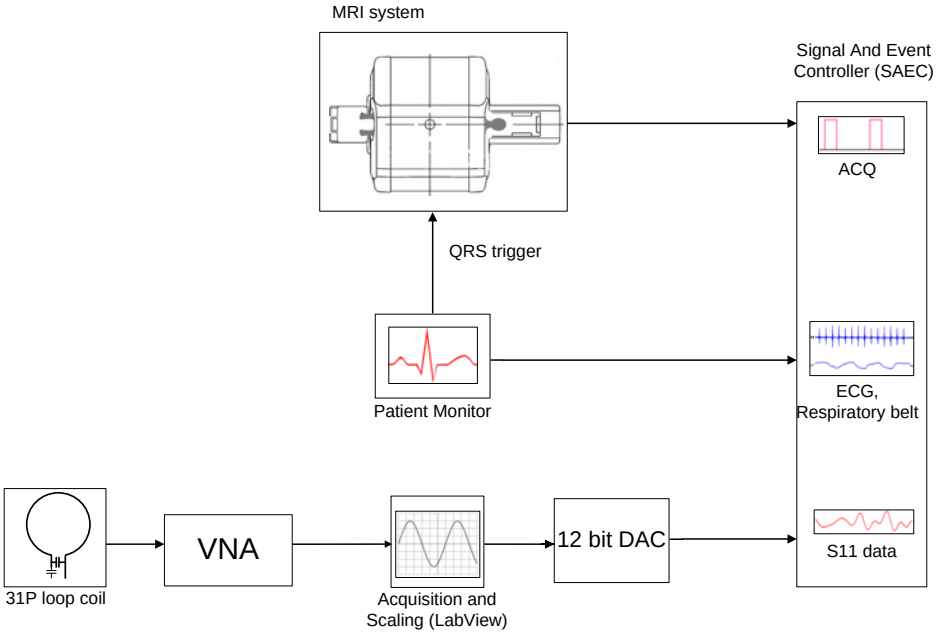

Figure 3.5 – Schematic of motion acquisition setup with VNA

to evaluate coupling and common mode effects between the two coils. For this, a power sensor was connected with the ^{31}P loop coil via the filter panel. Power levels during imaging sequences with the phantom-loaded birdcage coil were below 10 μW,

which reflected no coupling between the main ^{1}H body transmit coil and the ^{31}P loop coil or induced currents on the cable shield.

The various experimental setups provide motion information based on coil load changes on the lab-bench as well as during image generation in the MRI. To analyze and compare the data to state-of-the-art techniques or use it for retrospective motion correction, it needs to be recorded and processed. In the following, software applications are presented, which control power sensors or VNAs, process and save the data or forward it to the SAEC system.

3.3 LabView applications for coil load changes

LabView from National Instruments (NI) is a graphical programming environment especially designed for measurement and control tasks. To acquire this data, the user can choose between NI or third-party hardware modules or drivers for third-party equipment - e.g. measurement instruments, sensors or actuators. LabView provides a variety of signal processing, visualization, and storage software packages, as well as intuitive tools to generate GUIs. The source code is written in a graphical flowchart diagram on which multiple objects, the so-called virtual instruments or VIs, are connected with wires. GUI elements are also directly connected to the flowchart diagram, which allows effective programming of software applications. LabView provides an easy way to interact with the sensing hardware or acquired signal and is suited for fast prototyping for research as well as comprehensive test applications for production lines.

For data acquisition in this work, LabView applications were written to retrieve data from a RF power sensor or a VNA, to filter and save the data, and to transfer it via a digital-to-analog converter to the SAEC. To optimize the sampling rate, the application was designed in a producer-consumer pattern (Section 3.3.1). For concurrent signal recording with other sensors and MRI sequence data, the acquired motion data had to be transferred to the SAEC (Section 3.3.2). For the simultaneous read-out of the transmission and reflection coefficients of a four-channel network analyzer a modified version was used. Because of the limited input ports of the SAEC electronics, the data of the ten motion signal sources (transmission and reflection S-parameters) was saved locally in that case (Section 3.3.3).

A continuous control of the motion capture was necessary during the experiments. Therefore, the data acquisition and processing was visualized in a GUI. The GUI of the application for the power sensor is shown in Figure 3.6. Settings for measurement parameter, filters and data transfer are available as well as a graphical illustration of the acquired data. Furthermore this software provided raw data and filtered data recording and manual or automatic scaling of the output signal to the SAEC.

3.3.1 The Producer-Consumer-Architecture

The producer-consumer design enables data sharing between two separated processes with different processing times. Data handling like filtering or storing typically takes longer than data acquisition. A sequential cycle of data acquisition and processing leads, therefore, to slower sampling rates. This can be avoided by running both processes in parallel and buffering the data in data queues. In LabView, the two processes are the producer loop and the consumer loop, whereby data from the producer loop is stored in the queue and read by the consumer loop in the next loop cycle. Due to its FIFO buffer, the consumer loop reads and processes the data in the same order as it was acquired.

The producer loop for the following experiments, had two main functions in sequential order. The first function was the data acquisition of the measurement device (power sensor or VNA) and writes the measured value in the data queue.

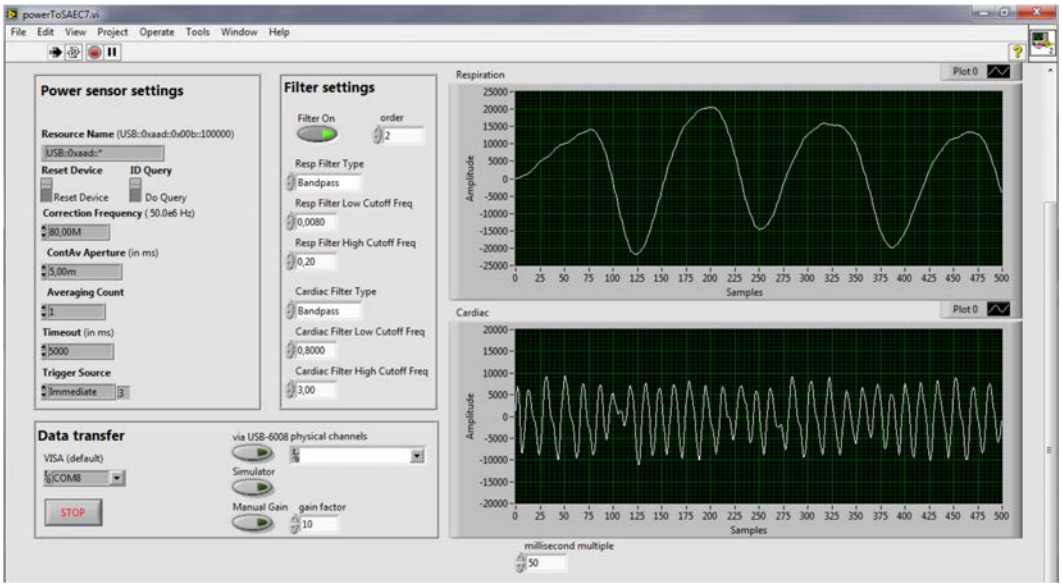

Figure 3.6 – GUI of a LabView application for reflected power measurement. Respiratory and cardiac filtered signal is visualized. Data transfer options, filter parameter and sensor settings are available

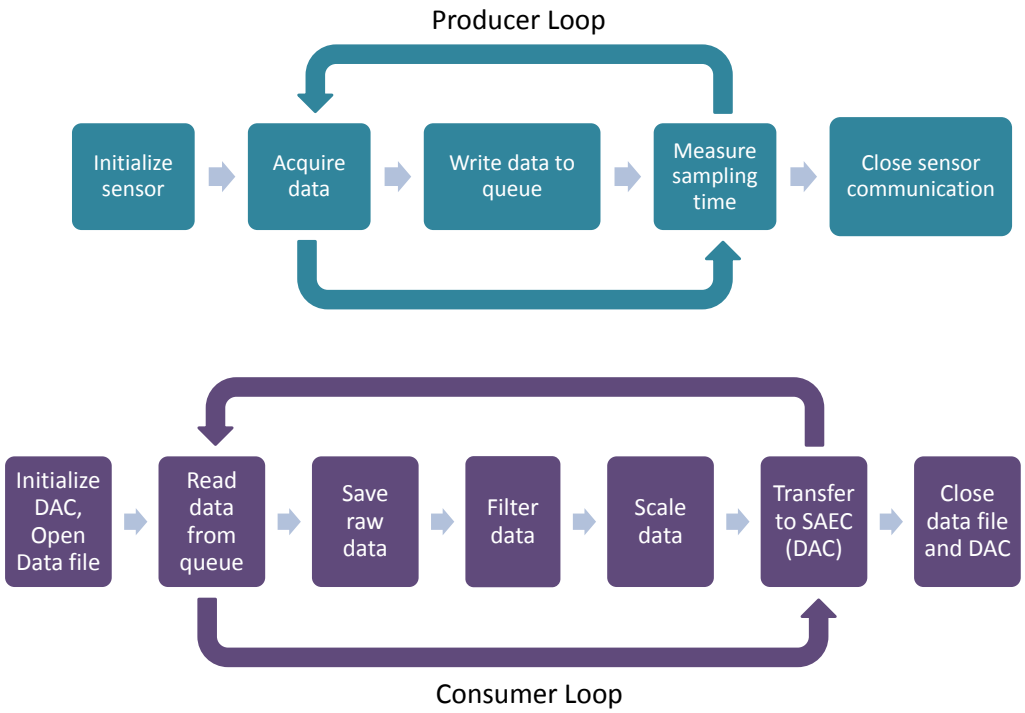

Figure 3.7 – Schematic of LabView data acquistion application

The second function determined the current time. A subtraction of the time from the previous loop cycle yields the duration of one measurement cycle and, therefore, the effective sampling rate of the data, which is used for filtering and data storage.

Data processing as normalization, filtering, storage, and transfer is performed in the consumer loop. The data processing varies by application and is further explained in the following sections. After starting the application, the initialization processes of the devices or data storage are performed. Similarly, memory release, communication termination, and error processing takes place after stopping the application (see Fig.3.7).

3.3.2 Transfer of power meter measurements to SAEC

To transfer the recorded power to the SAEC system, the data has to be adapted to the input voltage range of 0V to 3.3 V. A linear scaling of y=mx+b was used with

$$m=(Out_{max} - Out_{min})/(In_{max} - In_{min})$$

and

$$b=Out_{max} - m * In_{max}.$$

In_{max} and In_{min} are the boundaries of the measured data, and Out_{max} and Out_{min} the data range of the output voltage of the DAC. These values were either defined manually by observation of the data, or automatically by analyzing minimum and maximum value of an array of 1000 values. A "freeze" function interrupts the automatic analyses and fixes the current values.

In addition to scaling, a filter for the respiration and cardiac motion is implemented and selectively available. The filters were chosen from the LabView Point-By-Point library, which allowed filtering in real-time without the necessity of acquiring multiple data points before filtering. Two second-order Butterworth band-pass filters with cut-off frequencies of 0.05 Hz and 0.5 Hz for the respiratory signal and 0.8 Hz and 3 Hz for the cardiac signal are utilized. These values were reported for separating respiratory and cardiac motion in [73]. A filter delay of 254 ms was determined by investigating the pulse response of the filter and correction was applied in the data post-processing.

The signal for the SAEC is transmitted by the 12-bit DAC NI-USB 6008. The DAC is controlled via USB 2.0 and provides, besides eight analog inputs and 12 digital I/O ports, also two analog outputs. The output voltage range is 0 V to 5 V with 5 mA current per port and a 150 S/sec update rate. This update rate was sufficient, since the data-sampling rate in the producer loop was limited by the measurement cycle of the used equipment and was typically at 125 S/sec. For the transfer of the filtered data, both ports are used - one for the respiratory signal and one for the cardiac signal.

In volunteer experiments described in Section 5.1, 5.2.2 and 6.1, the data was filtered in the LabView application before the transfer to the SAEC. This setup required both output ports on the DAC to transfer the filtered respiratory and cardiophysiologic signals. The pre-filtering in LabView was not used in the experiments described in Sections 6.2 and 6.3. Here, raw data was transferred to the SAEC, which required only one DAC output channel. The raw data was saved simultaneously and filtering was applied in the post-processing with MATLAB. The filter parameters

were chosen as described above. However, the filtering was performed in the forward and backward directions to eliminate filter delays.

3.3.3 Continuous S-parameter recording with a VNA

Besides reading the power values of a power meter, the temporal impedance change can be recorded by the acquisition of scatter parameters of a VNA. The VNA needs to be set into CW mode at a fixed frequency. The initialization routine has to define the correct frequency for the CW mode:

1. Initialize VNA communication
2. Perform a single frequency sweep on each port
3. Define the minimal reflection factor on each port (= resonance frequency f_0)
4. Set CW mode frequency and power: $f_{CW} = f_0$, P_{CW}=0 dBm
5. Set traces to measure (1 trace for single S11; up to 10 for all ports)

Depending on the number of used ports, up to 10 S-parameter traces need to be defined on the four-port VNA (four reflection coefficients, six transmission coefficients). After initialization, the producer loop acquires the data of all traces continuously and saves it in the data queue for further processing.

For the volunteer measurements in Section 6.2, only one port of the VNA was used to acquire S11 data from a loop coil. Similarly to the LabView power meter application, the data was scaled and send directly to the DAC. Inline filtering was only used for visualization and control purposes. For multi-channel S-parameter measurements in Section 6.3, the data was saved in a CSV-file, as the SAEC and DAC were not able to handle 10 signals simultaneously. Visual control and filtering of one user-defined channel was implemented as well.

3.4 Post-processing methods

3.4.1 Signal processing with MATLAB

For data analysis the software application MATLAB (Mathworks, Natick, Tx, USA) was used. SAEC data was imported by proprietary scripts of IADI. All saved signals were normalized first. If the coil load data was pre-filtered by the LabView application, a filter delay compensation was applied to the signal. This fixed compensation value was verified by cross-correlation of the filtered respiratory signal of the coil and the pneumatic belt signal. If the raw signal was saved, the filtering was performed in the post-processing. Two second-order Butterworth filter with the same parameters described in [73] were used. The cut-off frequency of the cardiac triggering was set to 0.8 - 3 Hz. The respiratory signal was filtered with a low-pass filter and a cut-off frequency of 0.5 Hz. These values also correspond to the filter settings in the LabView application.

Comparison of the respiratory coil signal with the pneumatic belt was performed by linear regression. In the experiments described in chapter 6.1 and 6.2, ECG and coil data were superimposed for one interval between two R-peaks (R-R interval) (Fig 3.8). A simple peak detection was performed on the R-peak of ECG signal and the single intervals were superimposed. The coil data was also segmented and superimposed for the same time frame. For visualization the overlapped data is presented with its mean value and the standard deviation as a semi-transparent area. Depending on the data set length between 130 and 383 R-R intervals were segmented and overlapped. A higher standard deviation was observed in the end-diastolic phase, caused by physiologic R-R cycle length variations throughout the acquired data set. The superimposed coil data was compared to simulated and measured left ventricular volume changes.

In chapter 6.2 the peak detection algorithm was also applied to the coil data. The R-R intervals of the ECG peaks and the S11 peaks were analyzed to evaluate the potential of the S11 signal for cardiac triggering.

3.4.2 Image processing and quality metric

The GRICS reconstruction algorithm

Free-breathing images suffer from ghosting artifacts and need to be retrospectively corrected. The reconstruction algorithm for Generalized Inversion Coupled Systems (GRICS) [50] was developed for that purpose. The problem of image reconstruction of motion corrupted MRI raw data can be formulated as a mathematical optimization problem where both the image and movement are unknown:

$$\min_{(\rho_0,\alpha)} \left\| E(\alpha)\rho_0 - s \right\|^2 + \mu R(\alpha) \tag{3.1}$$

with s the acquired k-space data, α the motion induced displacement field, E(α) the operator simulating the MRI image acquisition process, ρ_0 the reference image, μ a weighting factor and R(α) a regularization term. In this general form, the problem is

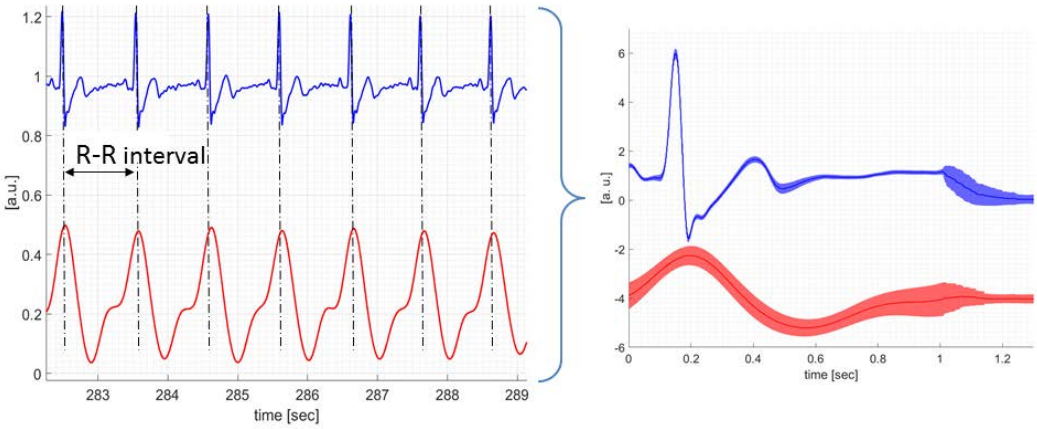

Figure 3.8 – R-peak detection and superposition of cardiac data. The ECG (blue) and coil data (red) was superimposed for each R-R interval. Right: Blue and red line represent the mean value of the superimposed data, the semi-transparent areas represent the standard deviation. A higher standard deviation toward the end-diastole is observable due to R-R interval inconsistencies.

mathematically under-determined. The assumption is made, that the displacement field is temporally correlated with physiological motion data, which is simultaneously recorded during the image acquisition by a motion sensor. To solve the problem of the coupled system of the image and the displacement, the algorithm alternates between optimization of the image (assuming a known displacement fields) and optimization of the displacement fields (assuming a known image). To allow estimation of large displacements, a multi-scale strategy is employed.

To apply GRICS imaging on Cine images, the reconstruction has to be split. The cardiac cycle is divided into cardiac phases, and the GRICS reconstruction is launched on each cardiac phase independently. The choice the number of cardiac phases and the duration of each heart phase is based on experience and defined by the user. Similar to the original GRICS algorithm that performs respiratory motion compensation, Cine-GRICS adds a cardiac motion compensation within each cardiac phase [124].

Image entropy for quality quantification

In the volunteer experiment described in Section 6.2, a metric to quantify the image quality was used. An indicator for the performance of a motion correction is the reduction of blurring or the sharpness of the edges in the image. By calculating the image entropy, the texture of the image can be characterized. The image entropy E can be calculated by [125]:

$$E = -\sum_{p=1}^{M} \frac{B_p}{B_{max}} ln \left[\frac{B_p}{B_{max}} \right] \tag{3.2}$$

with B_p the modulus of the complex value of the pixel p, M the number of image pixels and B_{max} the maximum image energy defined by

$$B_{max} = \sqrt{\sum_{p=1}^{M} B_p^2} \tag{3.3}$$

A higher entropy implies a reduction of blurring and sharpening of the edges e.g. after motion correction. This metric allowed the direct comparison of different motion signal sources in the GRICS algorithm.

3.5 Coil design for load change experiments

The evaluation of coil load changes caused by motion was performed primarily on product coils of the manufacturer. For lab bench experiments two single loop coils were designed and compared to results numeric simulations. Furthermore these coils were utilized to investigate local coil changes on different body parts.

The coil layout was etched from a copper PCB board with a diameter of 75 mm and conductor width of 8.0 mm. A coil conductivity of L=140 nH was measured. Two coils were built with a resonance frequency of f_0(1.5T)=64 MHz and f_0(3.0T)=127.7 MHz to investigate motion effects on proton Larmor frequencies for 1.5T and 3.0T. The capacitance of 11 pF and 44 pF respectively was balanced between the tuning capacitor C_t and C_1 (Fig 3.9b) and the resulting virtual ground was connected to the cable shield. On the 128 MHz coil, another capacitor C_2 was introduced to split the loop and assure a conductor length smaller then $\lambda/10$. Tuning and matching capacitors were included as variable capacitors. After adjusting the resonance frequency as close as possible to Z_0 =50+j0Ω, the variable capacitors were replaced by fixed value parts. Table 8 shows the values of the capacitors and Q-values of the two coils. For the experiments the coil was covered with a 10 mm foam material on both sides. This did not introduce any measurable changes to the parameter of the coils.

f_0 [MHz]	C_m [pF]	C_t [pF]	C_1 [pF]	C_2 [pF]	Q-ratio
64	5.7	83	82	-	6.65
128	3.7	31.9	30	30	12.54

Table 8 – Capacitor values and Q-ratios for single loop coils

3.6 Summary

Load variations on different coils were examined in lab-bench and imaging studies. For the different experiments, individual solution in the design were necessary. This resulted in four experimental setups, whereas three of them were applicable for motion recording during imaging. Motion information of the reflected power of transmit pulses (Section 3.2.1), of birdcage coil modes (Section 3.2.3.1) and of a ^{31}P single loop coil (Section 3.2.3.2) were recorded while image data was acquired. A flexible

(a) 127.7 MHz single loop coil with 75 mm diameter and 8 mm conductor width

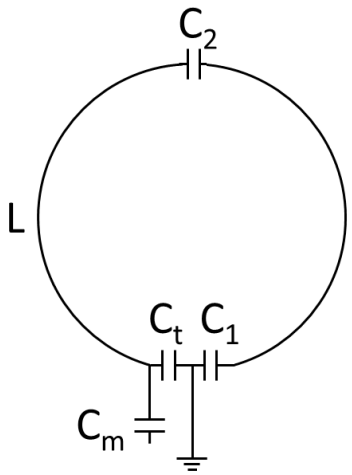

(b) Coil schematic

Figure 3.9 – Photo and schematic of single loop coil for motion capture

coil load acquisition system was designed, which allows the continuous recording of loading variations independent from the coil used and independent from the MRI system (Section 3.2.2).

The power measurement and S-parameter recording was controlled by LabView applications, which processed the data, visualized it and transferred it to the SAEC (Section 3.1.3). In addition, data was saved locally. To ensure a sufficient the sampling rate, the measurement process and data management process were separated by the producer-consumer design. Accordant data post-processing was applied with MATLAB (Section 3.4.1) for filtering and analysis of the recorded motion data, for comparison to other sensors and for GRICS reconstruction (Section 3.4.2).

A new version of the SAEC was developed and built as a mobile unit at GRC. It was used for in-vivo experiments described in Section 5.1.2 and 6.1. Furthermore, a SAEC system in Nancy recorded data during the volunteer study described in Section 6.2.

All activity which was necessary to establish the experimental setups and data analysis were realized by myself. However I want to highlight the strong cooperation and support from IADI for the SAEC development and the GRICS reconstruction, which were crucial parts for the experiments and this thesis.

Part II

The effect of coil load changes caused by motion

4

Numerical analysis of coil load changes

In the following chapters, the results of EM simulations on coil load changes are presented and compared to lab bench experiments. Details on simulation design are given in chapter chapter 4.1. The influence of a homogeneous loading phantom on the Q-value is presented in section 4.2. Tissue dependent loading and the effect of respiration is analyzed and compared with lab bench experiments on a vector network analyzer (section 4.3).

It has to be mentioned and thankfully acknowledged, that the EM simulations were conducted by Alexia Missofe and Julie Kabil from IADI. The baseline data, like coil design parameters, conductivity values and the simulation setup was provided from my side. Also the subsequent data analysis was performed by myself.

4.1 EM simulation design on coil load variations

The simulation was performed with EM-simulation software SEMCAD X(v14.8, SPEAG, Zuerich, Switzerland). The 75 mm-loop coil, as described in Section 3.5, was reproduced with a resonant frequency of 64 MHz and 128 MHz. The simulation was performed with the coils positioned on a phantom and on a human body model respectively. The impedance change and Q-value analysis of the coil were performed at:

- a phantom simulating a saline solution with a salt concentration of 0.9%
- the sternum position of a human body model
- the sternum position with the dielectric properties of the deflated lung
- the sternum position with the dielectric properties of the inflated lung

The conductive phantom was simulated as a rectangular box, with the dimensions 270 mm x 100 mm x 37 mm to cover the full sensitivity area of the coil. The salt concentration was chosen so that it corresponds to commercially available sodium chloride solutions that are used in clinical practice. Its conductivity was found to be σ = 1.4 S/m at a temperature of T = 20°C [9]. In order to reduce the simulation time for the human body model, all organs and body parts were removed except for the heart and lung tissue. By default, the coil had a distance to the tissue of 3 mm (Fig. 4.1).

The results of the simulations were compared with lab bench experiments with a VNA. The loop coil was loaded with a bag of 0.9% sodium chloride solution (NaCl 0.9% Ecobag, B.Braun, Melsungen, Germany). Inhale and exhale experiments were performed with the coil at the sternum of one human subject. Ten repetitions, each

with breath-hold in the inhale and exhale states, were carried out and the Q-value of the coil was measured at each breath-hold.

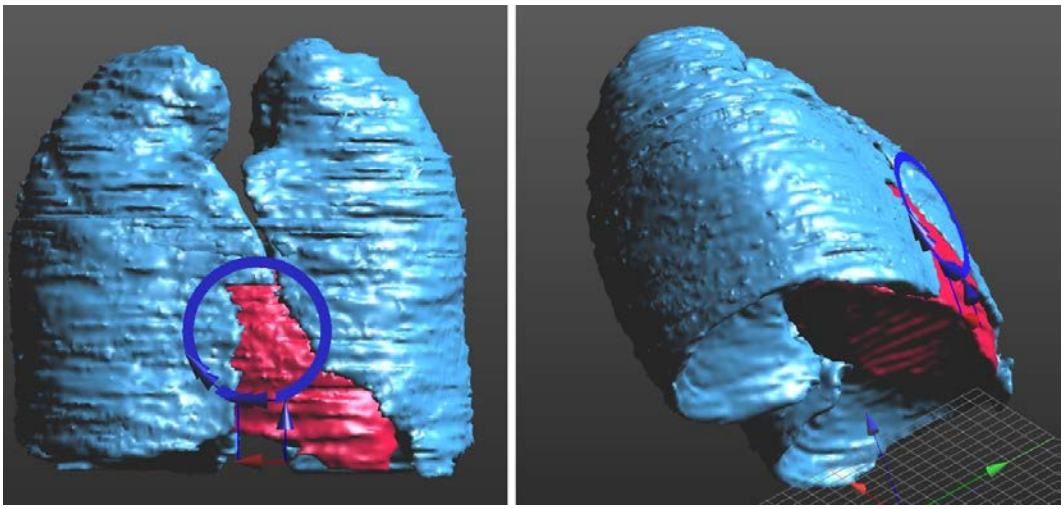

Figure 4.1 – Coil position on human body model. The coil was placed at the lower sternum position with a default distance of 3 mm. Tissue in blue represents the lung tissue of the human body model, tissue in red the heart tissue.

4.2 Simulated and measured Q-values on a homogeneous load

	64MHz coil		128MHz coil	
	simulated	measured	simulated	measured
f_0 unloaded [MHz]	65.01	64.86	127.52	128.92
f_0 loaded [MHz]	64.62	64.0	129.65	127.7
Q_u	137	173	140	163
Q_l	21	26	11	13
Q-ratio	6.52	6.65	12.72	12,54

Table 9 – Simulated and measured coil parameters coil parameters of two loops coils with f_0=64 MHz and f_0=128 MHz; Q_u is the unloaded Q-value and Q_l the loaded Q-value. Loading was performed with a 0.9% saline solution.

As shown in Table 9 the unloaded and loaded Q-values and resonant frequencies f_0 are in good correlation to the lab bench measurements (R^2 = 0.97). The frequency shift between the loaded and unloaded state is low in both cases (Δf = 0.4 - 2.1 MHz), while the Q-ratio of about 6.5 and 12.6 is shown respectively. This indicates a good coil design with a primary sample influence and low radiation losses.

For comparison, the sample loss calculation for a circular loop coil with a homogeneous load was applied to the current coil design. The sample loss is defined in [126] as

$$R = 0.0332\sigma(\omega_0\mu_0\pi)^2 r^3 \tag{4.1}$$

with σ the samples conductivity, ω_0 the angular frequency, $\mu_0 = 4\pi 10^{-7}$ N/A^2 the permeability of free space and r the radius of the coil. With r = 75 mm, σ = 1.4 S/m and the resulting sample resistance inserted in Eq. 2.16, one obtains a loaded Q-value of Q_l(64MHz) = 19.5 and Q_l(128MHz) = 10. This corresponds well to the measured data of Q_l(64MHz)= 26 and Q_l(128MHz) = 13 as well as the simulated data (Q_l(64MHz)= 21 and Q_l(128MHz) = 11). This verifies the correct modeling of the coil in the EM simulations and measured in-vitro results.

4.3 Results of human body model simulations and invivo measurements

The dielectric values of lung tissue were modified in order to simulate coil load changes in the inspiration and expiration states. From [105], permittivity and conductivity can be derived (Table 4). It can be observed that both the simulated and measured Q-values vary about 15% due to breathing (Table 10). Due to the higher conductivity in the deflated state, the losses on the coil are higher. This results in a lower Q-value and in a higher reflection coefficient (Fig. 4.2). The variability of the measured Q-value can be explained with inconsistent breathing of the subject. Since the Q-value change corresponds to the breathing state and torso movement, the reflection coefficient will behave conversely. Therefore, the reflected power values or reflection coefficients of the breathing signal were inverted in in-vivo experiments for better comparison with the respiratory belt.

	64MHz coil		128MHz coil	
	simulated	measured	simulated	measured
$Q_{inflated}$	79	77.9 ± 1.7	46	43.4 ± 2.6
$Q_{deflated}$	70	70.8 ± 1.9	39	40.3 ± 1.5
respiratory Q-ratio [%]	13	9 ± 3	15	7 ± 9

Table 10 – Simulated and measured coil parameters on breathing

The simulation of heart motion on the bases of conductivity variation was not conducted, because besides the conductivity changes by the blood volume, capacitive coupling effects of the heart displacement could further influence the signal. Although a direct simulation of the heart motion-induced Q-value variations was not performed, observations from Table 4 show that the ratio of the conductivity for blood is 1.78 times (for 64 MHz) and 1.63 times (for 128 MHz) higher than for heart muscle tissue. Between the end-diastolic motion state of the heart, in which the ventricles are filled with blood, and the end-systolic state, in which the heart is completely contracted and the blood volume in the heart is at the minimum, a

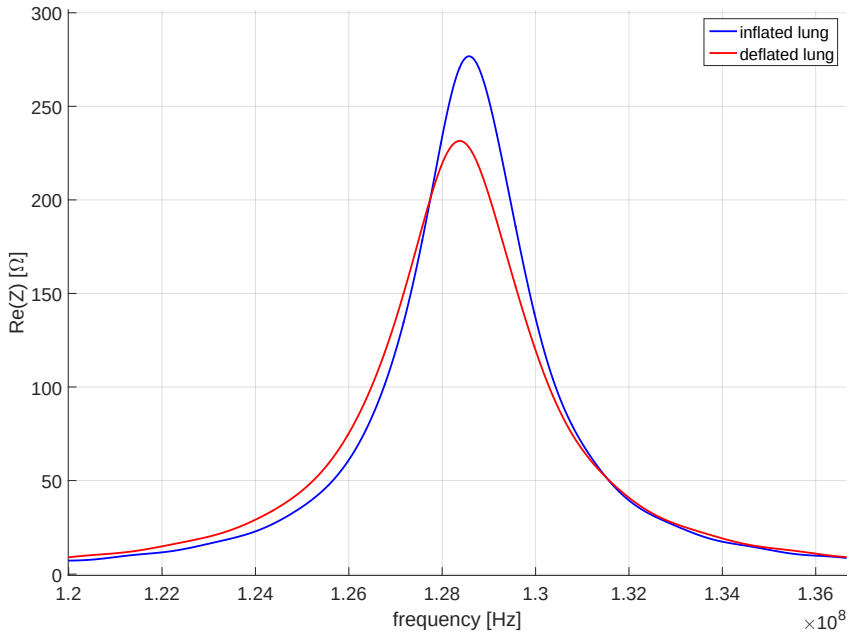

Figure 4.2 – Real value of the simulated coil impedance of deflated (red) and inflated lung (blue). Due to the higher conductivity, the Q-value is lower in the deflated state

significant change in the Q-value can be expected. In addition, the myocardial contraction could have an additional effect on these variations since the muscle moves away from the coil sensitivity region and increases losses by capacitive coupling.

4.4 Discussion

EM simulation helps to understand the complex behavior of the coil impedance and Q-value affected by physiological load changes. Analytic models can give a good approximation for homogeneous samples but are limited for human tissue, where various tissue types with different conductivities and border effects overlap.

A Q-value variation of 15% caused by breathing motion has been measured. This variation could have an effect on image quality in general and in signal-sensitive examinations like functional MRI (fMRI) or on quantitative measurements like B_1, T_1 or T_2 mapping. This is further addressed in Chapter 6.

In this simulation, the lung and heart tissue was separated from the human body model due to simulation time and memory restrictions. This does not reflect the true loading of the coil, but the abandoned tissue seems to make just a minor contribution to the relative coil loading variations, as shown in comparison with the measurement results.

The simulation fits well with the measured results and can reflect the impedance change on respiration. This breathing state simulation, however, is a simplified approach since only conductivity values have been modified. Organ displacement is not taken into account, which could lead to additional changes to the coil loading. However the sensitivity of loop coils is limited by their radius (see Section 2.1.4). Therefore depending on the position, a loop coil "sees" primarily the conductivity change in the lung rather than the motion of other organs.

A full analysis of the cardio-respiratory motion impedance variations would be possible by analyzing the full human torso at various motion states. This would involve a detailed motion model of the heart, diaphragm, lung, and neighboring organs. EM simulation software companies provide human body models with bulk body motion capabilities. These models are used e.g. for SAR calculations on multi-channel transmit systems. The complex contraction of the heart is not available yet and would need to be implemented by the user. This involves sufficient computing power and time, and could not be addressed in this work.

5

Motion induced load changes of volume coils

Coil losses on volume coils are mainly caused by stray capacitance effects of the sample or tissue inside the coils [103]. Hence, the assumption can made that, besides conductivity variations of tissue, bulk body motion affects the coils' impedance and Q-value synchronously to the motion magnitude. The up and down movement of the thorax during respiration has been shown to affect the Q-values of local and volume coils [76]. In volume coils, the change in distance of the object to the coil introduces variations in the capacitive coupling. Hence, motion-induced coil impedance changes lead to a detuning of the coil and wave reflection effects. This influences the transferred power during the excitation in MRI experiments. Typically, before the examination, the power is calibrated according to the loading of the patient. During the scan, the coil performance is influenced by the motion and, therefore, the transferred power of the excitation pulse varies. Here, we investigate these effects on the excitation pulses of an imaging sequence and their ability for retrospective motion correction with the GRICS algorithm (Section 5.1).

In Section 5.2, birdcage coils are studied in detail. Due to their design, they offer more resonance frequencies besides the imaging frequency; the so-called modes (see also Section 2.1.4). The effect of load changes on mode frequencies is thought to be a promising solution for a (semi-)continuous motion acquisition, independent from the transmission pulses.

The experiments and data analysis were conducted by myself, except for the GRICS reconstruction. The results of the experiments were published in two poster presentations at the Motion Correction Workshop of the International Society of Magnetic Resonance in Medicine (ISMRM) 2014 in Tromsø, Norway
[Kudielka et al., 2014a] [Kudielka et al., 2014b].

Furthermore the application of birdcage coil modes for motion capture was applied for patent and published in January 2016 [Kudielka et al., 2016a].

5.1 Reflected power of excitation pulses for respiration measurement

With the background of sample influence on coil loading, the question raises whether load variations would be detectable by power variations during imaging. This was addressed in the following section (5.1.1). Further investigations have shown the applicability of the power variation for respiratory motion tracking and retrospective correction with GRICS (Section 5.1.2).

5.1.1 Investigation of respiration influence on RF excitation power

To analyze the reflected power of the transmission pulse, the measurement setup, as described in Section 3.2.1, was realized on a HDxt MRI system. The forward and reflected power of the excitation pulse was integrated over the duration of this pulse (Fig. 5.1). The data of the respiratory belt and the reflected power of the body coil were recorded separately and merged in a MATLAB script retrospectively.

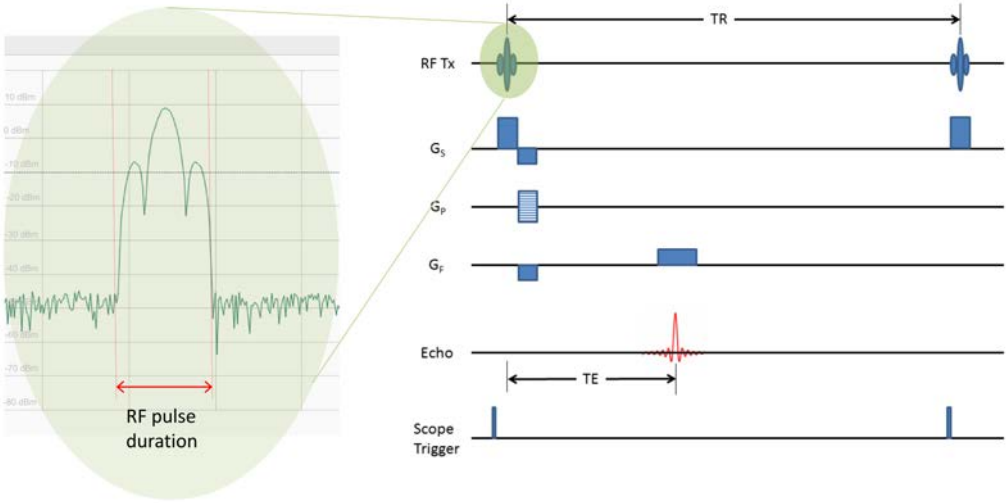

Figure 5.1 – Excitation pulse of a gradient echo pulse sequence. The measured power is integrated over the pulse duration.

In a first experiment, a healthy volunteer was placed inside the MRI system without any additional coil but with the respiratory belt fixed on to the chest. A FGRE localizer sequence was performed in "manual prescan" mode. This allowed a continuous looping of the sequence without image acquisition. Fig. 5.2 shows the coupled transmitted power (FWD, blue) and the coupled reflected power (REF, orange) of the body coil. While the transmitted power is stable, the reflected power shows regular variations. Both signals have a slight decreasing trend that is likely caused by losses due to the temperature increase of the transmit-chain components during the scan. Comparisons of the reflected power with the respiratory belt information correlate well and support the assumption that respiratory motion has an influence on the coil's tuning and transmission efficiency (Fig. 5.3).

Load-induced impedance changes in volume coils are caused by the whole volume inside the coil. Hence, even bulk patient motion could have an effect on the coil loading. This was investigated in another volunteer experiment on a MR750w MRI system with the same measurement setup. For that, the volunteer placed the arms over the head and was breathing normally. During the sequence looping, he was asked to move the arms down next to the torso. Fig. 5.4 shows the impact of the arms' movement. First, the respiratory variations are clearly detectable, with a breath-hold between t = 25-50 s. At t = 80 s, the volunteer moved his arms down, which resulted in a 4 dB drop of the reflected power and, hence, an improvement in

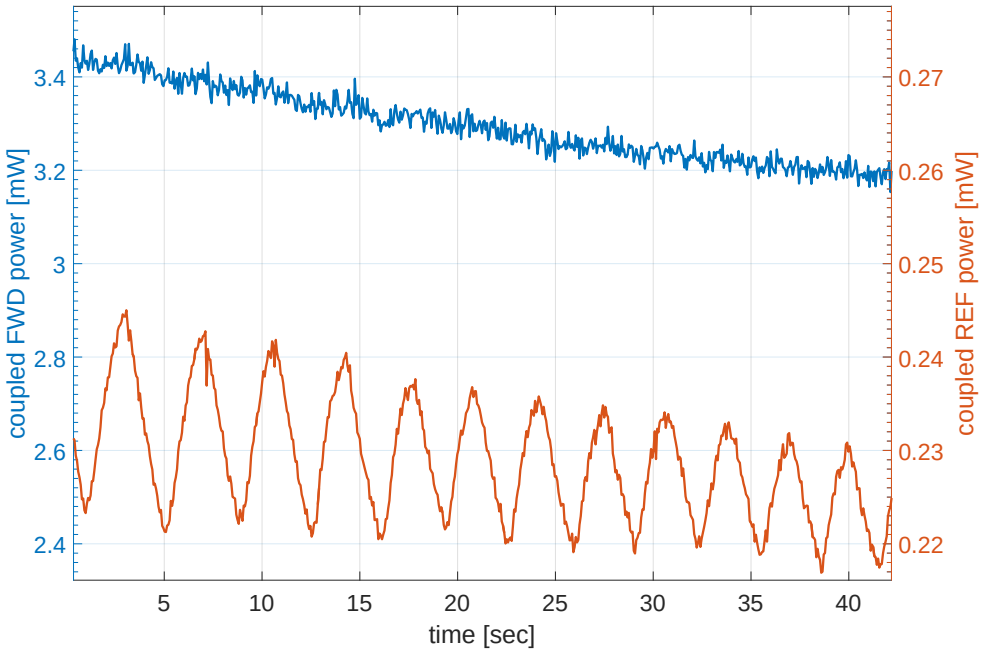

Figure 5.2 – Transmitted and reflected power of RF amplifier during sequence looping in free-breathing. Regular variations can be detected in the reflected power signal. blue: coupled transmitted power (FWD) of 3.2-3.4 mW; orange: coupled reflected (REF) power of 0.245-0.218 mW

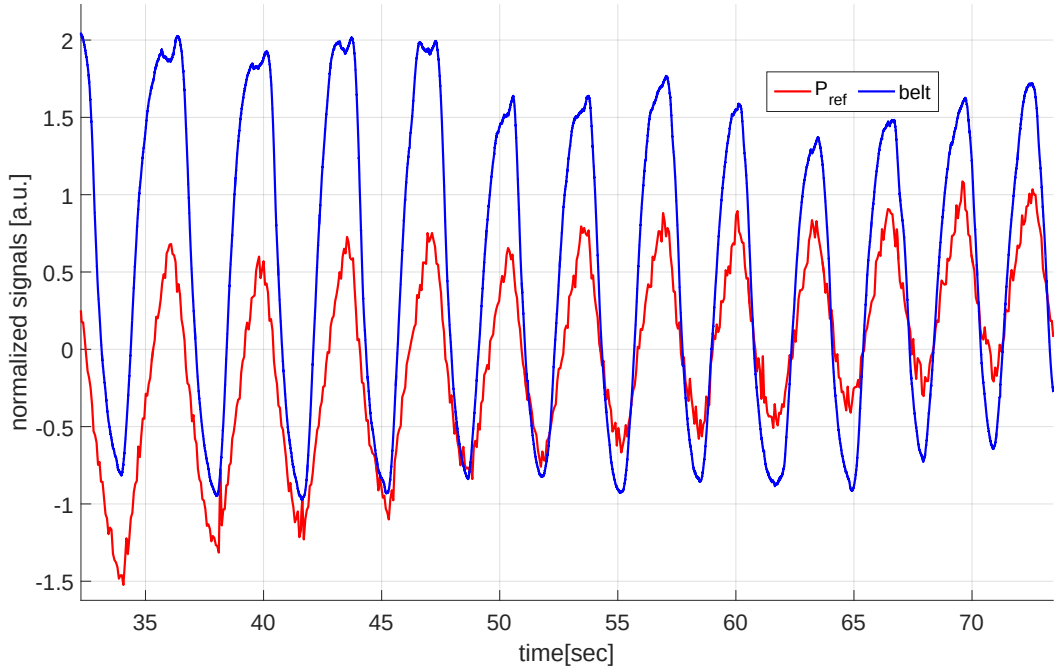

Figure 5.3 – Graphical comparison of reflected power of excitation pulse with respiratory belt

the tuning of the coil. This is contrary to the observation that a volume increase should impair the tuning and matching of the coil. However, during the pre-scan, the volunteer had his arms next to the body and the transmission power was calibrated to its optimum at this coil impedance state. While moving the arms over the head, the tuning was slightly mismatched, resulting in a higher reflected power.

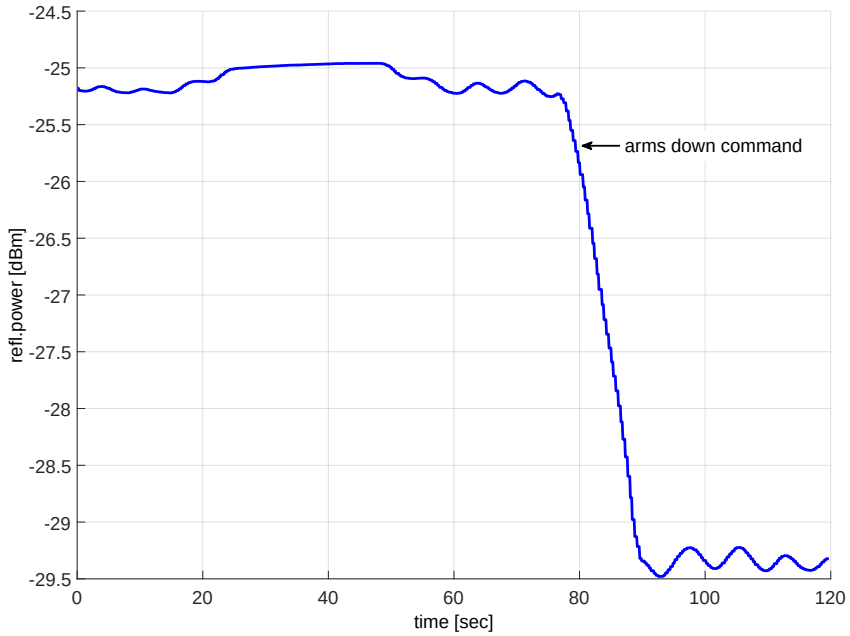

Figure 5.4 – Reflected power level change on arm motion during normal breathing; breath-hold between t=25...50 seconds

5.1.2 Application of reflected power information for motion correction

Since it was shown that reflected power variations from birdcage coils can represent breathing motion, a reflected transmit power recording during a free-breathing imaging sequence was utilized for a retrospective motion correction. A healthy subject was placed in the MR750w system and image data was acquired with an eight-channel torso coil. An FSE sequence (TR = 789 ms, TE = 47.5 ms, ETL = 8, FOV = 300 mm, Matrix 256x256) was performed in free-breathing and the reflected power of the first excitation pulse in each sequence was acquired with a power meter. A LabView application was normalizing and filtering the power values and forwarded the data via an RS232 protocol to the SAEC system (see also Section 3.2.2 for further details). The power of the excitation pulse was integrated over the pulse width of 3 ms. The synchronously recorded data of the respiratory belt and the reflected power was analyzed retrospectively with MATLAB. Thus, a good correlation between the respiratory belt and the reflected power could be observed (Fig. 5.5). The coefficient of determination was calculated as $R^2 = 0.80$. Since the power meter was triggered with the imaging sequence, the reflected power was measured once every TR. Hence, the sampling frequency results in $f_s = 1/TR = 1/0.789\ s = 1.26$ Hz. This is in good

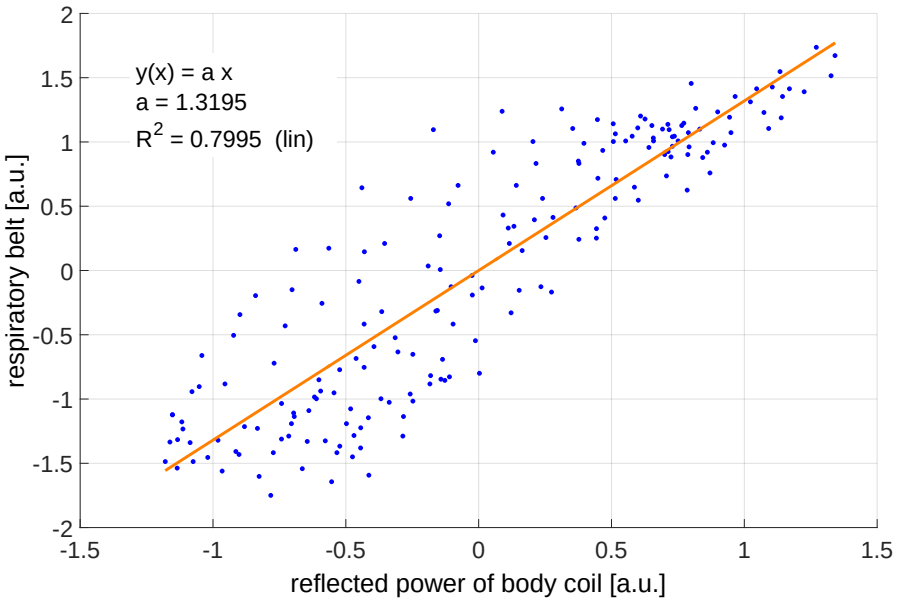

Figure 5.5 – Correlation of reflected power and pneumatic belt during free-breathing imaging

agreement with the Nyquist theorem, as the normal respiratory frequency is in the range of 0.1 Hz to 0.5 Hz. The power signal was used as a motion-state indication in the GRICS algorithm to correct for artifacts in the free-breathing image data. As shown in Fig. 5.6, the ghosting artifact can be reduced significantly with the reflected transmit pulse power signal.

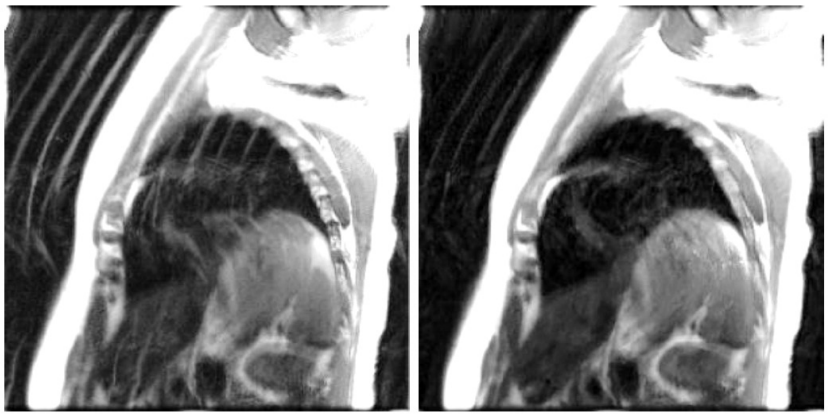

Figure 5.6 – Comparison of uncorrected (left) and GRICS corrected (right) free-breathing exam

5.2 Birdcage coil modes for motion detection

A main disadvantage of the method described before, is the dependence on the imaging sequence, which defines the sampling frequency and does not allow motion tracking before and after the sequence. A birdcage volume coil provides various resonant frequencies or modes (see Section 2.1.4). One solution for independent motion registration could be a separation in frequency. However since these modes come as side effects and are generally not tuned and matched, they provide a lower Q-value compared to the dedicated Larmor frequency of the coil. In a first approach, various modes were investigated with a moving phantom and on a volunteer (Section 5.2.1). The application of this method for motion detection during imaging was shown. Furthermore the influence of the mode currents was investigated by noise scans and a RF switch setup was implemented for imaging experiments. This allowed respiratory motion registration on mode frequencies of a birdcage head coil during image acquisition (Section 5.2.2).

5.2.1 Investigation of birdcage coil modes for motion detection

To analyze the capability for mode-based motion detection, the reflected power of a CW signal was measured on several modes of an inbuilt 3T body coil, while a $CuSO_4$ phantom was continuously moving inside this coil ± 100 mm from the isocenter in the Z-direction. For that measurement, the flexible power setup from Section 3.2.2 was used, in addition to a frequency multiplier and an amplifier (MiniCircuits, NY, USA) to generate a constant power at the coil of P_{FWD} = 10 mW at different frequencies. The setup was connected to the I-port of the birdcage coil, while the Q-port was terminated at 50 Ω. Fig. 5.7 shows the reflected power of the Larmor frequency (black) in comparison with the mode frequencies. A significant sensitivity has been observed on modes with higher Q-vales, such as at f = 235 MHz. In an in-vivo experiment, this frequency was chosen to measure respiratory motion with the volunteer placed inside the coil. For comparison, the information of the pneumatic belt was saved. Normal breathing and deep breathing events were detected with a correlation of R^2 = 0.73 between the mode-impedance change signal and the respiratory belt (Fig. 5.8).

The introduced power at a mode frequency causes a current flow in the endrings and rungs. Therefore it contributes to the noise level of the Larmor frequency, which could degrade image quality significantly. This effect is shown by noise scans on the 3T HDxt GRC MRI system. In noise scans the receiver signal is recorded without a prior excitation pulse and only noise of the entire receive path is acquired. By design, only the Larmor frequency is taken into account. The scans were performed with and without a CW-power level of 1 mW (0 dBm) at the harmonic mode of f=64 MHz. A 20-fold increase in noise level can be observed with the CW power on (Table 11). This effect was greatly reduced by adding a high-pass filter (BHP-100+, Mini Circuits) before the pre-amplifier with a pass-band frequency of 90-2000 MHz and a attenuation of 25 dB at 64 MHz. This shows that currents on the birdcage

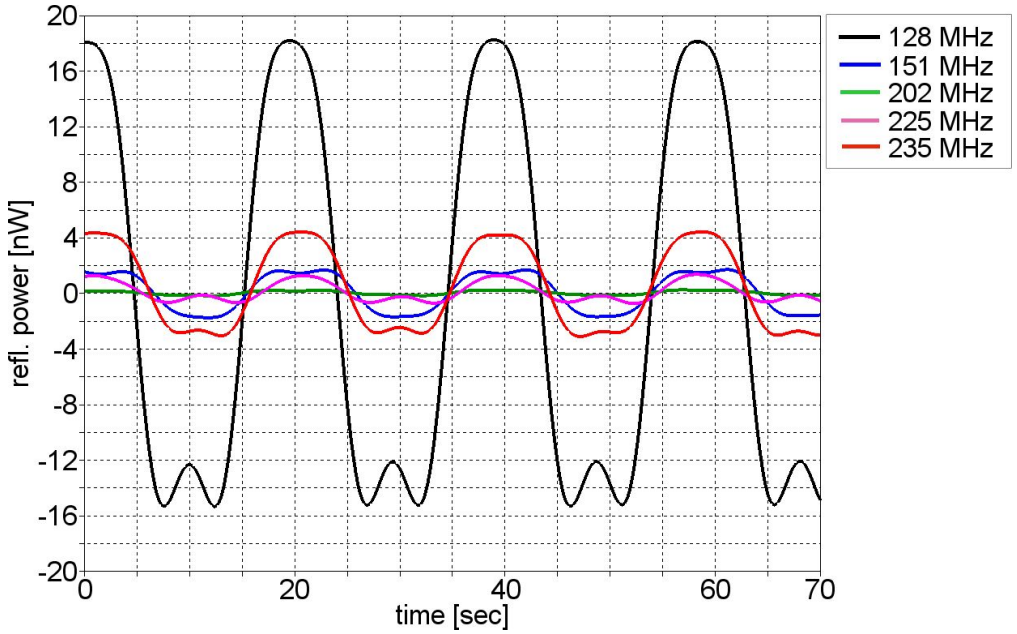

Figure 5.7 – Power variations on birdcage coil modes caused by a moving phantom

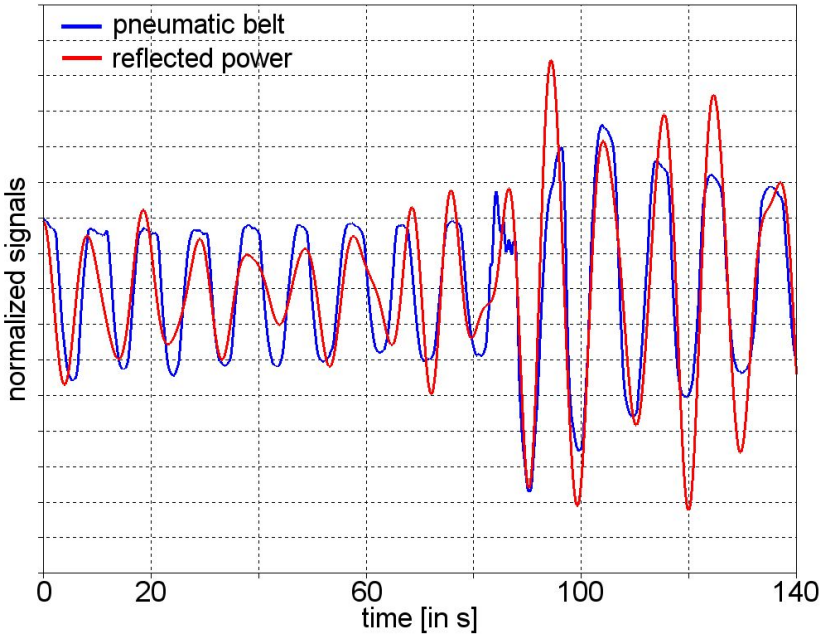

Figure 5.8 – Normal breathing and deep breathing effects on reflected power at the mode frequency f_H = 225MHz and pneumatic belt

coil at non-Larmor frequencies affect the noise level in imaging but can be reduced with accordant filtering.

Therefore, to utilize the motion detection on birdcage coil modes for MRI imaging, it has to be filtered out or deactivated during image acquisition. Similarly, the setup

[16bit pixel value]	mean±std	mean percentage
normal noise level	30.91 ± 19.10	100
with 0dBm power at mode	630.74 ± 385.21	2040
with high-pass filter	4.18 ± 2.75	14

Table 11 – Noise level comparison between normal conditions, with power on mode frequency (f = 64 MHz) and with BHP-100+ high pass filter (passband 90-2000MHz)

has to be separated during the excitation phase of the imaging sequence to avoid damage by the high power of the excitation pulse. One solution can be found in a switching logic, which alternately connects the coil to the RF paths of the MRI system and the RF setup of the motion detection system. A switching logic that performs these tasks is introduced in Section 3.2.3.1. Its functionality and the results of a volunteer scan are discussed in the following section.

5.2.2 Motion registration during MRI imaging

Long-ranging susceptibility effects affect the B_0 homogeneity in head imaging due to respiratory and cardiac motion (Section 1.3.1). In addition, the blood pulsation and torso movement are transferred toward the head and lead to involuntary displacement. In the following it is investigated, if a semi-continuous measurement of reflected power on a head birdcage coil mode can resolve physiological motion in the head during image acquisition. A healthy volunteer was lying on the patient table with the head padded inside the birdcage head coil. The switch and motion measurement setup were connected between the coil and its RF connector to the MR system (see Section 3.2.3.1). The pneumatic belt and PPG were placed on the volunteer for comparison. A gradient echo sequence with the following parameters was used:

- TR = 500ms
- TE = 20ms
- FA = 60 deg
- FOV=240mm
- Matrix 192x192
- NEX = 1

The motion acquisition switch was triggered by the MRI scope trigger signal. The activation of the switch was controlled with a TTL logic according to the TR and TE of the sequence. A trigger delay $T_d > TE$ was defined to ensure an "OFF" state of the motion measurement during the excitation pulse and image acquisition, and was set to $T_d = 40$ ms. Physiological motion information was acquired during the rest of the sequence for $T_p = 450$ ms. A safety window of 10 ms guaranteed that the

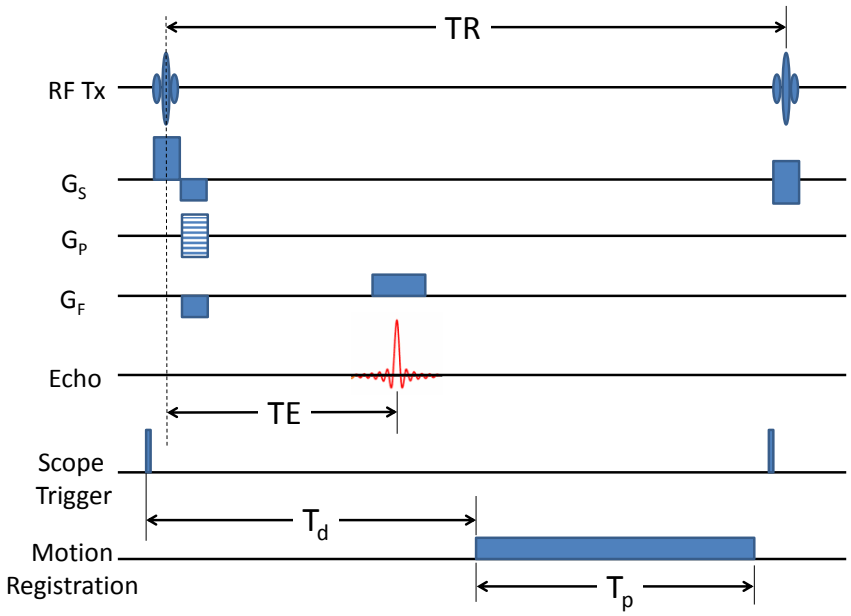

Figure 5.9 – Gradient echo sequence timing with switch activation; RF = RF excitation, G_S = slice selective gradient, G_P = phase encoding gradient, G_F = frequency encoding gradient, Echo = receive signal, TE = Echo time, Scope trigger = trigger pulse of MR system, T_d = trigger delay time, T_p = switch activation time

measurement setup was disconnected before the next excitation pulse (Fig. 5.10). The frequency for the motion detection setup was set to one mode of the birdcage coil head coil of f_m = 95 MHz. The data of the power sensor was sampled, filtered, and saved by the LabView application introduced in Section 3.3. Finally, the data of the respiratory belt, the PPG, and the power sensor were processed with MATLAB.

During imaging, a heart rate of 78 bpm and a respiration rate of 14 cycles/minute were recorded by the PPG and pneumatic belt. A FFT analysis of the acquired power signal shows two significant frequency components (Fig. 5.11). The first peak at f = 0.23 Hz corresponds to the respiration-induced head motion (f = 14 cycles/60 s = 0.233 Hz). The retrospectively filtered signal provided was well-correlated with the pneumatic belt (R^2 = 0.81). The second peak of the FFT describes the switching frequency of f = 2 Hz (total switch time = T_p + T_d + 10 ms = 500 ms). The "OFF" state gap of 50 ms at each MRI sequence had no significant effect on the recorded data, as the sampling duration was 42 ms due to the power sensor sampling time. Also, a frequency component that represents the PPG signal at f = 1.3 Hz is observable; however, its amplitude is not significantly prominent. Furthermore frequencies of f < 0.1 Hz have a significant contribution in the FFT. This can be explained with magnitude variations throughout the measurement.

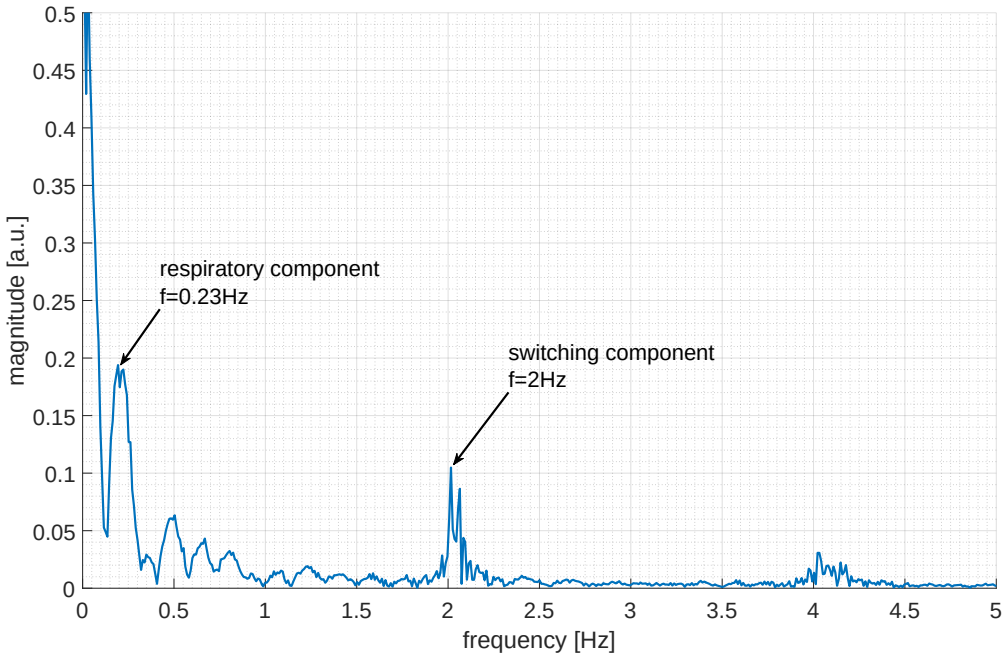

Figure 5.10 – FFT of power signal of mode frequency; f=0.23Hz corresponds to respiration frequency of 14cylces/minute; f=2Hz reflects switching frequency

5.3 Discussion

Observations on the reflected power of the excitation pulse give a good indication for the respiratory motion in volume coils. The measurement setup is relatively easy to implement, and might be achievable with the components of the MRI system itself - e.g. with the power monitoring or RF signal receiver. To link the acquired power data to respiratory motion, one must assume that the patient lies still on the patient table and is not moving. This assumption is usually true for cardiac imaging, when a multi-channel torso coil is placed and strapped on the patient. Other patient movement is usually not periodic and could be filtered out with dedicated algorithms. The dependence of the sampling rate on the scope trigger and, hence, the TR time, limits this method to the detection of slow respiratory motion only. Especially in sequences with various excitation pulses, such as FSE, information regarding additional RF pulses could increase the sampling frequency. This would require a trigger for the power sensor at every RF pulse.

A synchronized but separated image acquisition and motion registration could be advantageous and is shown by the utilization of birdcage coil modes to capture impedance change effects due to motion. Semi-continuous motion detection with a TR-independent sampling rate is feasible. But one must keep in mind that some RF power needs to be applied continuously to the coil in order to measure the motion-induced impedance change. The power level can be small (here in mW range) but it could have an effect on the image noise. Filtering or controlled switching needs to be applied, which would allow semi-simultaneous motion measurement and imaging at the Larmor frequency. Switching setups are limited by their settling duration and might fail in fast imaging methods. Dedicated filtering and activation of the motion measurement system might be preferable for such sequences. To improve sensitivity, different coil designs could be taken into account. Double-tuned birdcage coils provide a quadrature architecture at two different frequencies and deliver two signals by accordant filters.

Utilizing the power information of the volume coil depicts a potential solution for sensor-less and contactless motion detection. However, due to their design, a localization of the motion is not possible. This is addressed in the next chapter, where the behavior of surface loop coils on motion-induced impedance changes is investigated.

6 Measurement of load changes on local coils

A localization of the source of an impedance change with volume coils is not possible because the load impedance represents the whole volume inside the coil. However, coils with a heterogeneous magnetic field distribution are loaded just by objects in their field of sensitivity. In MRI, such coils can typically be found in receive-only coils from single one-channel loop coils to multi-channel phased-array coils.

In the following experiments, multiple regions on the human body were analyzed for impedance change behavior with a small single-loop coil (Section 6.1). It is shown that cardio-physiologic motion can be derived but it cannot be directly compared to the ECG or PPG signals. While an ECG represents electrical activity and a PPG the peripheral blood flow, coil load variations are caused by mechanical heart motion and blood pool variations. Based on that, a volunteer study in a clinical setup was performed to acquire motion information during cardiac Cine imaging in free-breathing with a 31P loop coil. The acquired motion information was used to retrospectively correct for respiratory artifacts the GRICS algorithm and to compare it to cardio-physiologic data extracted from the Cine images (Section 6.2). Finally, the analysis of reflection and transmission coefficients of a four-channel coil is showing the potential of multi-channel motion acquisition, compared to single-coil measurements (Section 6.3).

The experiments and data analysis described in Section 6.1 and Section 6.3 were executed fully by myself. For the volunteer study of Section 6.2, I have received support during the image examinations by Dr. Pierre-André Vuissoz and Dr. Freddy Odille, as the LabView software, the SAEC and the image acquisition had to be controlled at the same time. Furthermore, the GRICS reconstruction for this experiment was performed by Dr. Freddy Odille from IADI. The results of these experiments were submitted for paper publication [Kudielka et al., 2016b].

6.1 Load changes of surface coils at several body positions

The 75 mm-loop coil in the 64 MHz and 128 MHz configuration (Section 3.5) were used in this lab bench experiment. The data of the coils was acquired and filtered with a dedicated LabView application, and all signals were transferred to the SAEC system. The setup and software are described in detail in Sections 3.2.2 and 3.3.2. The data of six healthy volunteers (3 male, 3 female, age 27-36) was acquired. Each volunteer was lying on the patient table during the whole experiment, while the ECG, PPG, and respiratory belt signals of the HDxt GRC MRI system were recorded for

comparison. Fig. 6.1 shows the five different coil positions where data was acquired. These are

1. the lower end of the sternum
2. the area outwards the left clavicle
3. the right popliteal fossa
4. the right subtalar joint lateral
5. the left scapula

The measurement time on each position was four minutes with the coil fixed on the particular position with a Velcro strip. Subsequently, the recorded SAEC data was analyzed with MATLAB.

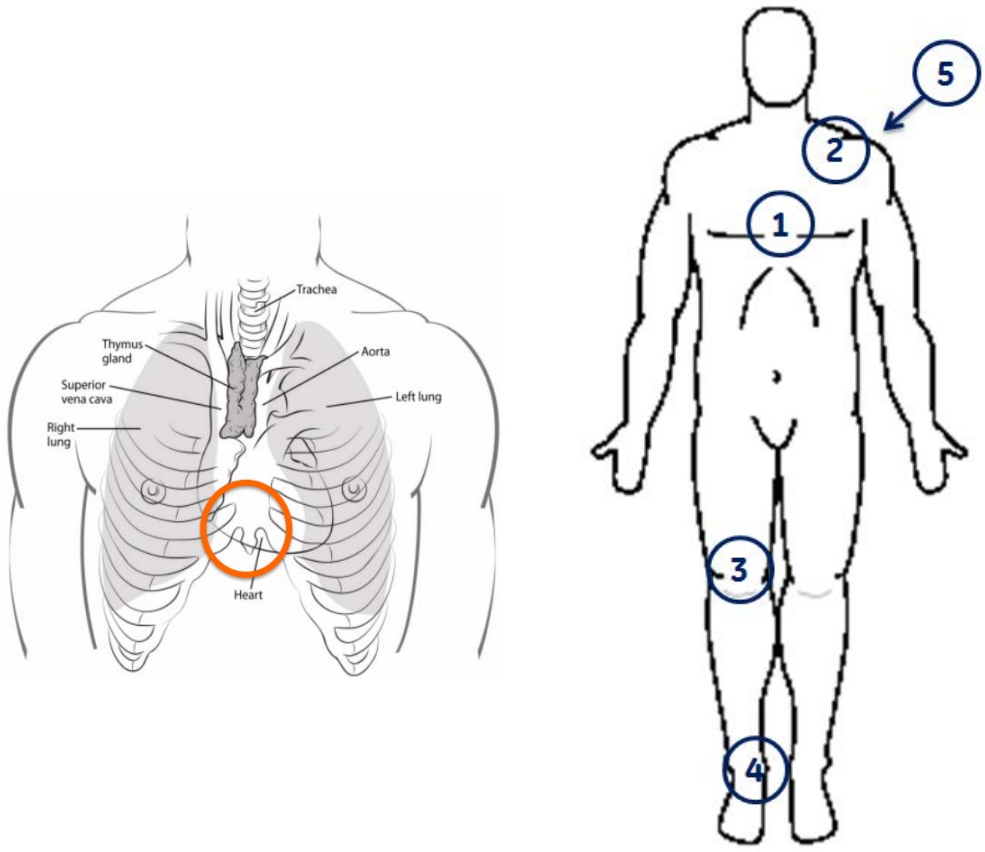

(a) Position 1 of loop coil on the chest

(b) Positions of loop coil for physiologic data acquistion

Figure 6.1 – Position 1 to 5 for physiological data acquisition at different body areas

6.1.1 Respiratory motion detection

Fig. 6.2 shows the variation of Q-values at the different coil positions after respiratory filtering. Respiratory motion can be observed in the torso region only (Positions 1, 2, and 5). Positions 3 and 4 did not have any specific signal features in the frequency range up to 0.3 Hz. The Q-ratios in Position 1 correspond to the simulated values of 0.13 and 0.15 (see Table 10 in Section 4.3). The signal at Positions 2 and 5 is significantly smaller but has a good correlation with the pneumatic belt data.

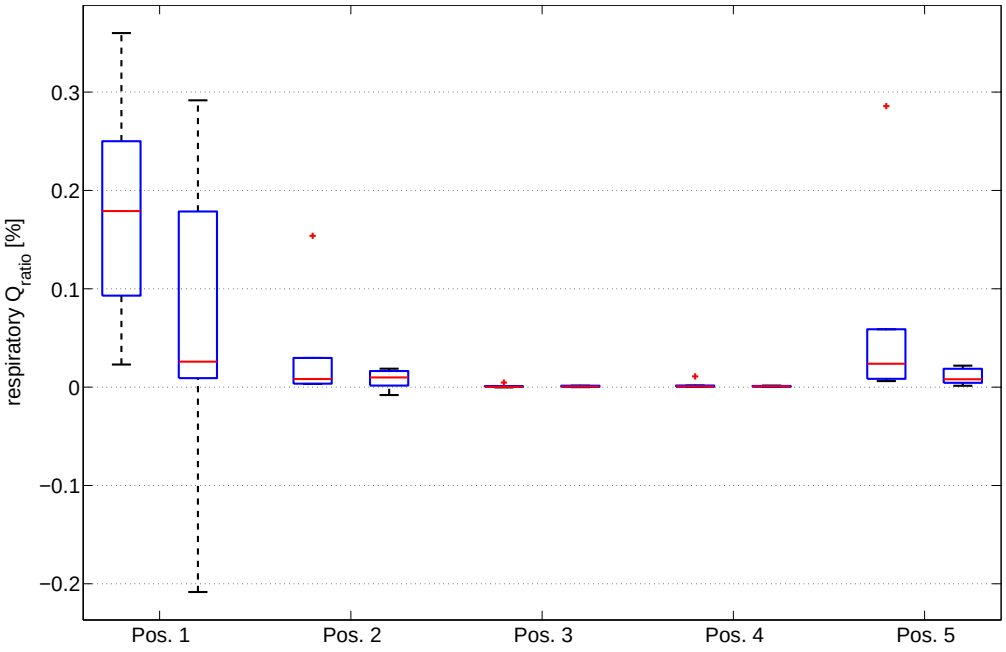

Figure 6.2 – Q-ratios for respiratory filtered signal on six volunteers at different positions; left bar: results of 64 MHz coil, right bar: results of 128 MHz coil

6.1.2 Arterial pulse flow detection

Positions 2, 3, and 4 were chosen due to the surface near arteries in these regions: the subclavian artery, the popliteal artery, and the medial malleolus artery respectively. The filtered impedance-change profiles should reflect a composition of the blood volume change and arterial wall motion at this position. To confirm this hypothesis, a coil was placed on the wrist of one volunteer with the PPG sensor on the same hand (Fig. 6.3a). Since the PPG signal represents arterial flow, a comparison of the coil signal and PPG in close proximity should be equal in shape. A slight super-extension of the wrist improved the coil signal and it can be shown that the filtered coil signal corresponded well to the PPG signal (Fig. 6.3b).

Comparing the temporal progress of the pulse curves, one can observe a position-dependent delay between the ECG signal and the coil data. From these delays, the pulse transit times (PTT) and pulse wave velocity (PWV) were calculated. The

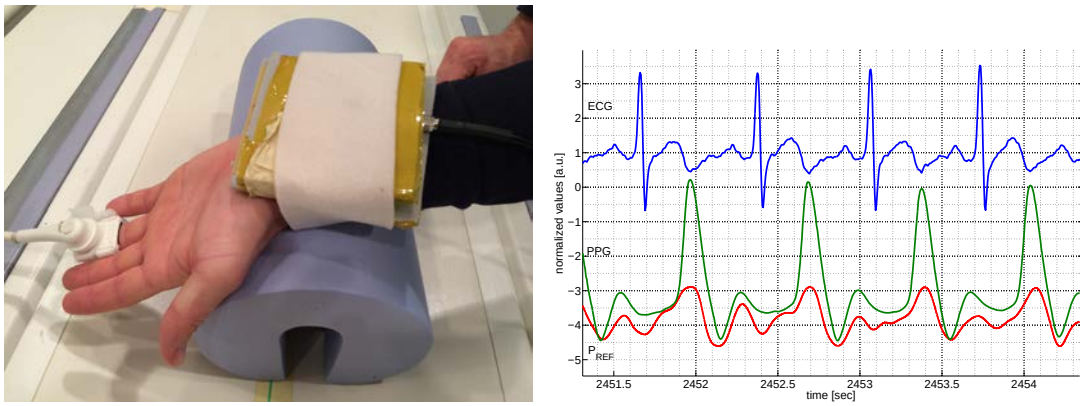

(a) Coil position on the wrist with PPG sensor (b) Signal of reflected power variations on the wrist

Figure 6.3 – a) Measurement setup on the wrist, b) Signal of reflected power variations on the wrist (red) compared to ECG (blue) and PPG (green). The coil load change clearly corresponds to the blood pulse variations shown by the PPG signal

distances between the sternum and Position 2 (d1), between the sternum and Position 3 (d2), and between Positions 3 and 4 (d3) were measured on each volunteer (Fig. 6.4). For the definition of the temporal points, the usage of the flow peak would be the most obvious method, although it is not recommended since flow reflection could lead to temporal peak shifts [127]. One state-of-the-art method that was used here is the "maximal upstroke algorithm" [128]. It refers to the maximum of the first derivative of the flow curve during systole. The coil data of the 128 MHz coil at the various positions was superimposed for each R-R interval. The maximum of the first derivative a_{max} of each superimposed curve was determined (Fig. 6.4). The flow duration between the subclavican artery and the popliteal artery was defined as t_{p2}, and between the popliteal artery and the medial malleolus artery as t_{p3}. The PWVs for the body and leg were calculated by

$$PWV_{body} = \frac{d_2 - d_1}{t_{p2}} \tag{6.1}$$

and

$$PWV_{leg} = \frac{d_3 - d_2}{t_{p3}} \tag{6.2}$$

Table 12 shows the calculated PWV for body and leg for all volunteers. Normal values according to literature [29, 129] are given in the last column and show a good correlation of the measured data.

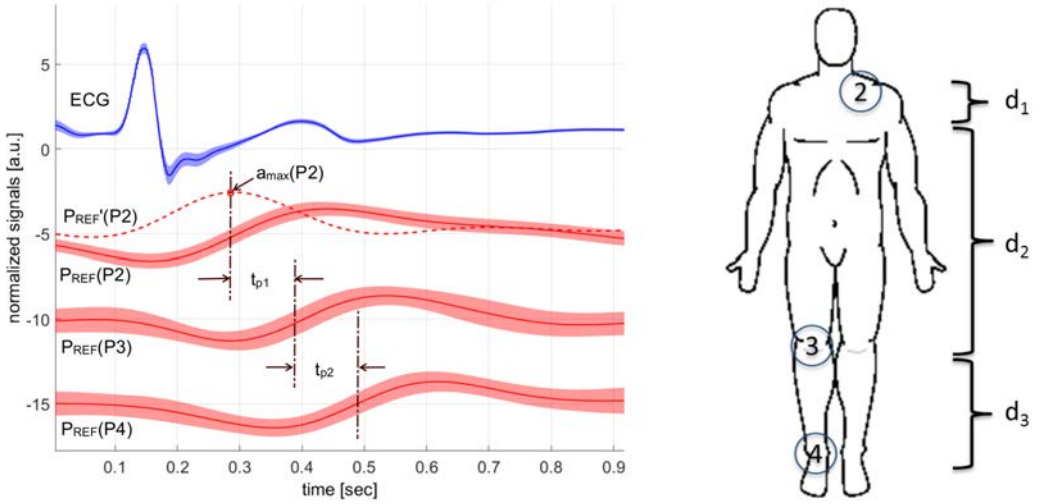

Figure 6.4 – Time points and distances for PWV calculations. left: time points definitions is performed by evaluating the maximum of the first derivative a_{max}, shown here for the curve on position 2 (P_{REF}(P2); right: distances between measurement positions, see text for detailed explanation

PWV [m/s]	vol.#1	vol.#2	vol.#3	vol.#4	vol.#5	vol.#6	lit.
PWV_{body}	6.8	5.8	5.8	5.1	7.1	7.35	6.2 (4.7-7.6)
PWV_{leg}	9.4	13.1	11.1	9.7	12.5	8.9	10 (8-12)

Table 12 – Pulse wave velocities calculated from coil power reflections on six volunteers; Literature values out of [29] and [129]; mean values and minima and maxima in brackets are given

6.1.3 Heart motion representation

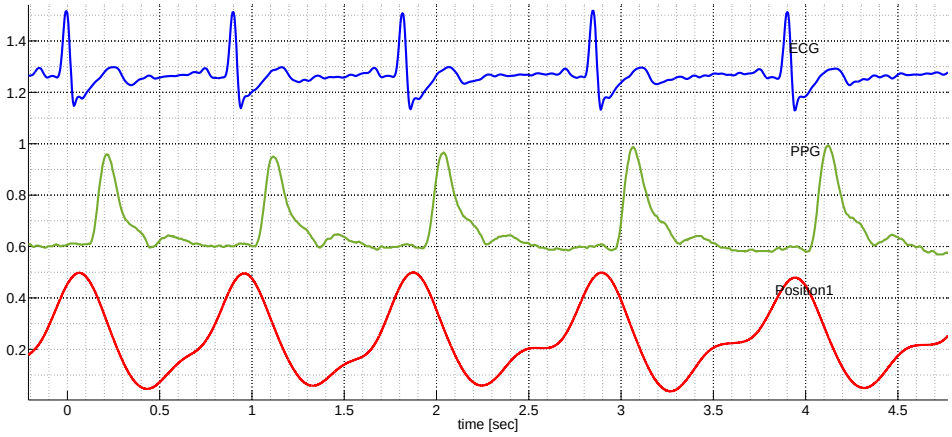

Figure 6.5 – Bandpass-filtered signal on position 1 in comparison with ECG and PPG

The band-pass-filtered signal on Position 1 represented repetitive patterns in correlation with ECG and PPG (Fig. 6.5). Since a direct comparison between the coil signal and the physiological sensors could not be made, myocardial volume variations were simulated and compared with the measurement results. The MATLAB script CircAdapt [130] provides a comprehensive analysis of cardio-physiologic volumes, flow, and muscle fiber contraction on the basis of initial start conditions for heart rate, pressure, flow, and activity. Cardio-physiologic parameters, like left ventricular volume, left atrial volume, aortic flow, and pulmonary artery flow were simulated with this software according to the measured heart rate of the volunteer. The 'MakeParDefault' function of CircAdapt was used to calculate the physiological values iteratively until steady conditions with minimized error. Quantitative results were not taken into account but the signal shape of the measured and simulated data was compared qualitatively. Fig. 6.6 shows an example of the normalized signal of these simulated parameters (green) in comparison with the measured coil signal (red), and the ECG and PPG signals (blue) of one volunteer.

It can be observed that the filtered reflected power variations correlate to the left ventricular volume course (Fig. 6.7). This can be explained with the blood volume change and the aligned change in conductivity during the heart cycle, which seems to contribute most to the resultant impedance changes (see also Section 4.3). Impedance variations by the heart muscle motion, aortic flow or pulmonary artery flow might overlap but are thought to have a minor contribution.

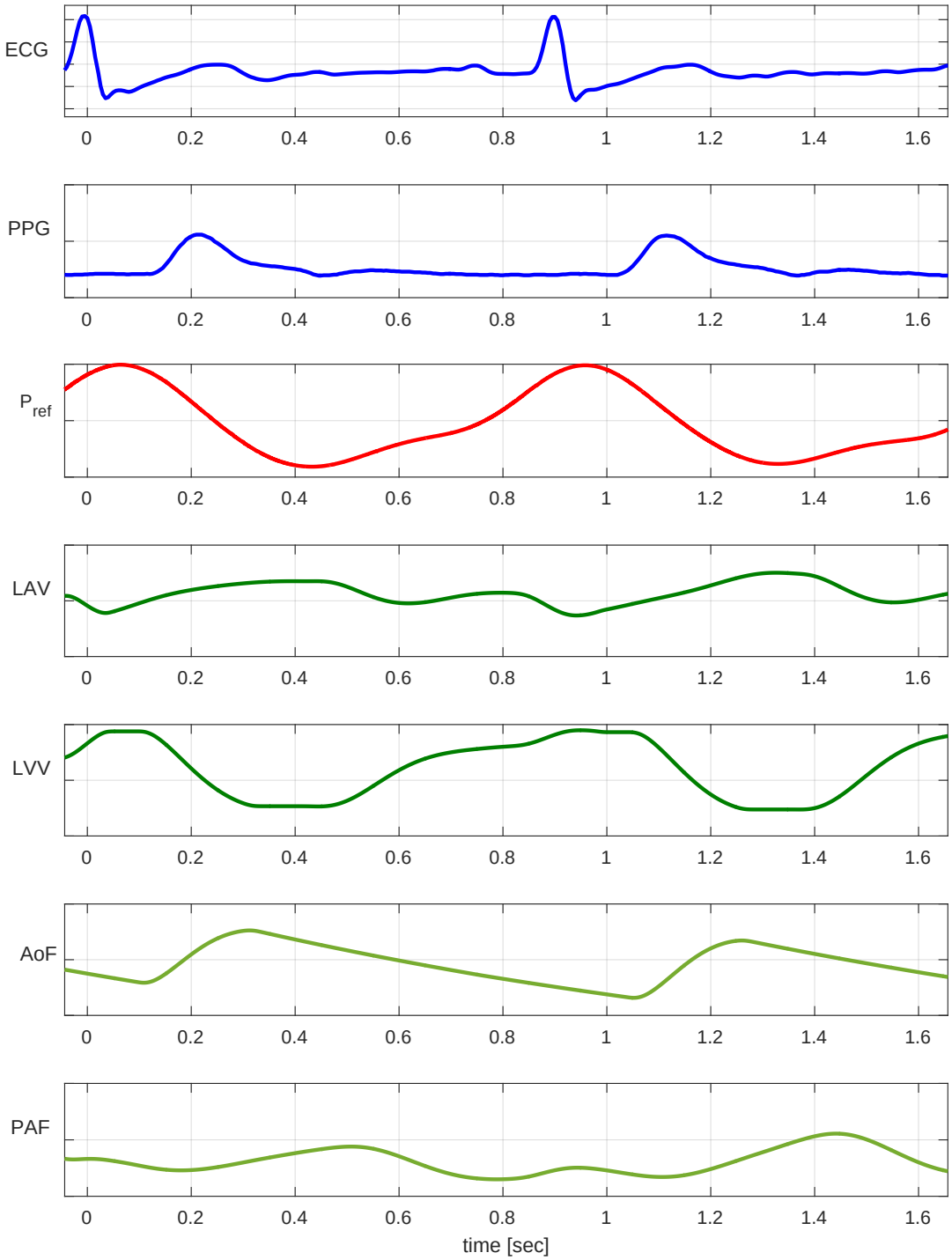

Figure 6.6 – Comparison of experimental results with simulated data of CircAdapt. ECG = electocardiogram of MRI system, PPG = pulseplethysmograph of MRI system, P_{ref} = measured reflected power of coil, LVV = left ventricular volume, LAV = left atrial volume, AoF = aortic flow, PAF = pulmunary artery flow. y-axis values normalized in arbitrary units

Table 13 gives the coefficient of determination R^2 of the fit of the superimposed coil signal at Position 1 with the simulated left ventricular volume. A value of R^2 = 0.55 to 0.92 was observed for the 64 MHz coil and R^2 = 0.45 to 0.91 for the 128 MHz coil. Variations in the goodness of the fit are versatile and could be caused by coil positions and the resulting contributions of different signal sources. In addition, the simulation might not reflect the real volume variation. Therefore, a detailed comparison between Cine images, the segmented left ventricular volume, and the coil impedance information was performed in a clinical evaluation (see Section 6.2).

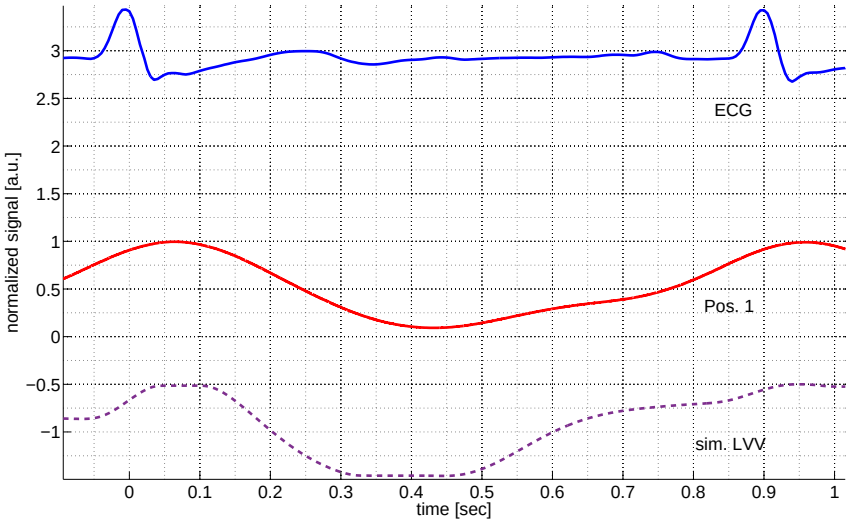

Figure 6.7 – 1RR section with simulated left ventricular volume, ECG and band-pass filtered coil data at position 1

		vol.#1	vol.#2	vol.#3	vol.#4	vol.#5	vol.#6
64 MHz	R^2	0.91	0.55	0.92	0.76	0.92	0.86
	mean HR	59.2	45.9	55.9	57.3	50.2	59.7
	number RR intervals	310	250	173	351	229	309
128 MHz	R^2	0.9	0.45	0.89	0.78	0.83	0.91
	mean HR	60.0	45.7	59.8	55.9	49.8	60.4
	number RR intervals	365	193	250	349	383	300

Table 13 – Heart motion analysis on six volunteers for the 64MHz coil and 128MHz coil; R^2 of the coil signal to the simulated LV volume, the mean heart rate (HR) and the number of analyzed R-R intervals is given

6.2 Local acquisition of load changes as a motion indicator during Cine imaging

A clinical evaluation of the coil load measurements was performed on the 3T HDxt system in the CHRU Nancy. The aim was to show the ability of a localized loop coil as a simultaneous motion detection of both respiratory and cardiac displacement at the same time during image acquisition. To understand the observed signals and prove a physiological reason, a comparison with a left ventricular volume contraction from Cine images was applied. The motion tracking setup described in chapter 3.2.3.2 was utilized.

6.2.1 Clinical volunteer setup and data analysis methods

Figure 6.8 – Setup of loop coil measurement. Coil fixation is removed for visualization. ECG, respiratory belts at the chest and at the abdomen are used for this measurement

Five healthy volunteers (one male, four female; age: 28-32 years) were examined in a 3T HDxt MRI system. The images were acquired with the transmit-receive body coil. An ECG and two respiratory belts of an external Maglife patient monitor were used as reference (Fig. 6.8). For simultaneous coil load measurement, a ^{31}P single-loop coil was placed at the sternum of the volunteer. Short-axis Cine images were recorded in breath-hold. The whole heart was covered in 14 to 16 slices. In addition, the Cine images of one slice were acquired, while the volunteers breathed normally.

The acquired data was processed and filtered with MATLAB (see also Section 3.3.2). Free-breathing data was retrospectively corrected with the GRICS algorithm. The reconstruction was performed based on the data of the two pneumatic belts and

the coil loading, respectively. For quality assessment, the image entropies [125] of the uncorrected and corrected images obtained in all cardiac phases were calculated and compared.

Typical parameters of the myocardial function, namely, the end-diastolic volume (EDV), end-systolic volume (ESV), ejection fraction (EF) of the left and right ventricle as well as end-systolic time (ES) and end-diastolic times (ED) were evaluated by a cardiologist using the MASS research software (V2013-EXP, Medis, Leiden, Netherlands). The determined values were used as a baseline for semi-automatic left ventricular volume segmentation (Cardiac Vx, GE Healthcare, Waukesha, WI, USA).

6.2.2 Retrospective respiratory motion correction

The filtered respiratory data shows good correlation (R^2=0,89-0,99) with the pneumatic belts for all volunteers. Outliers were particularly observed in the correlations for volunteers 3 and 4 in the abdominal belt (Fig. 6.9). As explained in chapter 1.3.2 this is caused by patient individual breathing patterns. The movement between the abdominal area and the chest can be decoupled as shown in Fig.6.10.

Fig. 6.11 illustrates reconstructed images without correction, with correction using the belt data and with correction using the coil data. The entropy of the corrected free-breathing Cine images was 0.62% - 3.93% higher than those of the uncorrected images. A higher entropy implies reduction of blurring and sharpening of the edges by the GRICS reconstruction algorithm. The entropy improvement of the corrected images was observed to be constant over all the cardiac phases (Fig. 6.12). Over all the cardiac phases, there was no significant difference between the entropy change achieved by reconstruction using the reflection factor data ($p = 0.9976$) relative to that achieved using the respiratory belt data. It was confirmed for all the volunteers that the reflection factor could be used as a motion indicator for the application of the GRICS reconstruction algorithm (Table 14).

	uncorrected	corrected with belt data	corrected with S11 data
Volunteer 1	933,82	939,64 (0,62%)	940,34 (0,70%)
Volunteer 2	750,42	767,4 (2,26%)	767,05 (2,21%)
Volunteer 3	833,75	843,6 (1,18%)	843,2 (1,14%)
Volunteer 4	954,15	991,6 (3,92%)	990,22 (3,77%)
Volunteer 5	898,23	924,87 (2,97%)	925,5 (3,04%)

Table 14 – Mean image entropy over all cardiac cycles of uncorrected images, belt corrected images and coil corrected images. Values in brackets are percentage increase of corrected to uncorrected image entropy

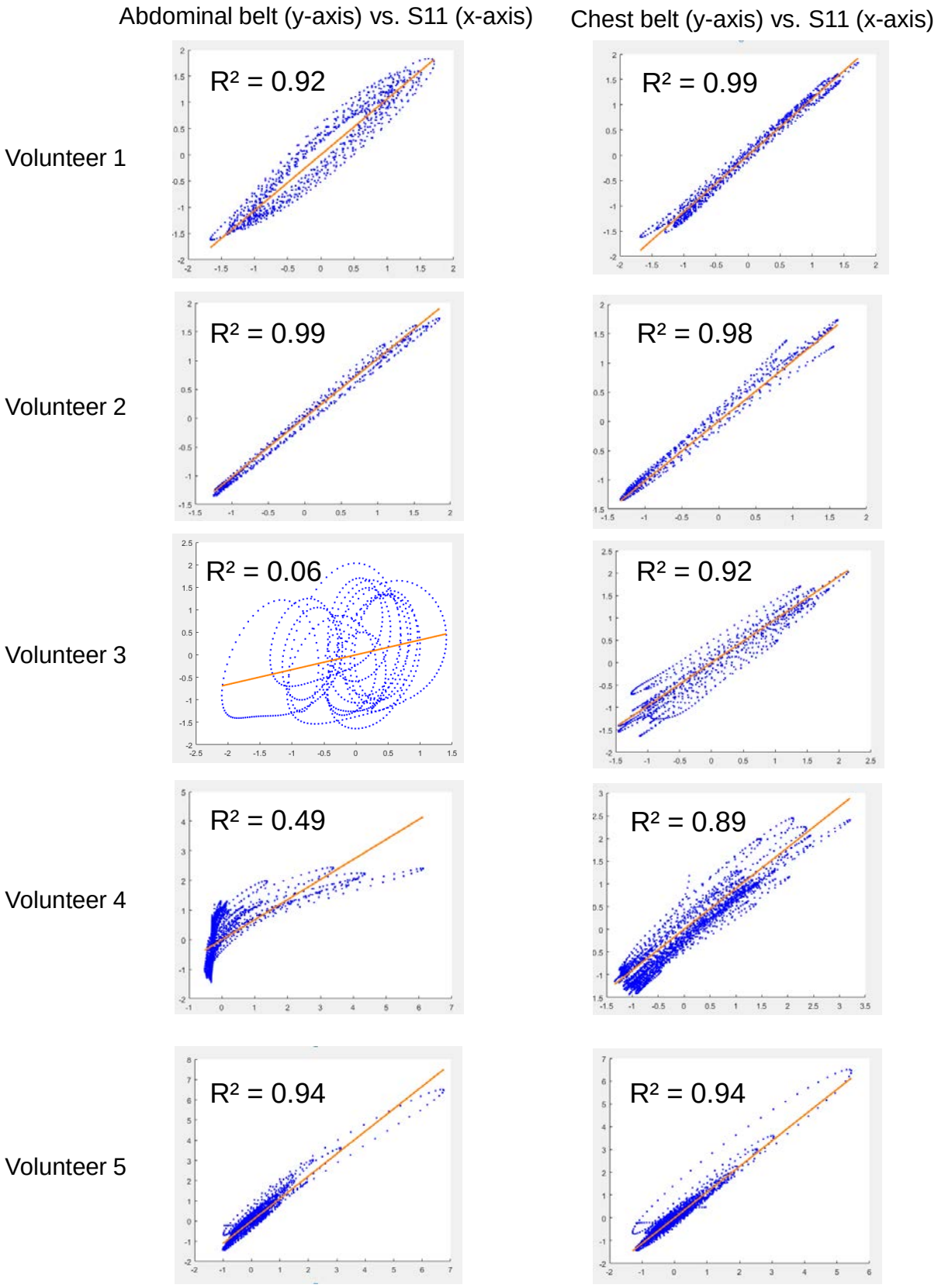

Figure 6.9 – Correlation between the coil S11 data and the abdominal belt signal (left), and between the coil S11 data and the chest belt signal (right), for each volunteer

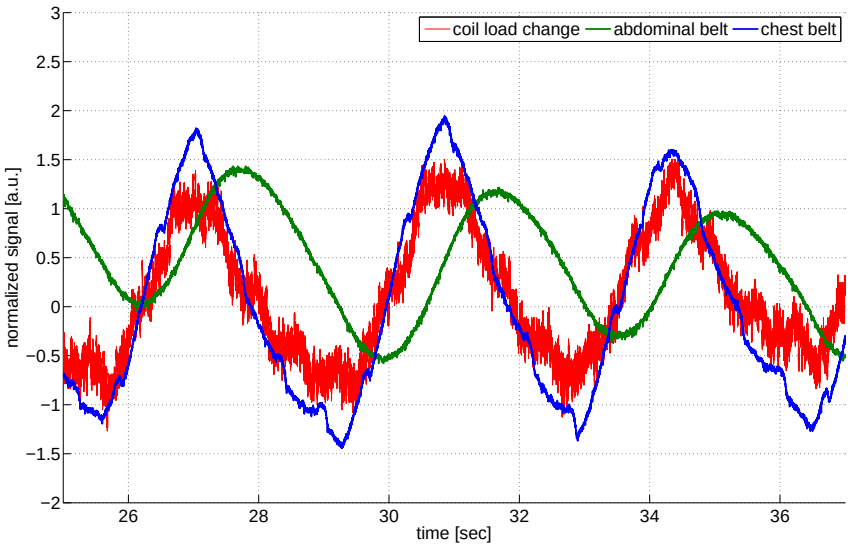

Figure 6.10 – Comparison of raw S11-data (red), the chest belt (blue) and the abdominal belt (green) on volunteer 3 with an atypical breathing pattern

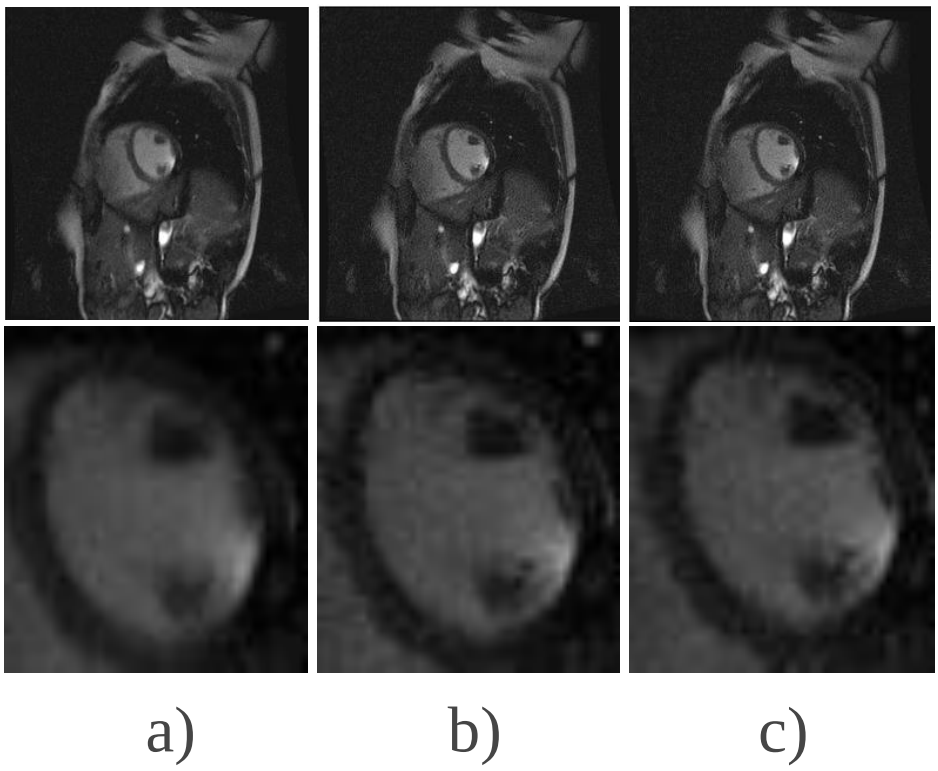

Figure 6.11 – Top row: Short axis images of a free-breathing Cine acquisition in volunteer 5. Uncorrected (left), motion correction with belt (middle) and motion correction with S11 data (right). bottom row: zoomed area of left ventricle: an increase in sharpness can be detected in the GRICS corrected images

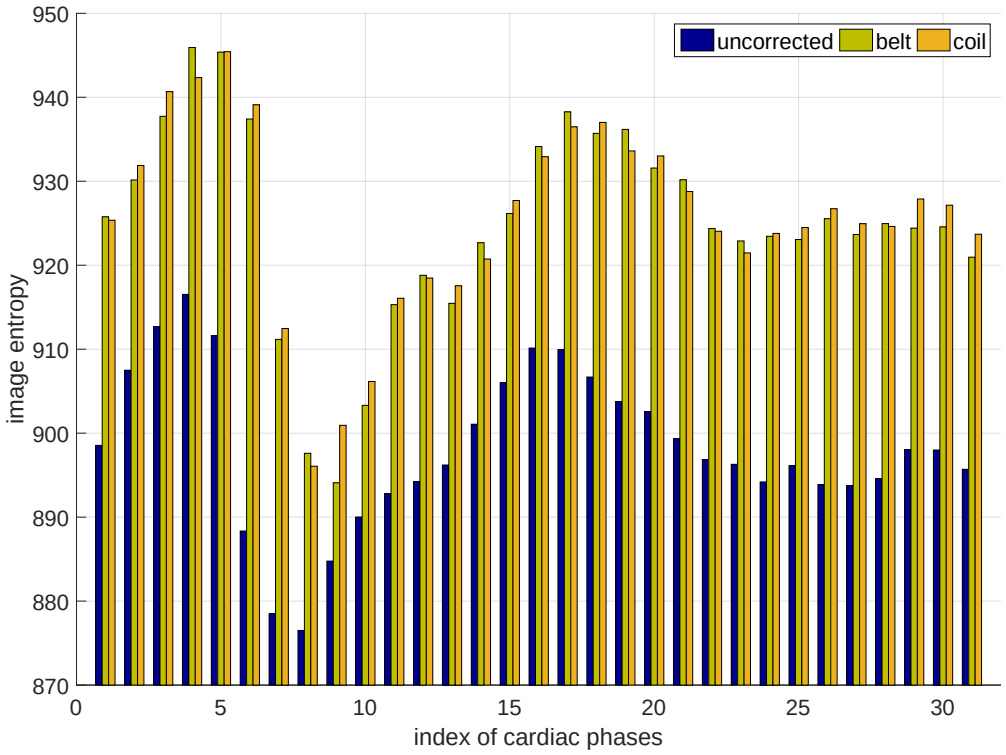

Figure 6.12 – Image entropy over 31 cardiac phases. Entropy of uncorrected (blue), belt corrected (green) and S11 corrected (orange) of volunteer 5

6.2.3 Coil load data compared to left ventricular volume variations

The higher frequency components of the reflection signal presented a repeating pattern in correlation with ECG. Fig. 6.13 shows the superimposed reflection factor data and ECG data of 130 R-R intervals for the four volunteers. A clear profile in the superimposed reflection data can be observed, whereas a signal notch occurs at the end-systolic time followed by a plateau until the end-diastolic time. Both data sets show a higher standard deviation towards the end due to R-R length variations. The correlation of the mean of the superimposed reflection data with the left-ventricular volume variation has been calculated as R^2 = 0,52- 0,78 (Fig. 6.14). The low

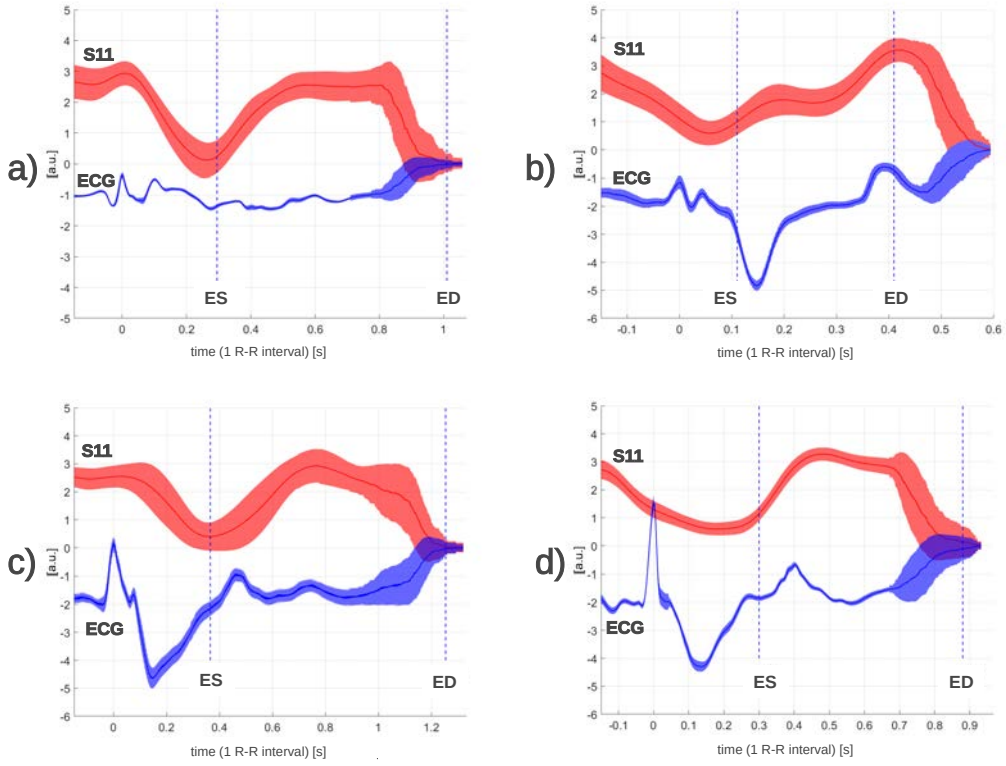

Figure 6.13 – Superimposed ECG (blue) and S11 (red) data for one R-R interval. The width of each curve represents the standard deviation, and the thin line the mean value. The data for a) volunteer 2, b) volunteer 3, c) volunteer 4, and d) volunteer 5 are shown. ES and ED respectively denote the end-systolic and end-diastolic time points determined from the Cine images.

correlation could be caused by the position and size of the coil. The effective coil area detects additional impedance variations from atrial or aortic blood flow, which is overlapped to the ventricular blood volume and increases the imperfections in the variation of the coil load.

Because the variation of the coil loading is correlated with the left ventricular volume of each cardiac cycle, this motion information may be used for cardiac triggering. A simple peak detection algorithm was applied to the ECG and S11 signals

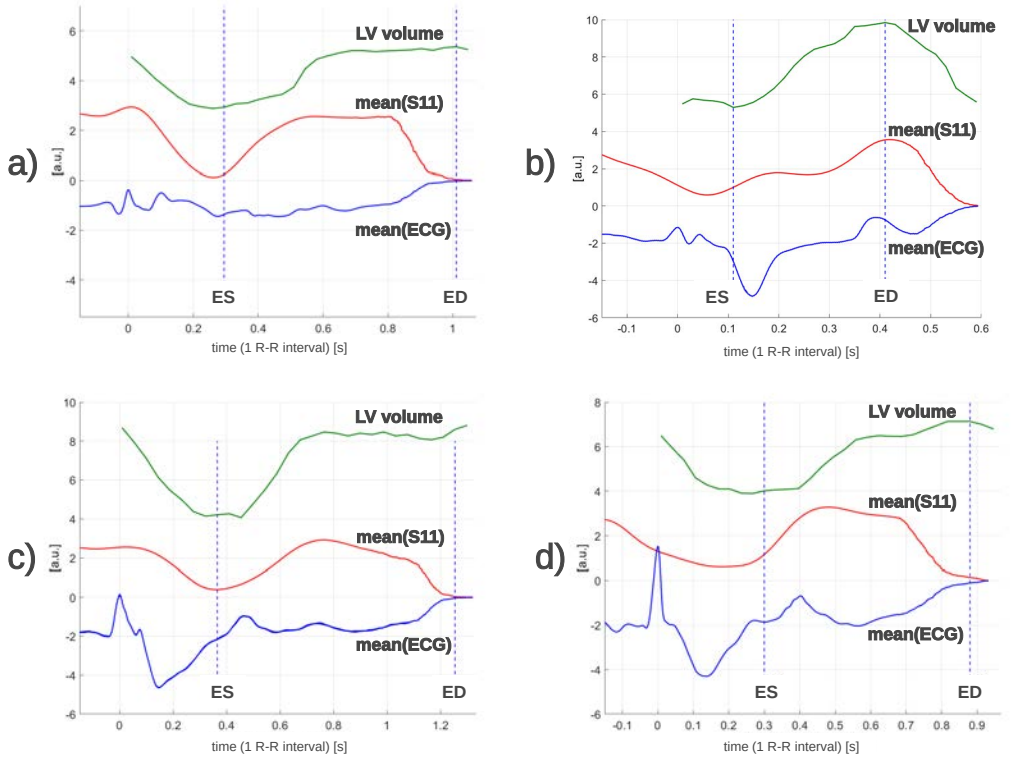

Figure 6.14 – Comparison of the mean values of the super-imposed ECG (blue) and S11 (red) data for one heart beat, and the segmented LV volume progress (green). The data for a) volunteer 2, b) volunteer 3, c) volunteer 4, and d) volunteer 5 are shown The values of the correlation coefficient R2 are a) 0.71, b) 0.72, c) 0.78, and d) 0.52, respectively

for the free-breathing data of volunteer 5. The duration between adjacent peaks of both signals were analyzed. The Bland-Altman diagram shown in Fig. 6.15 reveals good correlation ($R^2 = 0.86$) between the R-R intervals of the ECG R-peaks and the peaks of the S11 data.

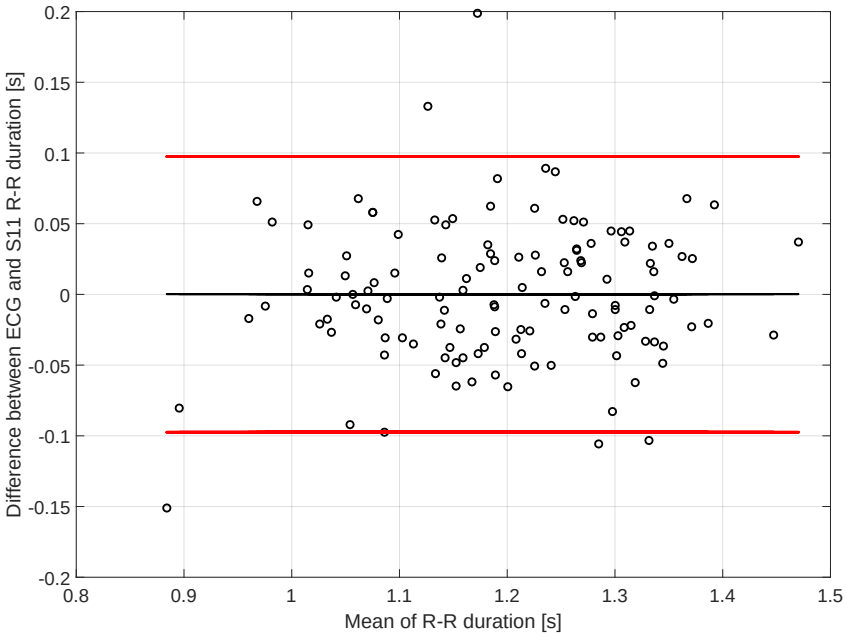

Figure 6.15 – Bland-Altman plot of R-R durations measured from ECG data and S11-data (R^2=0.86). Red lines indicate 2σ standard deviation

6.3 Simultaneous load change acquisition of a multi-channel coil

The temporal acquisition of reflected power or reflection coefficient of a coil element represents organ or flow motion in the underlying area. Single elements can give a substitute of this motion if the organ structure in the coil's vicinity is homogeneous and the effect on the coil load is dominant. As shown earlier, this is sufficient for respiratory motion or local blood flow representation (Section 6.1) or as an indicator for general patient motion (Section 5.1).

A combination of reflection coefficient fluctuations of multiple coil elements might give more detailed spatial information of the physiological position changes. Reflection coefficient variations alone, however, would be limited to the near-surface zone underneath each specific coil element. In order to get a full spatially encoded motion profile, one would need to understand the motion throughout the subject. The variation of the transmission coefficient of opposed coil elements could give such through body motion information and could add additional information to the reflection coefficient of each separate coil element. The effect of physiological motion to the transmission and reflection coefficient of a four-channel 1.5T cardiac coil was evaluated in a lab experiment.

6.3.1 S-parameter setup on 4-channel cardiac coil

Figure 6.16 – 1.5T four channel cardiac coil; Coil cover is removed and direct connections to the coil are visible

The coil is shown in Fig. 6.16. The dimensions of each element are 200 x 250 mm. Since the pre-amplifier for that type of coil is placed in the MRI system after the

coil connector, the coil elements were directly accessible via the SMA connectors. A four-port network analyzer (ZVB4, Rohde & Schwarz) generated and measured the signal at the resonant frequency on each coil element continuously. Transmission (S_{xy}) and reflection (S_{xx}) coefficients were measured and saved during the experiment by a LabView application (Section 3.3.3). It was supposed, that the transmission coefficients in both directions were equal. This reduced the total number of S-parameters from 16 to ten (S_{11}, S_{22}, S_{33}, S_{44}, S_{12}, S_{13}, S_{14}, S_{23}, S_{24} and S_{34}).

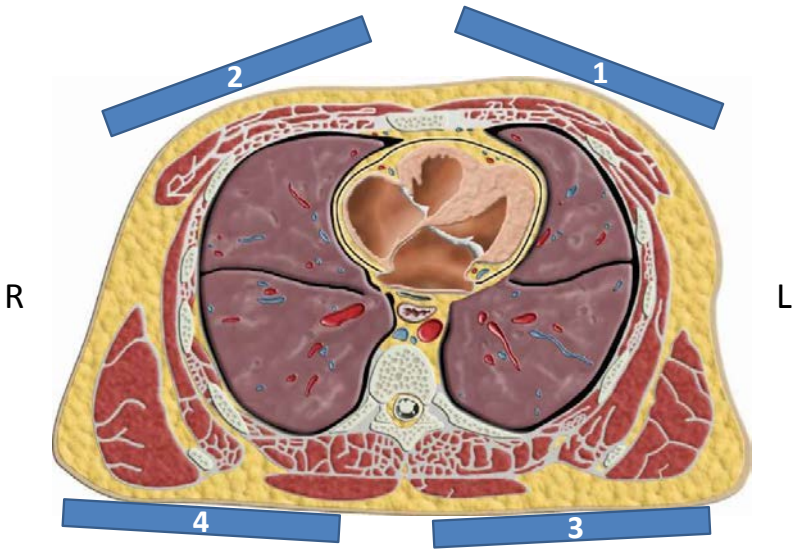

Figure 6.17 – Schematic of the coil element positions on the volunteer

A volunteer was placed on the patient table of the MRI system, with his back on the posterior part of the four-channel cardiac coil. ECG, PPG, and the respiratory belt were positioned on the volunteer and the anterior part was strapped on top of the chest. The position of the coil elements is illustrated in Fig. 6.17. The data was filtered and processed with MATLAB using the same filter algorithms as described in Section 6.2.

6.3.2 4-port S-parameters of a volunteer measurement

Figs. 6.18 and 6.19 show the filtered signal of the reflection and transmission parameters of a four-channel cardiac coil filtered for respiratory frequency and compared to the respiratory belt. The impedance variations due to breathing were represented by all four channels. However, the signal of the posterior coil shows better stability than the anterior signal. This is caused by the higher mechanical stability of the posterior coil due to the volunteer weight. Further more the S_{11} data shows a negated trend compared to the respiratory belt, while S_{22} shows a combination of two phase shifted signals. This might be caused by an unstable fixation of the anterior coil.

The same signal was also band-pass filtered between 0.8 Hz and 3 Hz and superimposed over 65 R-R intervals. A cardio-physiologic motion can be distinguished and compared to PPG (Figs. 6.20 and 6.21). The reflection coefficients of the anterior part show a small deviation from the mean. Additionally, a time delay of 100 ms is visible in S_{22} data. The posterior signals have larger variations, which is an indication of a weak cardiac motion component at this position. Also, in transmission coefficients, these larger variations are observable in the areas far from the heart (S_{34} and S_{23}). The S_{14} coefficient (which lies along the heart motion axis) and the S_{23} coefficient (perpendicular to the heart motion axis) are more stable. As described earlier in Section 6.1, these signals represent primarily blood flow and ventricular volumina changes, although with different flow characteristics due to different distances to the heart. Further analysis of the heart motion and the observed signal is needed to understand the signals and combine them to a motion model.

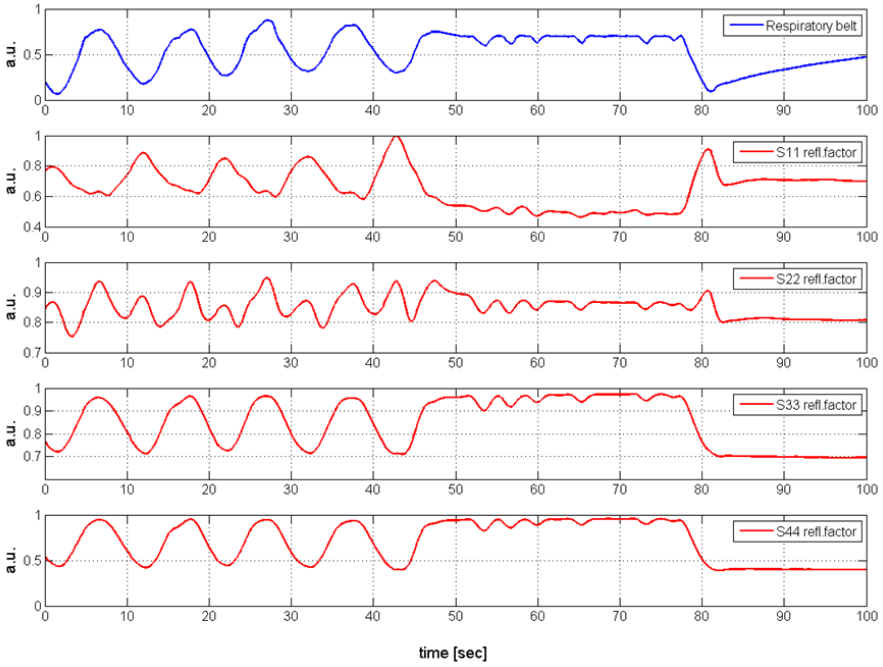

Figure 6.18 – Respiratory portion of reflection coefficients of 4-ch coil during free-breathing; S_{33} and S_{44} signal is more stable, due to mechanical fixation by the volunteers weight

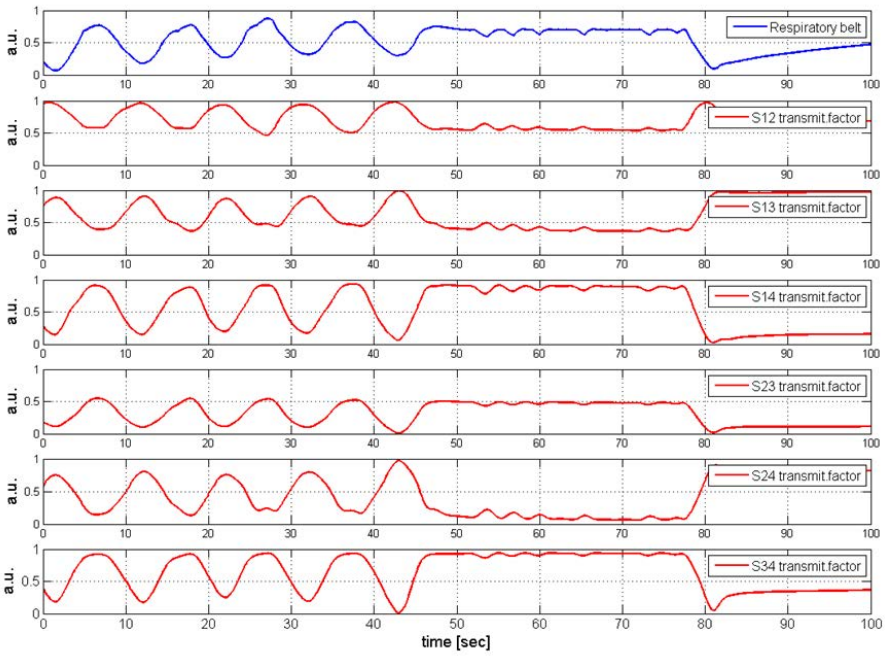

Figure 6.19 – Respiratory portion of transmission coefficients of 4-ch coil during free-breathing; All transmission coefficient represented the respiratory motion equally well

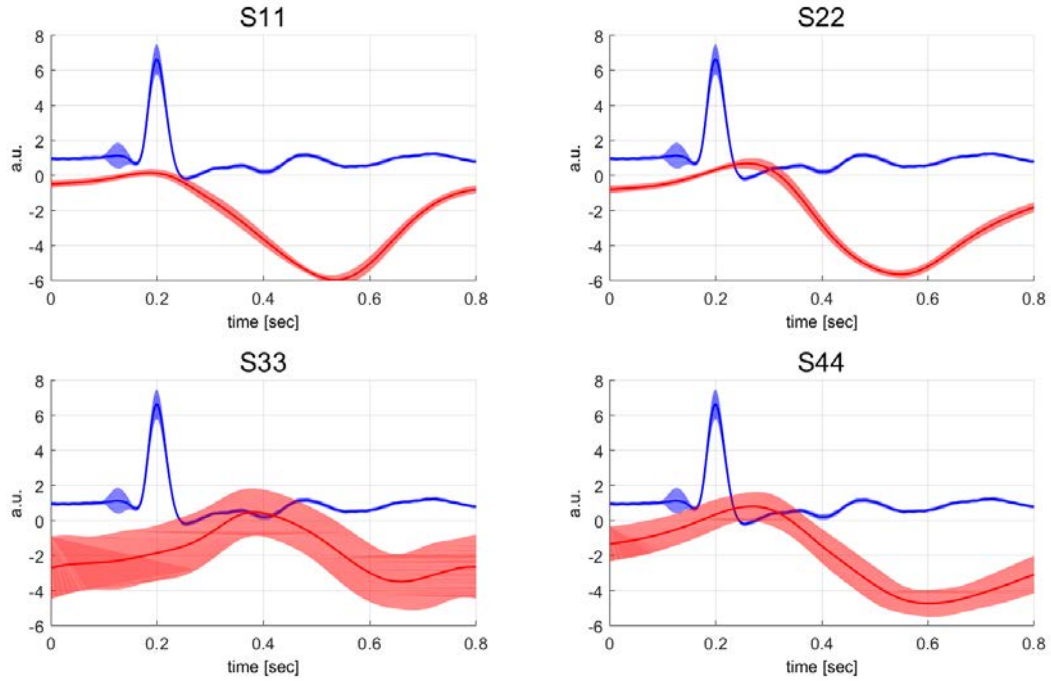

Figure 6.20 – Cardiophysiologic signal of reflection coefficients of 4-ch coil during free-breathing. A higher standard deviation is observed in S_{33} and S_{44} signal, mainly due to the larger distance to the heart

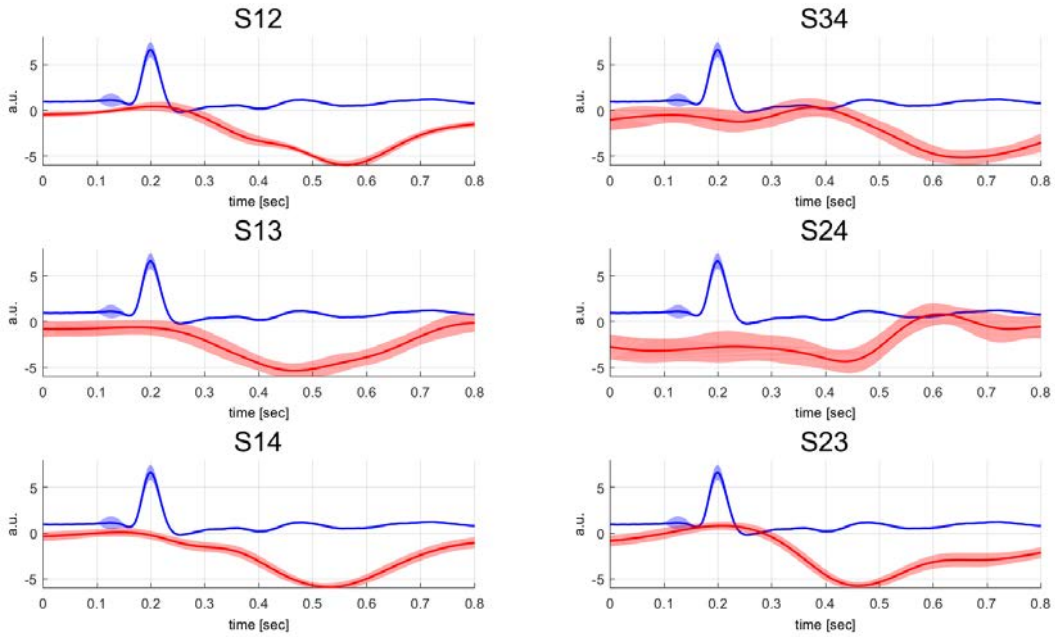

Figure 6.21 – Cardiophysiologic signal of transmission coefficients of 4-ch coil during free-breathing; Signal along the heart axis (S_{14} and S_{23}) are more accurate and show lower standard deviation

6.4 Discussion

Coil load changes on surface coils represent various physiological signals like respiration, blood flow, and blood volume changes on the chest. But in other body areas arterial blood flow can be detected as well. This enables the possibility to measure cardiovascular information using multi-channel coils in parallel to the imaging sequence. Localized measurements on the sternum are proven to detect respiratory and cardiac motion. As shown by an analysis of the left ventricular volume and ECG peaks, the blood volume variations of the heart represent the mechanical motion of the myocardium and could be applied as a real end-diastolic trigger for cardiac imaging.

By a direct comparison of the measurements in Sections 6.1 and 6.2, it can be shown that the signal quality depends on the coil dimension and the location of the coil element. Especially on the torso, various physiological signals like respiration, blood flow, and blood volume changes can overlap on larger coil diameters (Section 6.2). However, if one considers a multi-channel imaging coil instead of single-loop coils, dedicated algorithms could be implemented to find the coil element with the most stable signal.

With multi-channel coils, transmission coefficients can contain additional valuable motion information. In combination with reflection coefficients, they might provide sufficient input for through-body motion models. The four-channel cardiac coil showed a spatial signal separation in the left-right and anterior-posterior directions. Due to the large dimensions, the cardio-physiologic signal holds information from multiple sources - e.g. arterial blood flow, and ventricular and atrial blood volume changes. Nevertheless, the signals in the close proximity of the heart, along the motion axis or perpendicular to the motion axis gave stable and reproducible results. With modern multi-element coils (e.g. a 32-channel cardiac coil), motion information in the superior-inferior direction and with higher spatial resolution might be achieved. This would enable the prescription of a full 3D representation of the physiological motion. Furthermore, high-Q coils could increase the sensitivity, which would be beneficial for the small signals of e.g. arterial blood flow. However, such coils have to be carefully designed because higher motion sensitivity and decreases SNR due to larger loading effects.

Part III

Discussion and Outlook

Discussion - Advantages and Limitations

The ability of coil load changes on MRI coils for motion detection was investigated. Electromagnetic simulations of a single loop coil on the human torso were compared to in-vitro and in-vivo lab bench experiments. Although the simulation model was simplified, the measured data correlated well to the simulation results independent of the design frequency.

In-vivo measurements were performed on different coils inside the MRI magnet tunnel. Contact-less respiratory motion registration has been shown with the Tx/Rx body coil with two different approaches. While the first method was utilizing the reflected power of the excitation pulse for motion recording, the second method showed a sequence independent setup with the birdcage coil harmonic frequencies. Both methods showed good correlation of $R^2 = 0.78$ and 0.73, respectively, to the recorded data of the pneumatic belt.

Two volunteer studies with single loop coils showed various physiologic motion information at different positions on the human body, namely respiratory motion, blood volume variation due to myocardial contraction and blood flow in peripheral arteries. Motion data on the chest was shown to be a modulation of respiratory and cardiophysiologic signals, whereas the latter indicated a direct relationship to the mechanical heart contraction. In a clinical setup, the motion signal of a loop coil was recorded during Cine imaging on five volunteers. Besides the respiratory and cardiophysiologic motion signal, the ability for a cardiac trigger was investigated. In addition the acquired motion signal was used with the retrospective GRICS correction algorithm.

Furthermore, the coil loading variations of four coil elements were analyzed. Here reflection and transmission coefficients of a vector analyzer were recorded concurrently. The data intensity and stability was dependent on the coil position. The cardiac signal through the body along the heart axis had lower standard deviation compared to other signal paths, indicating motion direction information in the acquired data.

Advantages of imaging coils as motion sensors

The usage of the imaging coil for motion detection provides a promising sensorless solution. Because the coil is already placed on or near the patient and in the accordant ROI, other sensors can be eliminated. Furthermore during the imaging sequence the imaging coil is only used for a small percentage of the sequence time. Tx/Rx-coils, as the body birdcage coil, are active during spin excitation and image acquisition, surface coils are used to acquire image data only. For the rest of the sequence the coil is not in use and could be utilized for motion recording. The good compatibility of the coil inside the magnetic field is a further advantage over other sensors. During this thesis the usage of a time-of-flight camera inside the bore was also investigated [Kudielka et al., 2015b]. Although motion tracking inside the bore

was possible, a significant temperature increase due to components inside the camera interacting with the main magnetic field and a sensitivity against the RF excitation fields was observed. This limited the application of the in-bore camera and further design changes would have to be taken into account. Inherently, RF coils do not have this problem inside the magnet tunnel.

A further advantage of the coil loading technique is the penetration into the body. Other motion detection methods, like optical systems or electro-mechanical systems, provide only information from the body surface. This might be sufficient for tracking bulk body motion or head motion, however can give no or only indirect information on physiological motion inside the body. As shown is this work, the blood volume change, myocardial contraction and the arterial pulse flow can be visualized by coil load variations. The ventricular blood volume variation revealed a direct analogy with the heart contraction, which was not detectable with ECG or PPG. Knowledge of the heart motion might be useful to e.g. identify end-diastolic motion states.

The measurement setup for motion registration with the inbuilt body coil by power reflection during the excitation pulse could be easy to realize and might be even possible with the hardware already existing in the system (see the Outlook section for further information). Phased-array coils can provide localized motion information at various locations simultaneously. Although further investigation is needed, current experiments show promising results for directional information of the motion signal, which could be used for spatial resolved motion model of the organ.

Limitations of imaging coils as motion sensors

The continuous impedance measurement necessitates constant current flow through the coil. Hence, an increase in the noise level, supplementary proton saturation, and an increase in the SAR level may have negative effects due to this measurement technique. As shown in Table 11, a motion signal power level of 1 mW enhances the noise level by a factor of 20 in the same coil. On the other hand, the same power level on a ^{31}P surface coil had no effect on the imaging coil. As this power level is equivalently lower than 1 ppm of the excitation pulse, the effect on spin manipulation was negligible.

Filtering or switching setups might be necessary to separate the imaging functionality of the coil from the motion detection, if the imaging coil is utilized for motion detection. The switching might be rather complex, as fast state alteration and low insertion losses are required. Moreover, the switching would cause information gaps in the motion data during the RF transmission and image acquisition. Nevertheless, the excitation and acquisition windows are usually very short compared to the frequency of the motion, and interpolation of the missing data should be sufficient to close the gaps.

As it can be recognized by the comparison of Section 6.1 and Section 6.2, the diameter of the surface coil determines the accuracy of the measurement, especially on positions were multiple motion sources are present. In the region of the heart, blood flow in the atria, aorta or pulmonary system can modulate the signal of the ventricular blood volume, which represents the myocardial contraction. This is shown in the results of the ^{31}P surface coil, with a diameter of 150 mm. The signal of the 75

mm loop coil showed higher reproducibility on the cardiac filtered signal throughout the volunteers.

As generally valid for motion sensors, the positioning of the coil is crucial for data reliability. In cardiac imaging the surface coil is fixed with straps and sporadic motion might be neglected. Volume coils however detect any motion inside the coil. This could be used as a general motion detector, which sends a warning message to the examiner when motion occurs or need some dedicated filtering.

The coil impedance can only be accessed directly at the resonating structure. In modern coil design, the preamplifier is often used also for matching purposes (preamplifier decoupling) and the image signal is digitized on the coil to reduce noise. Hence motion measurement setups after the coil connector can be difficult to implement and thus have to be realized in the coil design already. Some possible implementations are described in the following Outlook chapter.

The coil loading influence on imaging

In Fig. 5.2 the variation of the reflected power from the coil is compared to the transmitted power from the amplifier during various excitation pulses. Hence the effective power for spin excitation varies accordingly. The physiologic motion affects both, the loading of the transmitting coil as well as the receiving coil, which are often of different origin. Load variations are pronouncedly different, because the capacitive coupling is enhanced on volume coils, while conductivity changes have a stronger influence on surface coils. Using the same coil for transmission and reception of the NMR signal, motion induced variations on the transmitted B_1 field could be, therefore, different from variations of the received B_1 field. The principle of reciprocity is based on static conditions and hence the acquired B_1 fields could not show the effective transmit field. Currently the effect of the motion induced power change on the transmit B_1 field is further investigated.

Outlook

This thesis showed in various experimental setups the proof-of-concept for motion detection with imaging coils. The usage of birdcage coil harmonics was applied for patent and published in January 2016. Furthermore the SAEC system was further development and became independent from the third party monitor.

These results can the basis for new MRI motion detection system. For example one could think of an integration of the SAEC into the firmware or an extension of the power monitoring system to a combined power and motion monitoring system.

Implementation of coil based motion detection

Acquisition of the respiratory motion by recording power variations of the RF excitation pulses on the transmission coil can be realized relatively easy. In general the power amplifier contains a directional coupler to measure the outgoing power with the reflected or returning power. Connecting a power sensor or oscilloscope to the coupled reflected port of the directional coupler is already sufficient to detect power variations due to respiratory motion or body movement. The MRI system itself uses the forward and reflected power information to monitor the absorbed energy and SAR limits. Dedicated firmware changes could utilize this power monitoring for contact-less motion detection.

As described above, motion measurement setups can be included in the coil design. Such an on-coil setup could include fast MEMS switches [131] and on-coil directional couplers [132]. In addition, a setup considering the magnitude and phase of the reflected power could enhance the motion signal [113]. Positioning of single loop elements was shown to be critical for signal reliability.

Although not investigated in this work, coil loading variations could give quantitative information on e.g. the stroke volume by dedicated calibration methods. This would give additional information during the image acquisition already.

In summary, coil load variations are an interesting effect which could serve for motion tracking or might provide additional patient information besides the images.

Thesis related publications

[Kudielka et al., 2015] Kudielka, G. P., Hardy, C., Vuissoz, P.-A., Felblinger, J., and Brau, A. C. (2015). Utilization of the Receive Coil for cardiovascular and respiratory motion representation. *Oral Presentation, In Proceedings of the 23rd Annual Meeting of the ISMRM, Toronto, Canada (p. 705).*

[Kudielka et al., 2014a] Kudielka, G. P., Menini, A., Vuissoz, P.-A., Brau, A. C., and Felblinger, J. (2014a). Reflected power as a breathing signal for motion correction in cMRI with GRICS. *In:Proceedings Scientific Workshop "Motion in MRI", International Society for Magnetic Resonance in Medicine, Tromso, Norway.*

[Kudielka et al., 2014b] Kudielka, G. P., Vuissoz, P.-A., Brau, A. C., and Felblinger, J. (2014b). Usage of birdcage coil harmonic frequencies for measurement of respiration induced impedance changes. *In:Proceedings Scientific Workshop "Motion in MRI", International Society for Magnetic Resonance in Medicine, Tromso, Norway.*

[Kudielka et al., 2016a] Kudielka, G. P., Vuissoz, P.-A., and Felblinger, J. (2016a). *POWER MEASUREMENT ON MAGNETIC RESONANCE IMAGING COIL AT DIFFERENT FREQUENCY THAN LARMOR FREQUENCY.* US20160003927.

[Kudielka et al., 2016b] Kudielka, G. P., Vuissoz, P.-A., Odille, F., Menini, A., and Felblinger, J. (2016b). Sensor-less, continuous recording of cardiac and respiratory motion based on load changes on MR radiofrequency coils. *IEEE Transactions on Biomedical Engineering, submitted on May, 12th 2016.*

Other publications

[Bustin et al., 2016] Bustin, A., Odille, F., Kudielka, G. P., Janich, M. A., Brau, A. C., and Menini, A. (2016). A fully automated binning method for improved SHARP reconstruction of free-breathing cardiac images. *Poster Presentation, In Proceedings of the 19th Annual SCMR Scientific Sessions, Los Angeles, CA, USA*.

[Kudielka et al., 2015a] Kudielka, G. P., Kluge, T., Shair, S., and Menzel, M. (2015a). Magnetic Resonance Imaging for 3D Resin Flow and Curing Process Monitoring. *Oral Presentation, In Proceedings of the Composite and Advanced Materials Expo (CAMX), Dallas, TX, USA*.

[Kudielka et al., 2015b] Kudielka, G. P., Menini, A., Vuissoz, P.-A., Felblinger, J., and Wiesinger, F. (2015b). Technical feasibility and potential applications of an optical Time-Of-Flight camera mounted inside the MR scanner. *Oral Presentation, In Proceedings of the 23rd Annual Meeting of the ISMRM, Toronto, Canada (p. 705)*.

Bibliographie

[1] CA Roobottom, G Mitchell, and G Morgan-Hughes. Radiation-reduction strategies in cardiac computed tomographic angiography. *Clinical radiology*, 65(11):859–867, 2010.

[2] T Filipe, L Ribeiro, R Almeida, S Rodrigues, K Azevedo, C Silva, and A Abrantes. Radiographers perceptions of magnetic resonance imaging: a study of the causes that lead to the exams repetition. *Proceedings of the ECR2013*, 2013.

[3] JB Andre, BW Bresnahan, M Mossa-Basha, MN Hoff, CP Smith, Y Anzai, and WA Cohen. Toward quantifying the prevalence, severity, and cost associated with patient motion during clinical mr examinations. *Journal of the American College of Radiology*, 12(7):689–695, 2015.

[4] D Buikman, T Helzel, and P Röschmann. The RF coil as a sensitive motion detector for mri studied up to 2 tesla. *Magnetic Resonance Imaging*, 4(2):169–170, 1986.

[5] EM Purcell, HC Torrey, and RV Pound. Resonance absorption by nuclear magnetic moments in a solid. *Physical review*, 69(1-2):37, 1946.

[6] F Bloch. Nuclear induction. *Physical Review*, 70(7-8):460–474, October 1946.

[7] PC Lauterbur. Image formation by induced local interactions: examples employing nuclear magnetic resonance. *Nature*, 242(5394):190–191, 1973.

[8] P Mansfield and PK Grannell. NMR diffraction in solids. *Journal of Physics C: solid state physics*, 6(22):L422, 1973.

[9] FA Duck. *Physical properties of tissues: a comprehensive reference book*. Academic press, 2013.

[10] JP Wansapura, SK Holland, RS Dunn, and WS Ball. NMR relaxation times in the human brain at 3.0 tesla. *Journal of magnetic resonance imaging*, 9(4):531–538, 1999.

[11] CMJ de Bazelaire, GD Duhamel, NM Rofsky, and DC Alsop. MR imaging relaxation times of abdominal and pelvic tissues measured in vivo at 3.0 T: preliminary results 1. *Radiology*, 230(3):652–659, 2004.

[12] DI Hoult. The signal-to-noise ratio of the nuclear magnetic resonance experiment. *Journal of Magnetic Resonance*, 24(1):71–85, 1976.

[13] J Maclaren, M Herbst, O Speck, and M Zaitsev. Prospective motion correction in brain imaging: a review. *Magnetic resonance in medicine*, 69(3):621–636, 2013.

[14] HW Korin, JP Felmlee, SJ Riederer, and RL Ehman. Spatial-frequency-tuned markers and adaptive correction for rotational motion. *Magnetic resonance in medicine*, 33(5):663–669, 1995.

[15] RL Ehman and JP Felmlee. Adaptive technique for high-definition mr imaging of moving structures. *Radiology*, 173(1):255–263, 1989.

[16] ML Wood and RM Henkelman. MR image artifacts from periodic motion. *Medical physics*, 12(2):143–151, 1985.

[17] ML Wood and RM Henkelman. The magnetic field dependence of the breathing artifact. *Magnetic Resonance Imaging*, 4(5):387–392, 1986.

[18] JT Marcus, MJW Goette, LK DeWaal, MR Stam, RJ Van der Geest, RM Heethaar, and AC Van Rossum. The influence of through-plane motion on left ventricular volumes measured by magnetic resonance imaging: implications for image acquisition and analysis. *Journal of Cardiovascular Magnetic Resonance*, 1(1):1–6, 1999.

[19] P-F Van de Moortele, J Pfeuffer, GH. Glover, K Ugurbil, and X Hu. Respiration-inducedB0 fluctuations and their spatial distribution in the human brain at 7 Tesla. *Magnetic Resonance in Medicine*, 47(5):888–895, May 2002.

[20] VO Boer, BL vd Bank, G van Vliet, R Luijten, and DWJ Klomp. Direct B0 field monitoring and real-time B0 field updating in the human breast at 7 Tesla. *Magnetic Resonance in Medicine*, 67(2):586–591, February 2012.

[21] T Verma and J Cohen-Adad. Effect of respiration on the B0 field in the human spinal cord at 3T: Effect of Respiration on B0 Field in Human Spinal Cord. *Magnetic Resonance in Medicine*, 72(6):1629–1636, December 2014.

[22] PJ Bolan, P-G Henry, EH Baker, S Meisamy, and M Garwood. Measurement and correction of respiration-induced B0 variations in breast 1H MRS at 4 Tesla. *Magnetic Resonance in Medicine*, 52(6):1239–1245, December 2004.

[23] D Raj, AW Anderson, and JC Gore. Respiratory effects in human functional magnetic resonance imaging due to bulk susceptibility changes. *Physics in medicine and biology*, 46(12):3331, 2001.

[24] Y Wang, SJ Riederer, and RL Ehman. Respiratory motion of the heart: kinematics and the implications for the spatial resolution in coronary imaging. *Magnetic Resonance in Medicine*, 33(5):713–719, 1995.

[25] KE Barrett, S Boitano, SM Barman, and HL. Brooks. *Review of medical physiology*, volume 24. McGraw-Hill Medical New York, 2012.

[26] AD Scott, J Keegan, and DN Firmin. Motion in Cardiovascular MR Imaging 1. *Radiology*, 250(2):331–351, 2009.

[27] B Jung, D Föll, P Böttler, S Petersen, J Hennig, and M Markl. Detailed analysis of myocardial motion in volunteers and patients using high-temporal-resolution mr tissue phase mapping. *Journal of Magnetic Resonance Imaging*, 24(5):1033–1039, 2006.

[28] N Kawel-Boehm, A Maceira, ER Valsangiacomo-Buechel, J Vogel-Claussen, EB Turkbey, R Williams, S Plein, M Tee, J Eng, and DA Bluemke. Normal values for cardiovascular magnetic resonance in adults and children. *Journal of Cardiovascular Magnetic Resonance*, 17(1), December 2015.

[29] The Reference Values for Arterial Stiffness' Collaboration. Determinants of pulse wave velocity in healthy people and in the presence of cardiovascular risk factors: establishing normal and reference values. *European Heart Journal*, 31(19):2338–2350, October 2010.

[30] V Taviani, SS Hickson, CJ Hardy, AJ Patterson, V. Young, CM McEniery, IB Wilkinson, JH Gillard, and MJ Graves. Estimation of aortic pulse pressure using fourier velocity encoded M-mode MR: Aortic Pulse Pressure by M-mode MR. *Journal of Magnetic Resonance Imaging*, 39(1):85–93, January 2014.

[31] M Zaitsev, J Maclaren, and M Herbst. Motion artifacts in MRI: A complex problem with many partial solutions: Motion Artifacts and Correction. *Journal of Magnetic Resonance Imaging*, 42(4):887–901, October 2015.

[32] HMA de Bie, M Boersma, MP Wattjes, S Adriaanse, RJ Vermeulen, KJ Oostrom, J Huisman, DJ Veltman, and HA Delemarre-Van de Waal. Preparing children with a mock scanner training protocol results in high quality structural and functional MRI scans. *European journal of pediatrics*, 169(9):1079–1085, 2010.

[33] Y Wang, PS Christy, FR Korosec, MT Alley, TM Grist, JA Polzin, and CA Mistretta. Coronary MRI with a respiratory feedback monitor: the 2D imaging case. *Magnetic resonance in medicine*, 33(1):116–121, 1995.

[34] C Jahnke, I Paetsch, S Achenbach, B Schnackenburg, R Gebker, E Fleck, and E Nagel. Coronary MR Imaging: Breath-hold capability and patterns, coronary artery rest periods, and β-blocker use 1. *Radiology*, 239(1):71–78, 2006.

[35] C Plathow, S Ley, J Zaporozhan, M Schöbinger, M Gruenig, Eand Puderbach, M Eichinger, H-P Meinzer, I Zuna, and H-U Kauczor. Assessment of reproducibility and stability of different breath-hold maneuvres by dynamic MRI: comparison between healthy adults and patients with pulmonary hypertension. *European radiology*, 16(1):173–179, 2006.

[36] E Kaza, R Symonds-Tayler, DJ Collins, F McDonald, HA McNair, E Scurr, DM Koh, and MO Leach. First MRI application of an active breathing coordinator. *Physics in medicine and biology*, 60(4):1681, 2015.

[37] P Mansfield. Multi-planar image formation using nmr spin echoes. *Journal of Physics C: Solid State Physics*, 10(3):L55, 1977.

[38] A Haase, J Frahm, D Matthaei, W Hanicke, and K-D Merboldt. FLASH imaging. rapid NMR imaging using low flip-angle pulses. *Journal of Magnetic Resonance (1969)*, 67(2):258–266, 1986.

[39] K Scheffler and S Lehnhardt. Principles and applications of balanced SSFP techniques. *European radiology*, 13(11):2409–2418, 2003.

[40] J Hennig, A Nauerth, and H Friedburg. RARE imaging: a fast imaging method for clinical MR. *Magnetic resonance in medicine*, 3(6):823–833, 1986.

[41] DK Sodickson and WJ Manning. Simultaneous acquisition of spatial harmonics (SMASH): fast imaging with radiofrequency coil arrays. *Magnetic Resonance in Medicine*, 38(4):591–603, 1997.

[42] KP Pruessmann, M Weiger, MB Scheidegger, P Boesiger, et al. SENSE: sensitivity encoding for fast MRI. *Magnetic resonance in medicine*, 42(5):952–962, 1999.

[43] DR Bailes, DJ Gilderdale, GM Bydder, AG Collins, and DN Firmin. Respiratory ordered phase encoding (ROPE): a method for reducing respiratory motion artefacts in MR imaging. *Journal of computer assisted tomography*, 9(4):835–838, 1985.

[44] EM Haacke and GW Lenz. Improving MR image quality in the presence of motion by using rephasing gradients. *American journal of roentgenology*, 148(6):1251–1258, 1987.

[45] L Axel and D Morton. MR flow imaging by velocity-compensated/uncompensated difference images. *Journal of computer assisted tomography*, 11(1):31–34, 1987.

[46] BMA Delattre, RM Heidemann, LA Crowe, J-P Vallée, and J-N Hyacinthe. Spiral demystified. *Magnetic resonance imaging*, 28(6):862–881, 2010.

[47] G Buonincontri, C Methner, T Krieg, TA Carpenter, and SJ Sawiak. Trajectory correction for free-breathing radial cine MRI. *Magnetic Resonance Imaging*, 32(7):961–964, September 2014.

[48] M Zaitsev, C Dold, G Sakas, J Hennig, and O Speck. Magnetic resonance imaging of freely moving objects: prospective real-time motion correction using an external optical motion tracking system. *Neuroimage*, 31(3):1038–1050, 2006.

[49] LM Louis and BK Rutt. Generalized k-space analysis and correction of motion effects in mr imaging. *Magnetic resonance in medicine*, 30(4):438–446, 1993.

[50] F Odille, P-A Vuissoz, P-Y Marie, and J Felblinger. Generalized reconstruction by inversion of coupled systems (GRICS) applied to free-breathing MRI. *Magnetic Resonance in Medicine*, 60(1):146–157, 2008.

[51] GM Bydder and MD Robson. Partial fourier partially parallel imaging. *Magnetic resonance in medicine*, 53(6):1393–1401, 2005.

[52] JFM Schmidt, L Wissmann, R Manka, and S Kozerke. Iterative k-t principal component analysis with nonrigid motion correction for dynamic three-dimensional cardiac perfusion imaging. *Magnetic resonance in medicine*, 72(1):68–79, 2014.

[53] RL Ehman, MT McNamara, M Pallack, H Hricak, and CB Higgins. Magnetic resonance imaging with respiratory gating: techniques and advantages. *American journal of roentgenology*, 143(6):1175–1182, 1984.

[54] ME Wagshul, S Sin, ML Lipton, K Shifteh, and R Arens. Novel retrospective, respiratory-gating method enables 3D, high resolution, dynamic imaging of the upper airway during tidal breathing: Retrospective, Respiratory-Gated, Upper Airway Imaging. *Magnetic Resonance in Medicine*, 70(6):1580–1590, December 2013.

[55] L Rousselet, M Filipovic, Z Ramdane-Cherif, V Laurent, C Pasquier, and J Felblinger. MR compatible sensor for measuring respiratory motion based on acceleration . In *Proceedings of the 19th Scientific Meeting, International Society for Magnetic Resonance in Medicine*, page 143, Stockholm, 2010. ISMRM.

[56] G Bonmassar, PL Purdon, IP Jääskeläinen, K Chiappa, V Solo, EN Brown, and JW Belliveau. Motion and ballistocardiogram artifact removal for interleaved recording of EEG and EPs during MRI. *Neuroimage*, 16(4):1127–1141, 2002.

[57] T Frauenrath, F Hezel, W Renz, d'Orth TG., M Dieringer, F von Knobelsdorff-Brenkenhoff, M Prothmann, J Menger, and T Niendorf. Acoustic cardiac triggering: a practical solution for synchronization and gating of cardiovascular magnetic resonance at 7 Tesla. *J Cardiovasc Magn Reson*, 12(1):67, 2010.

[58] F Kording, B Schoennagel, G Lund, F Ueberle, C Jung, G Adam, and J Yamamura. Doppler ultrasound compared with electrocardiogram and pulse oximetry cardiac triggering: A pilot study: Alternative Trigger Technique for Cardiac MRI Using DUS. *Magnetic Resonance in Medicine*, pages 1257–1265, October 2014.

[59] U Wedegaertner, M Frisch, I Kopp, J Graessner, K Hecher, G Adam, and J Yamamura. A Novel Technique for Cardiac MRI of the Fetal Heart: MR compatible Doppler Ultrasound (CTG) for CardiacTriggering. In *Proceedings 20th Scientific Meeting, International Society for Magnetic Resonance in Medicine*, 2011.

[60] J Schulz, T Siegert, E Reimer, C Labadie, J Maclaren, M Herbst, M Zaitsev, and R Turner. An embedded optical tracking system for motion-corrected magnetic resonance imaging at 7t. *Magnetic Resonance Materials in Physics, Biology and Medicine*, 25(6):443–453, December 2012.

[61] J Maclaren, M Aksoy, and R Bammer. Contact-free physiological monitoring using a markerless optical system: Contact-Free Physiological Monitoring. *Magnetic Resonance in Medicine*, 74(2):571–577, August 2015.

[62] J Xia and RA Siochi. A real-time respiratory motion monitoring system using KINECT: Proof of concept. *Medical Physics*, 39(5):2682–2685, May 2012.

[63] J Ortmüller, T Gauer, M Wilms, H Handels, and R Werner. Respiratory surface motion measurement by Microsoft Kinect. *Current Directions in Biomedical Engineering*, 1(1), January 2015.

[64] C Schaller, J Penne, and J Hornegger. Time-of-flight sensor for respiratory motion gating. *Medical Physics*, 35(7):3090, 2008.

[65] A Smith, S Kim, C Serago, K Hintenlang, R Pooley, and D Hintenlang. Development of an mr and ct compatible non-invasive temperature based optical fiber respiration sensor for use in radiotherapy. In *World Congress on Medical Physics and Biomedical Engineering, June 7-12, 2015, Toronto, Canada*, pages 603–606. Springer, 2015.

[66] H Eviatar, B Schattka, JC Sharp, J Rendell, and ME Alexander. Real time head motion correction for functional mri. page 269, 1999.

[67] JA Derbyshire, GA Wright, RM Henkelman, and RS Hinks. Dynamic scan-plane tracking using mr position monitoring. *Journal of magnetic resonance imaging*, 8(4):924–932, 1998.

[68] S Sengupta, S Tadanki, JC Gore, and EB Welch. Prospective real-time head motion correction using inductively coupled wireless NMR probes: Head Motion Correction Using Wireless NMR Probes. *Magnetic Resonance in Medicine*, 72(4):971–985, October 2014.

[69] MB Ooi, M Aksoy, J Maclaren, RD Watkins, and R Bammer. Prospective motion correction using inductively coupled wireless RF coils: Prospective Motion Correction Using Wireless Markers. *Magnetic Resonance in Medicine*, 70(3):639–647, September 2013.

[70] A Peshkovsky, KH Knuth, and JA Helpern. Motion correction in MRI using an apparatus for dynamic angular position tracking (ADAPT). *Magnetic Resonance in Medicine*, 49(1):138–143, January 2003.

[71] M Haeberlin, L Kasper, C Barmet, DO Brunner, BE Dietrich, S Gross, BJ Wilm, S Kozerke, and KP Pruessmann. Real-time motion correction using gradient tones and head-mounted NMR field probes: Real-Time Motion Correction using Gradient Tones and NMR Field Probes. *Magnetic Resonance in Medicine*, 74(3):647–660, September 2014.

[72] SJ Vannesjo, BJ Wilm, Y Duerst, S Gross, DO Brunner, BE Dietrich, T Schmid, C Barmet, and KP Pruessmann. Retrospective correction of physiological field fluctuations in high-field brain MRI using concurrent field monitoring: Physiological Field Correction Using Concurrent Field Monitoring. *Magnetic Resonance in Medicine*, 73(5):1833–1843, May 2015.

[73] F Thiel, D Kreiseler, and F Seifert. Non-contact detection of myocardiums mechanical activity by ultrawideband RF-radar and interpretation applying electrocardiography. *Review of Scientific Instruments*, 80(11):114302, 2009.

[74] F Thiel, M Hein, U Schwarz, J Sachs, and F Seifert. Fusion of magnetic resonance imaging and ultra-wideband-radar for biomedical applications. In *Ultra-Wideband, 2008. ICUWB 2008. IEEE International Conference on*, volume 1, pages 97–100, 2008.

[75] I Graesslin. An Alternative Concept for Non-Sequence Interfering, Contact-free Respiration Monitoring. In *Proceedings 17th Annual Meeting, International Society for Magnetic Resonance in Medicine, Honolulu, Hawaii, USA*, 2009.

[76] D Buikman, T Helzel, and P Röschmann. The RF coil as a sensitive motion detector for magnetic resonance imaging. *Magnetic resonance imaging*, 6(3):281–289, 1988.

[77] A Andreychenko. Noise variance of an RF receive array reflects respiratory motion: a novel respiratory motion predictor. In *Proceedings 22th Annual Meeting, International Society for Magnetic Resonance in Medicine, Milan, Italy*, 2014.

[78] ZW Fu, Y Wang, RC Grimm, PJ Rossman, JP Felmlee, SJ Riederer, and RL Ehman. Orbital navigator echoes for motion measurements in magnetic resonance imaging. *Magnetic Resonance in Medicine*, 34(5):746–753, 1995.

[79] AJW Van der Kouwe, T Benner, and AM Dale. Real-time rigid body motion correction and shimming using cloverleaf navigators. *Magnetic resonance in medicine*, 56(5):1019–1032, 2006.

[80] N White, C Roddey, A Shankaranarayanan, E Han, D Rettmann, J Santos, J Kuperman, and A Dale. Promo: Real-time prospective motion correction in mri using image-based tracking. *Magnetic Resonance in Medicine*, 63(1):91–105, 2010.

[81] S Thesen, O Heid, E Mueller, and LR Schad. Prospective acquisition correction for head motion with image-based tracking for real-time fMRI. *Magnetic Resonance in Medicine*, 44(3):457–465, 2000.

[82] S Skare, A Hartwig, M Mårtensson, E Avventi, and M Engström. Properties of a 2d fat navigator for prospective image domain correction of nodding motion in brain MRI. *Magnetic Resonance in Medicine*, 73(3):1110–1119, 2015.

[83] T Kober, JP. Marques, R Gruetter, and G Krueger. Head motion detection using FID navigators. *Magnetic Resonance in Medicine*, 66(1):135–143, July 2011.

[84] ACS Brau and JH Brittain. Generalized self-navigated motion detection technique: Preliminary investigation in abdominal imaging. *Magnetic Resonance in Medicine*, 55(2):263–270, 2006.

[85] RR Ingle, JM. Santos, WR. Overall, MV. McConnell, BS. Hu, and DG. Nishimura. Self-gated fat-suppressed cardiac cine MRI: Self-Gated ATR-SSFP Cine MRI. *Magnetic Resonance in Medicine*, 73(5):1764–1774, May 2015.

[86] M Buehrer, J Curcic, P Boesiger, and S Kozerke. Prospective self-gating for simultaneous compensation of cardiac and respiratory motion. *Magnetic Resonance in Medicine*, 60(3):683–690, September 2008.

[87] P Hu, S Hong, MH. Moghari, B Goddu, L Goepfert, KV. Kissinger, TH. Hauser, WJ. Manning, and R Nezafat. Motion correction using coil arrays (MOCCA) for free-breathing cardiac cine MRI. *Magnetic Resonance in Medicine*, 66(2):467–475, August 2011.

[88] SC Amartu and HJ Vesselle. A new approach to study cardiac motion: the optical flow of cine MR images. *Magnetic Resonance in Medicine*, 29(1):59–67, 1993.

[89] TS Tenforde and TF Budinger. Biological effects and physical safety aspects of NMR imaging and in vivi spectroscopy. *NMR in Medicine*, 1985.

[90] G. M. Nijm, S. Swiryn, A. C. Larson, and A. V. Sahakian. *Characterization of the magnetohydrodynamic effect as a signal from the surface electrocardiogram during cardiac magnetic resonance imaging.* IEEE, 2006.

[91] JW Krug, G Rose, D Stucht, G Clifford, and J Oster. Limitations of VCG based gating methods in ultra high field cardiac MRI. *Journal of Cardiovascular Magnetic Resonance*, 15(Suppl 1):W19, 2013.

[92] JW Krug, G Rose, GD Clifford, and J Oster. ECG-based gating in ultra high field cardiovascular magnetic resonance using an independent component analysis approach. *J Cardiovasc Magn Reson*, 15:104, 2013.

[93] SE Fischer, SA Wickline, and CH Lorenz. Novel real-time R-wave detection algorithm based on the vectorcardiogram for accurate gated magnetic resonance acquisitions. *Magnetic Resonance in Medicine*, 42(2):361–370, 1999.

[94] JM Chia, SE Fischer, SA Wickline, and CH Lorenz. Performance of QRS detection for cardiac magnetic resonance imaging with a novel vectorcardiographic triggering method. *Journal of Magnetic Resonance Imaging*, 12(5):678–688, 2000.

[95] C Li, C Zheng, and C Tai. Detection of ECG characteristic points using wavelet transforms. *Biomedical Engineering, IEEE Transactions on*, 42(1):21–28, 1995.

[96] J Felblinger, J Slotboom, R Kreis, B Jung, C Boesch, et al. Restoration of electrophysiological signals distorted by inductive effects of magnetic field gradients during MR sequences. *Magnetic Resonance in Medicine*, 41(4):715–721, 1999.

[97] AM Weissler, WS Harris, and CD Schoenfeld. Systolic time intervals in heart failure in man. *Circulation*, 37(2):149–159, 1968.

[98] F Contijoch, WRT Witschey, K Rogers, J Gorman, RC Gorman, V Ferrari, and Y Han. Impact of end-diastolic and end-systolic phase selection in the volumetric evaluation of cardiac MRI: Selection of Cardiac Phases. *Journal of Magnetic Resonance Imaging*, September 2015.

[99] J Mispelter, M Lupu, and A Briguet. *NMR probeheads for biophysical and biomedical experiments: theoretical principles & practical guidelines*. Imperial College Press, 2006.

[100] DI Hoult and PC Lauterbur. The sensitivity of the zeugmatographic experiment involving human samples. *Journal of Magnetic Resonance (1969)*, 34(2):425–433, 1979.

[101] TW Redpath and JMS Hutchison. Estimating patient dielectric losses in nmr imagers. *Magnetic resonance imaging*, 2(4):295–300, 1984.

[102] A Haase, F Odoj, M Von Kienlin, J Warnking, F Fidler, A Weisser, M Nittka, E Rommel, T Lanz, B Kalusche, et al. NMR probeheads for in vivo applications. *Concepts in Magnetic resonance*, 12(6):361–388, 2000.

[103] TKF Foo, CE. Hayes, and Y-W Kang. An analytical model for the design of RF resonators for MR body imaging. *Magnetic resonance in medicine*, 21(2):165–177, 1991.

[104] JG van Heteren, RM Henkelman, and MJ Bronskill. Application of an equivalent circuit to signal-to-noise calculations in MRI. *Magnetic resonance imaging*, 5(2):101–108, 1987.

[105] PA Hasgall, F Di Gennaro, C Baumgartner, E Neufeld, MC Gosselin, D Payne, A Klingenboeck, and N Kuster. ITIS-Database for thermal and electromagnetic parameters of biological tissues, 2015.

[106] P Nopp, E Rapp, H Pfutzner, H Nakesch, and C Rusham. Dielectric properties of lung tissue as a function of air content. *Physics in Medicine and Biology*, 38(6):699–716, June 1993.

[107] SJ Vannesjoe. Snapshot field monitoring enables correction of slow field perturbations in high-res brain MRI. In *Proceedings of the 21st Scientific Meeting, International Society for Magnetic Resonance in Medicine*, page 2569, 2013.

[108] CE Hayes, WA Edelstein, JF Schenck, OM Mueller, and M Eash. An efficient, highly homogeneous radiofrequency coil for whole-body NMR imaging at 1.5 T. *Journal of Magnetic Resonance (1969)*, 63(3):622–628, 1985.

[109] JJ Ackerman, TH Grove, GG Wong, DG Gadian, and GK Radda. Mapping of metabolites in whole animals by 31P NMR using surface coils. *Nature*, 283(5743):167–170, 1980.

[110] PB Roemer, WA Edelstein, CE Hayes, SP Souza, and OM Mueller. The NMR phased array. *Magnetic resonance in medicine*, 16(2):192–225, 1990.

[111] J Wang. A novel method to reduce the signal coupling of surface coils for MRI. In *Proceedings of the 4th Annual Meeting of ISMRM, New York, NY, USA*, page 1434, 1996.

[112] Agilent Impedance Measurement Handbook - A guide to measurement technology and techniques, 2013.

[113] KW Belt and DJ Schaefer. *Apparatus and method of acquiring physiological gating signals for magnetic resonance imaging of moving objects*. Google Patents, December 1987. US Patent 4,712,560.

[114] D Formica and S Silvestri. Biological effects of exposure to magnetic resonance imaging: an overview. *Biomedical engineering online*, 3(1):11, 2004.

[115] C Gabriel, S Gabriel, and E Corthout. The dielectric properties of biological tissues: I. Literature survey. *Physics in medicine and biology*, 41(11):2231, 1996.

[116] RP Patterson. Fundamentals of impedance cardiography. *Engineering in Medicine and Biology Magazine, IEEE*, 8(1):35–38, 1989.

[117] M Cheney, D Isaacson, and JC Newell. Electrical impedance tomography. *SIAM review*, 41(1):85–101, 1999.

[118] R Vas. Electronic device for physiological kinetic measurements and detection of extraneous bodies. *Biomedical Engineering, IEEE Transactions on*, (1):2–6, 1967.

[119] T. S. Ibrahim, R. Lee, B. A. Baertlein, and PM L. Robitaille. B1 field homogeneity and SAR calculations for the birdcage coil. *Physics in medicine and biology*, 46(2):609, 2001.

[120] E Neufeld, S Kühn, G Szekely, and N Kuster. Measurement, simulation and uncertainty assessment of implant heating during mri. *Physics in medicine and biology*, 54(13):4151, 2009.

[121] A Kuehne, S Goluch, P Waxmann, F Seifert, B Ittermann, E Moser, and E Laistler. Power balance and loss mechanism analysis in RF transmit coil arrays: Transmit Array Loss Analysis. *Magnetic Resonance in Medicine*, pages n/a–n/a, October 2014.

[122] Jian-Ming Jin. Practical electromagnetic modeling methods. *eMagRes*.

[123] F Odille, C Pasquier, R Abacherli, P-A Vuissoz, GP. Zientara, and J Felblinger. Noise Cancellation Signal Processing Method and Computer System for Improved Real-Time Electrocardiogram Artifact Correction During MRI Data Acquisition. *IEEE Transactions on Biomedical Engineering*, 54(4):630–640, April 2007.

[124] P-A Vuissoz, F Odille, B Fernandez, M Lohezic, A Benhadid, D Mandry, and J Felblinger. Free-breathing imaging of the heart using 2D cine-GRICS (generalized reconstruction by inversion of coupled systems) with assessment of ventricular volumes and function. *Journal of Magnetic Resonance Imaging*, 35(2):340–351, 2012.

[125] D Atkinson, DLG Hill, PNR Stoyle, PE Summers, S Clare, R Bowtell, and SF Keevil. Automatic compensation of motion artifacts in MRI. *Magnetic Resonance in Medicine*, 41(1):163–170, 1999.

[126] MD. Harpen. Sample noise with circular surface coils. *Medical Physics*, 14(4):616, 1987.

[127] MG Taylor. Wave travel in arteries and the design of the cardiovascular system. *Pulsatile blood flow*, pages 343–372, 1964.

[128] S. C. Millasseau, A. D. Stewart, S. J. Patel, S. R. Redwood, and P. J. Chowienczyk. Evaluation of Carotid-Femoral Pulse Wave Velocity: Influence of Timing Algorithm and Heart Rate. *Hypertension*, 45(2):222–226, February 2005.

[129] J Choo, C Shin, E Barinas-Mitchell, K Masaki, BJ Willcox, TB Seto, H Ueshima, S Lee, K Miura, L Venkitachalam, et al. Regional pulse wave velocities and their cardiovascular risk factors among healthy middle-aged men: a cross-sectional population-based study. *BMC cardiovascular disorders*, 14(1):5, 2014.

[130] NHL Kuijpers, W Dassen, PM van Dam, EM van Dam, E Hermeling, J Lumens, T Arts, and T Delhaas. Circadapt: A user-friendly learning environment for (patho) physiology of heart and circulation. In *Computing in Cardiology (CinC), 2012*, pages 969–972. IEEE, 2012.

[131] SK Bulumulla, E Fiveland, K Park, and J Iannotti. MEMS reconfigurable coils. In *Proceedings of the 23rd Annual Meeting of ISMRM, Toronto, Canada*, page 1797, 2015.

[132] S-M Sohn, A Gopinath, and JT Vaughan. On-coil power monitor with a high directivity coupler. In *Proceedings of the 23rd Annual Meeting of ISMRM, Toronto, Canada*, page 1817, 2015.

Résumé

En imagerie par Résonance Magnétique cardiaque et thoracique, les mouvements cardiaques et respiratoires sont enregistrés avec des capteurs tels que les capteurs ECG et les ceintures respiratoires pour synchroniser les acquisitions et pour pratiquer des corrections rétrospectives des images. Le positionnement de ces capteurs augmente le temps de préparation des patients. Il présuppose également leur tolérance par les patients placés dans un espace restreint et déjÃ trÃ¨s contraints par l'antenne radio-fréquence (RF) nécessaire Ã¡ l'imagerie. Enfin, ces capteurs peuvent diminuer la qualité du signal et donc celle des images. Dans ces travaux, l'antenne RF déjÃ présente pour la réalisation de l'exam d'imagerie a été elle-mÃªme étudiée en tant que capteur de mouvements. Les variations des propriétés électromagnétiques des tissus dues aux mouvements se répercutent de maniÃ¨re directe sur l'impédance de l'antenne. Les variations d'impédance induites par les mouvements ont été étudiées dans des dispositif utilisant soit des antennes RF volumique ou des antennes RF surfacique sur des objets-test animés et sur des sujets sains. Les mouvements respiratoires, cardiaques et les flux sanguins ont été enregistrés avec cette méthode. Puis, les résultats expérimentaux ont été comparés Ã des simulations électromagnétiques et aux données de la littérature. Une correction de mouvements rétrospective avec l'algorithme GRICS a été appliquée Ã ces données démontrant la faisabilité de l'utilisation des antennes d'imagerie comme capteurs de mouvements.

Mots clés

Imagerie par Résonance Magnétique, antenne Radio-Fréquence (RF), mesures d'impédance, enregistrement de mouvements, imagerie cardiaque

Abstract

Especially in cardiac and thoracic magnetic resonance imaging, respiratory motion and heart movement need to be registered using sensors like electrocardiogram or respiratory belts, in order to trigger the image acquisition or perform retrospective corrections. The placement of the sensors extends the patient preparation time, is critical for signal quality and, hence, image quality, and expects patients to tolerate additional sensors besides the imaging coil and space restrictions. In this work, the imaging coil itself was investigated for sensor-less motion registration. Motion-related variations of the electromagnetic properties of tissue have a direct effect on the coil impedance. Lung motion, myocardial-related motion, and vascular blood flow were registered with this method. The experimental findings were compared to electromagnetic simulations and the data gathered by state-of-the-art sensors, and retrospective motion correction with the GRICS algorithm was executed.

Keywords

Magnetic Resonance Imaging, RF coil, impedance measurement, motion registration, Cardiac imaging